OBSERVATION OF PROMPT SINGLE MUON PRODUCTION BY 400 GEV PROTONS

Thesis by

Kay Wyatt Brown Merritt

In Partial Fulfillment of the Requirements
for the Degree of
Doctor of Philosophy

California Institute of Technology
Pasadena, California

1981

(submitted July 7, 1980)

ACKNOWLEDGMENTS

I am deeply indebted to all the other members of the E379 experiment - Barry Barish, Fritz Bartlett, Arie Bodek, Mike Shaevitz, Eric Siskind, Alain Diamant-Berger, Pat Dishaw, Martin Faessler, John Liu, Frank Merritt, and Stan Wojcicki - for their contributions to all phases of the experiment. I also want to thank my advisor, Frank Sciulli, for his contributions to the early stages of the experiment and for his advice and support during the analysis.

Particular acknowledgment is due to Frank Merritt, Stan Wojcicki, Alain Diamant-Berger, Mike Shaevitz, Eric Siskind, and Pat Dishaw for their large share in writing the analysis programs and working on the alignment and calibration programs.

Technical assistance with the building of the experiment was provided by the shops of SLAC Group G and Caltech. The Neutrino Lab at Fermilab and other Fermilab groups provided operational and technical support.

I thank Louise Sartain of Caltech for an excellent typing job. The Graphic Arts facility at Caltech generated the illustrations promptly and competently.

Financial support during my graduate study was provided by the National Science Foundation and by Caltech.

My special thanks go to Frank Merritt for his patience, encouragement, and critical evaluations of this work.

ABSTRACT

The observation of prompt single muon production from 400 GeV protons interacting in an iron target is reported. The experiment used a variable-density calorimeter made of iron plates and plastic scintillator as a target, followed by a large-acceptance muon identifier and an iron toroidal spectrometer. Single muon and dimuon events were separated with good efficiency using the muon identifier, and the rate of prompt single muons was measured by varying the density of the target-calorimeter, thereby changing the relative rate of prompt and non-prompt single muon production.

Prompt single muon signals were observed in two different kinematic regions - $p_\mu < 20$ GeV/c, $p_{t\mu} > 1$ GeV/c and 10 GeV/c $< p_\mu <$ 60 GeV/c, $p_{t\mu} > 0.5$ GeV/c. Approximate equality was found between the prompt $1\mu^+$ and prompt $1\mu^-$ signal in the high p region (in the high p_t region, only positive muons were accepted by the trigger). The observed cross section in both regions was ~ 70 nb/nucleon, assuming linear A dependence for the production of the prompt muons.

Hadronic production of charmed particles was the most likely source of the prompt muons; other possible sources could not account for the large rates observed. Three different models for charm production - uncorrelated D production, correlated $D\overline{D}$ production, and diffractive production of Λ_c-D pairs - are compared to the data and used to calculate cross sections. Within the $D\overline{D}$ model, the range of kinematic parameters allowed by the data is determined and the corresponding range of cross sections is 20-70 μb/nucleon. The results of this experiment are compared with other experimental results and with theoretical predictions of charm production.

TABLE OF CONTENTS

Chapter 1: Introduction

Chapter 2: Beam and Apparatus

Chapter 3: Triggering

Chapter 4: Event Analysis

Chapter 5: High p Data Analysis

Chapter 6: High p_t Data Analysis

Chapter 7: Interpretation of the Prompt Single Muon Signal

CHAPTER 1

INTRODUCTION

1.1 Sources of Prompt Leptons

For more than a decade, high energy physicists have found it informative to study the reaction

$$p + N \rightarrow \begin{matrix} \mu^{\pm} \\ e^{\pm} \end{matrix} + \text{anything}$$

where the lepton is produced promptly, on a time scale short compared with the charged pion lifetime of 10^{-8} seconds. Since about 1974, the terms prompt lepton or direct lepton have been used to refer broadly to leptons from the decays of any source other than pions, kaons, or hyperons. This admittedly loose definition includes the electromagnetic decays of vector mesons, the direct production of charged lepton pairs via the Drell-Yan mechanism[1], and the weak decays of any heavy particles not falling into the familiar low-lying SU(3) multiplets (e.g., charmed particles). Illustrations of these categories are shown in Figure 1-1. The study of the first two categories has certainly been fruitful. One of the ways the psi particle was discovered was the observation of a peak in the mass spectrum of prompt dimuons[2], and the upsilon particle was also discovered with that technique[3]. Studies of the non-resonant dimuon continuum have yielded better understanding of the Drell-Yan mechanism[4], and are beginning to shed light on related QCD mechanisms for dimuon production[5]. This thesis discusses an experiment which searched for the third category of prompt leptons: those produced in the weak decay of heavy particles. In

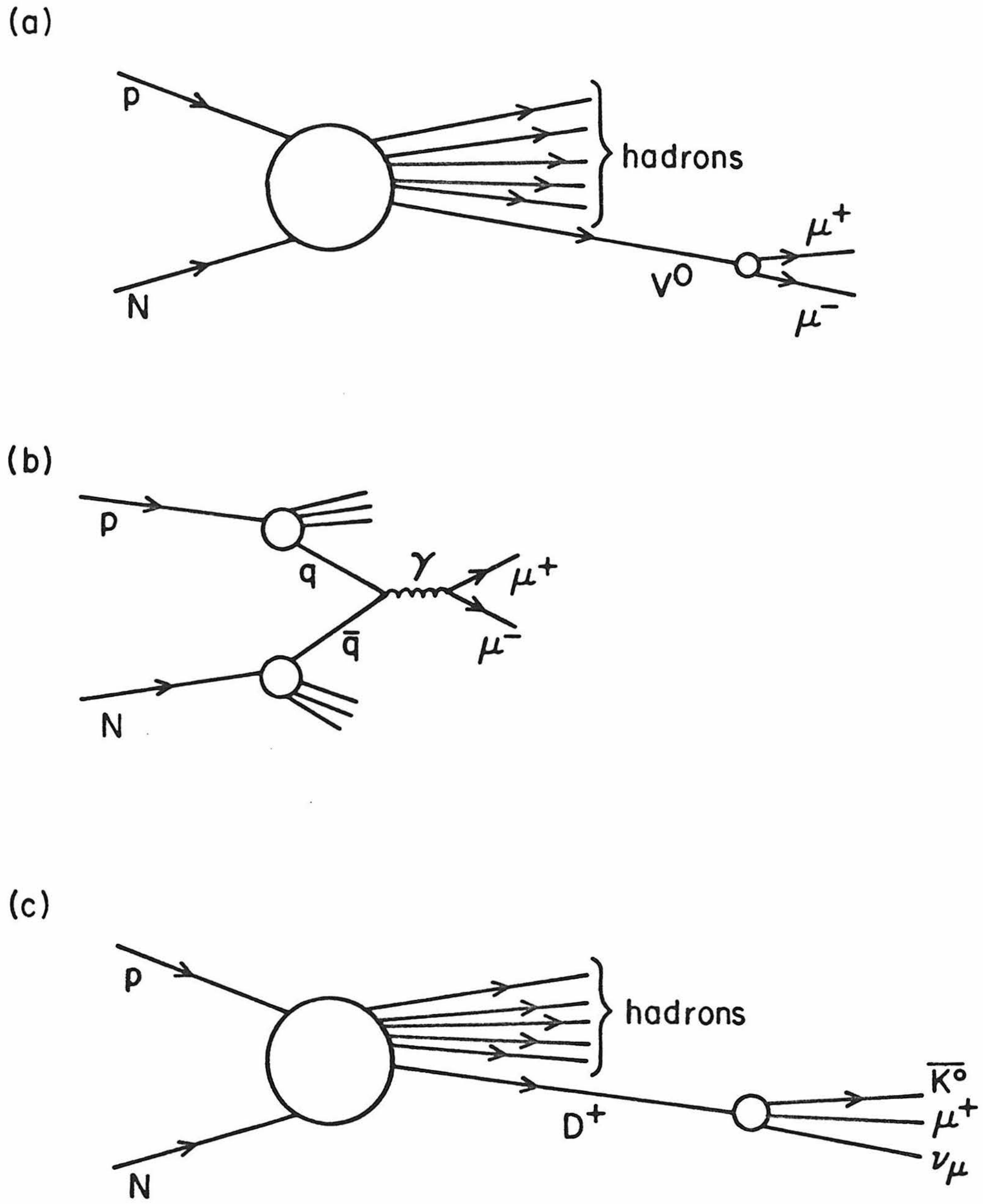

Figure 1-1: Three classes of prompt muon production -
(a) A vector meson decays into $\mu^+\mu^-$.
(b) A quark and an antiquark annihilate into a virtual photon, which then decays into $\mu^+\mu^-$.
(c) A charmed particle (e.g., D^+) decays weakly into a muon, a neutrino, and hadrons.

particular, the experiment looked for prompt single muon production as a signature of charmed particle production by hadrons, in the reaction

$$\begin{array}{l} p + \mathrm{Fe} \to C + \text{anything} \\ \qquad\qquad\quad \lfloor\!\!\longrightarrow \mu\nu_\mu + \text{anything} \end{array}$$

where C is a charmed particle.

The general process depicted in Figure 1-1a is the production of a neutral vector meson V^o and the subsequent electromagnetic decay of the meson into a pair of oppositely charged muons. The meson V^o, for the incident energies used in this experiment, may be ρ, ω, ϕ or ψ. (Upsilon production has too small a cross section to be observed in this experiment.) This source of dimuon production, like the direct dimuon production discussed next, is only relevant to the charm search as a background, when one of the muons is not observed.

Figure 1-1b shows schematically the direct production of a muon pair. In the conventional picture of hadron physics, the incident proton and the target nucleon contain quark-antiquark pairs as well as the so-called valence quarks, and in the interaction a quark and an antiquark can annihilate, producing a virtual photon which decays into a $\mu^+\mu^-$ pair with a continuum of invariant mass values. This is the original Drell-Yan mechanism[4]. There may also be corrections to $q\bar{q} \to \mu^+\mu^-$ from the processes of quantum chromodynamics, the candidate gauge theory of strong interactions[6].

The third diagram, Figure 1-1c, is the signal for which this experiment searched - the production of a heavy particle and its subsequent weak decay. In principle, the heavy particle could be any particle prevented from immediate strong decay into other hadrons; for example, the lowest lying state of a particle family carrying a new conserved quantum number. In practice, C must have an appreciable semi-leptonic branching ratio and a possible production cross section of the order of 10 microbarns to be seen in this experiment. Charmed particles were expected to fit both specifications[7,8].

Note that the only reason for tying these three disparate processes together is the "promptness" of the lepton production - these processes occur on a time scale of 10^{-12} sec or less compared with 10^{-8} sec for the production of leptons from charged pion decay. In this experiment, the technique of density extrapolation, described later, was used to separate prompt and non-prompt leptons on a statistical basis, and then the prompt events from the third possible source, weak decay of a heavy particle, were identified as those with only a single muon observed.

1.2 Theory of Charmed Particle Production

All the hadrons observed up until 1974 could be described as containing various combinations of the three quarks u, d, and s and their antiquarks $\bar{u}$, $\bar{d}$, and $\bar{s}$. There was, however, growing indirect evidence of the need for a fourth quark c to explain the suppression of strangeness changing neutral currents and other difficulties. This quark, as postulated by Glashow and others[9], would carry a new conserved quantum number named charm.

In 1974, the charm idea was experimentally verified[2,10] with the discovery of the ψ, a meson composed of $c\bar{c}$. The e^+e^- storage ring experiments[10] proceeded to identify the mesons with only one charmed quark, i.e., with bare charm - D, D* and F - and the predictions of the spectroscopy seemed in agreement with experiment. Theoretically expected values for the lifetimes of charmed particles were on the order of 10^{-13} sec[7], so that direct observation of charmed particle production required the use of techniques for detecting very short tracks, such as emulsion techniques. Most searches for hadronic production of charm were based on detecting the decay products. But the production of bare charm in hadronic collisions was not observed, and the theoretical predictions of cross sections for such production were very difficult to make.

One way to produce charmed quarks from ordinary hadron collisions is a mechanism analogous to the Drell-Yan process discussed above: $q\bar{q} \to c\bar{c}$ via a virtual photon, where q = u, d, or s. This mechanism yields a very small cross section. Other diagrams (Figure 1-2) can be drawn in the framework of quantum chromodynamics (QCD). Like all QCD problems, the calculation of these diagrams is quite difficult. Some attempts are listed in Reference 8. The estimates for the total cross section for bare charm production range from 1 to 30 microbarns, for proton on proton at $\sqrt{s} = 28$ GeV. Clearly, an experimental determination of the cross section would be very desirable even though the most prominent theory can provide no clear prediction of dominant mechanisms. This thesis aims to constrain as much as possible the value of the total cross section.

1.3 Experimental Technique

This experiment was proposed in 1975 and carried out in 1977 at the Fermi National Accelerator Laboratory (Fermilab). The basic setup

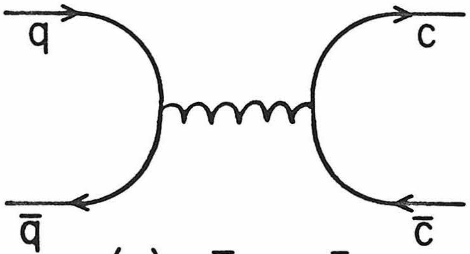

(a) $q\bar{q} \rightarrow c\bar{c}$

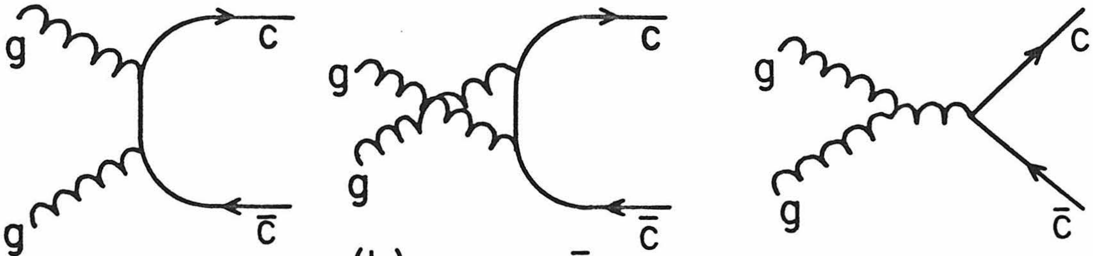

(b) $gg \rightarrow c\bar{c}$

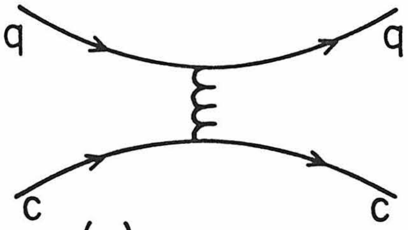

(c) $qc \rightarrow qc$

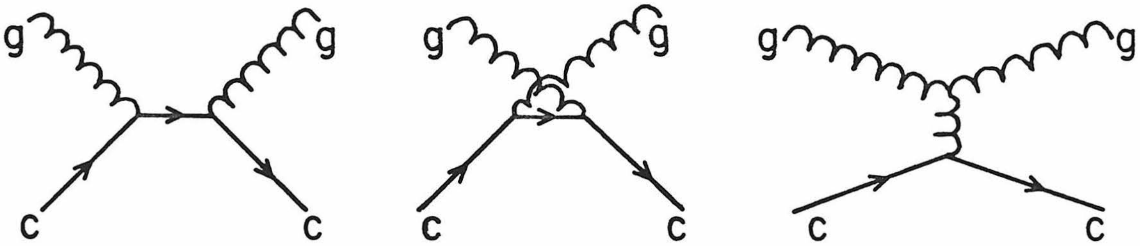

(d) $gc \rightarrow gc$

Figure 1-2: The lowest order diagrams in QCD for the creation of a pair of charmed quarks: (a) quark fusion, (b) gluon fusion, (c) quark excitation of a charmed quark from the ocean, (d) gluon excitation of a charmed quark from the ocean.

consisted of a proton beam striking an iron target-calorimeter with a muon identifier and an iron spectrometer following. Trigger counters placed around and within the spectrometer were used to signal the passage of a muon.

Single muon events were identified by the presence of only one track in the spark chambers downstream of the muon identifier. The key to the separation of these events into prompt and non-prompt categories was the variable density of the target calorimeter.

The decay length for a charged pion is $\gamma \cdot 780$ cm; for a D meson it is approximately $\gamma \cdot 10^{-2}$ cm. The typical meson interaction length in steel is 20 cm. Therefore, charged pions produced in a dense material are overwhelmingly more likely to interact than to decay, but D mesons exhibit the opposite behavior. If the density of the target material is varied, thereby changing the effective interaction length λ_i, the rate of pion or other non-prompt decay varies directly as the interaction length (inversely as the density) provided that λ_i remains small compared with $c\tau$ (see Appendix for a calculation of the deviations from linear variation). For D mesons, however, the decay rate would not be affected at all unless the interaction length became comparable to 10^{-2} cm, corresponding to densities certainly not achievable in the laboratory. Over the range of density variation in this experiment (pion interaction lengths between 25 and 50 cm), the non-prompt decay rate will vary linearly with inverse density and the charm decay rate will be constant as a function of density. If the sum of the charm and non-prompt rates is plotted versus inverse density, the sum will fit a linear function whose intercept at infinite density measures the charm rate and whose slope measures the non-prompt rate.

The variation of effective interaction length in this experiment was achieved by dividing the calorimeter into steel plates which were movable on rails along the beam direction. By introducing air gaps between the plates, the effective interaction length could be increased by a factor of 2.

1.4 Outline of Thesis

Chapter 2 of the thesis describes more fully the incident beam and the apparatus used. Chapter 3 gives details of the two triggering schemes. In Chapter 4, the process of converting the raw data to physical quantities specifying the event is discussed. Chapters 5 and 6 detail the parallel analysis of the two data sets, resulting in a single prompt muon rate as a function of p and p_t for the kinematic region covered by the two triggers. Finally, Chapter 7 explores the possible sources for the signal and the agreement of the data with those from other experiments. Unless otherwise noted the symbols p and p_t are used in this thesis to represent the momentum and the momentum transverse to the beam, respectively, of the muons observed in the apparatus.

CHAPTER 2

BEAM AND APPARATUS

2.1 The Accelerator Environment

The experiment used the N5 secondary beam line of the Fermilab accelerator. The data were collected between March and June, 1977. During this period, the proton synchrotron (the Main Ring) was operated at an energy of 400 GeV. A pulse, or spill, of protons was extracted from the Main Ring at intervals of 10 seconds, and the length of the spill was 1 or 2 seconds at different running periods. The extracted proton beam was split into several beams, one of which was transported to a copper target at the beginning of the N5 beam line. The N5 beam line is described below. The radio frequency (rf) cavities of the accelerator operate at a period of 18.86 nanoseconds. This time interval is frequently called an rf bucket, and timing signals which clock these intervals were used in the experiment for several purposes.

2.2 General Description of the Apparatus

The detector (Figure 2-1) was located in Lab E in the Neutrino Area at Fermilab, and was centered on the N5 hadron beam line. The beam emerged from a dipole spectrometer upstream of Lab E to interact in a steel-scintillator calorimeter. Particles exiting the calorimeter passed through another steel-scintillator sandwich for absorption of any remaining hadrons and identification of muons. The momenta of the muons were measured using an iron toroidal spectrometer.

2.3 The N5 Beam Line

The N5 beam line was originally designed to deliver hadrons to the

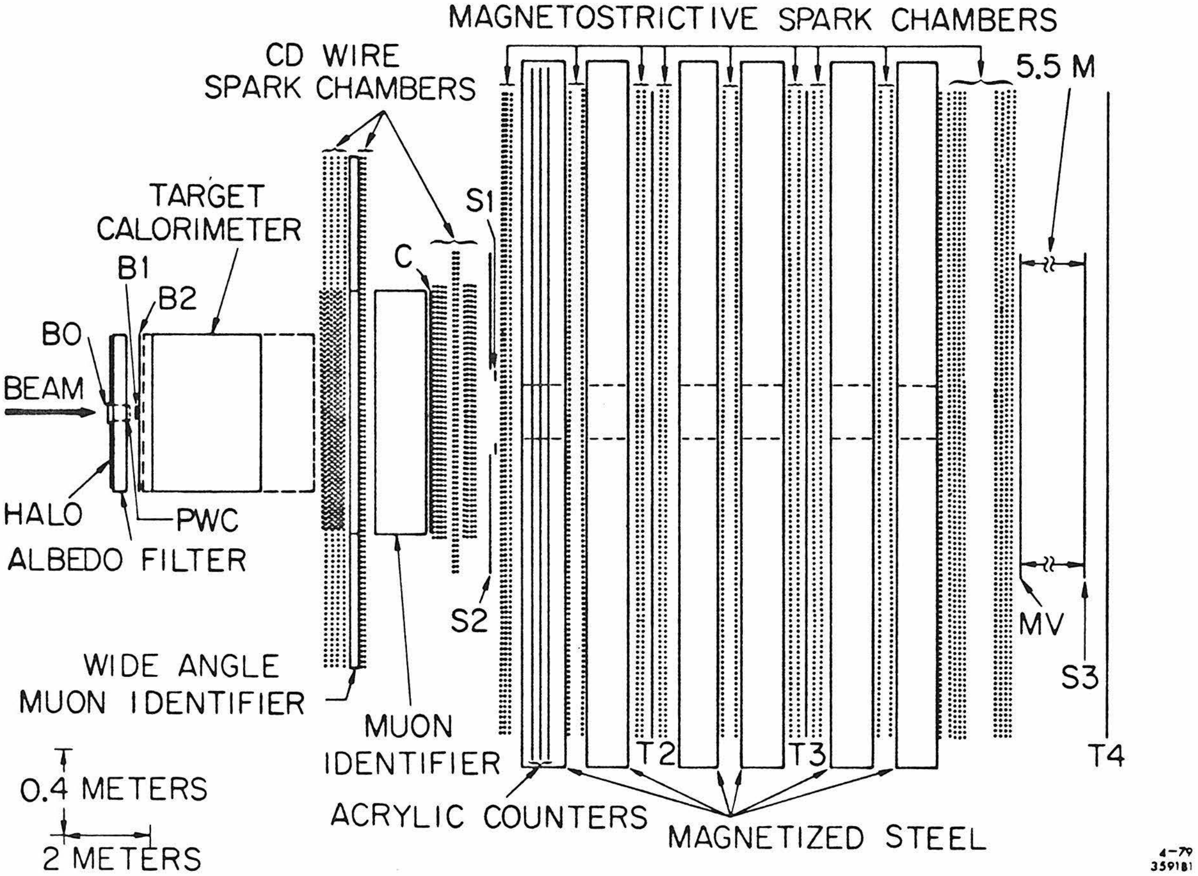

Figure 2-1: The apparatus in the configuration used for high p_t data taking. The dashed lines around the calorimeter indicate the space occupied when the plates are expanded to 1/2 the effective density; the solid lines indicate the plates in the most compact position. The dashed lines in the magnetized steel outline the central hole.

Fermilab bubble chambers. Our group was the first to use the beam line for a counter experiment requiring high intensities.

The beam was produced by targeting the primary beam on a copper target. The production angle and secondary momentum and sign were selectable. The beam line was 1 km long, with two major bends; its optics are discussed in Reference 11.

During all the data-taking discussed in this thesis, the beam line was tuned to deliver positive particles of momentum 400 GeV, with a primary beam of 400 GeV. It accepted mainly diffracted protons with a momentum spread of 1.0%. At the front of the calorimeter, the beam diameter was 6 cm. Typical beam intensities at the apparatus were 5×10^5 protons per second (pps) during the high p_t run and 5×10^4 pps during the high p run.

2.4 Defining the Beam

Immediately upstream of our experimental building were placed two dipoles which bent the beam through 16.5 mrad into our apparatus. There were 8 planes of proportional wire chambers (PWCs) located upstream and downstream of the dipoles (see Figure 2-2). They were placed in pairs, with one plane measuring the x coordinate and one the y coordinate. Each plane contained 48 wires spaced 1 mm apart. This system enabled rejection of events with more than one incident track.

Definition of the beam particle and further rejection of events with halo accompanying the beam were provided by counters situated just upstream of the calorimeter (Figure 2-1). The beam passed through B0 (7.6 x 7.6 cm), B1 (5 x 5 cm), and B2 (75 x 75 cm). The halo counter

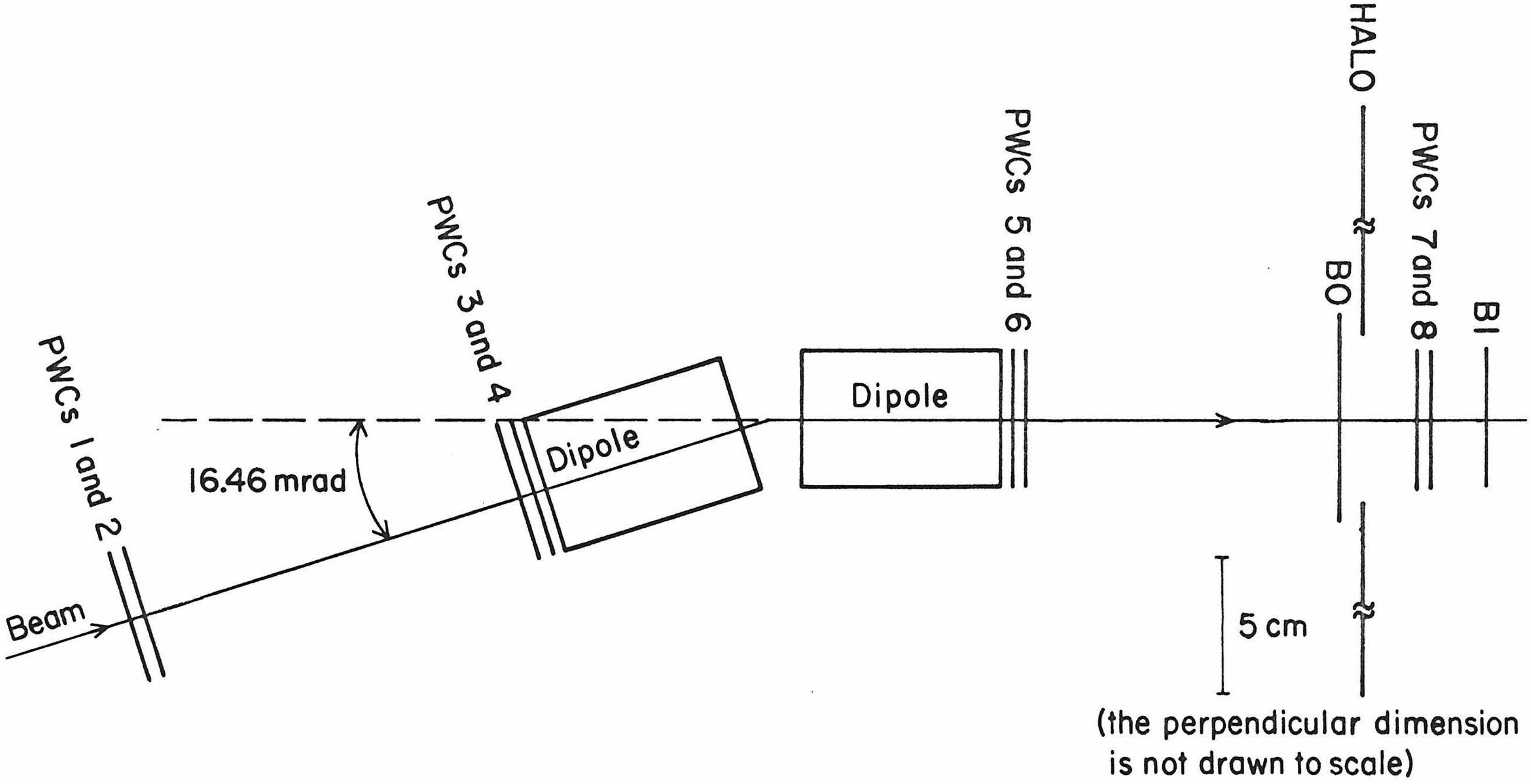

Figure 2-2: The spectrometer upstream of the apparatus, used for measuring the momentum of the incoming beam. The distance from the bend point in the center of the dipoles to PWCs 1 and 2 and to PWCs 7 and 8 was approximately 20 meters.

H covered the area out to 38 cm, excluding a 6.3 cm square in the center. All these counters were viewed by 56AVP phototubes, and their signals were pulse-height analyzed. The signal from counter H entered all triggers as a veto, and H was protected from backscattering (albedo) from the calorimeter interaction by a 30 cm thickness of steel called the albedo filter.

2.5 The Calorimeter and the Muon Identifier

The calorimeter (Figure 2-1) was a central element in the design of this experiment. It had three functions: to serve as a target for the proton interaction, to measure the total hadronic energy produced in the interaction, and to measure (by the variation of its effective interaction length) the number of single muon events from weak decays of long-lived particles (π's, K's and hyperons).

The calorimeter consisted of 45 plates of steel, each backed by a 0.6 cm thick plastic scintillator to sample the ionization energy of the shower (see Figure 2-3a). The plates and scintillators were all 75 x 75 cm in transverse dimension. Plates 1-20 were 3.8 cm thick; plates 21-45 were 5.0 cm thick; the total length of steel was therefore 202.3 cm. Spacing was made finer at the front because most of the shower energy was deposited there, and hence better resolution was more helpful there. It was a sampling calorimeter[12]; energy was measured by sampling the ionization energy periodically through the shower.

The 45 scintillators were viewed by 6342A phototubes. Amplified (by a factor of 40) and unamplified signals from the phototubes were pulse-height analyzed. For monitoring purposes, on each scintillator

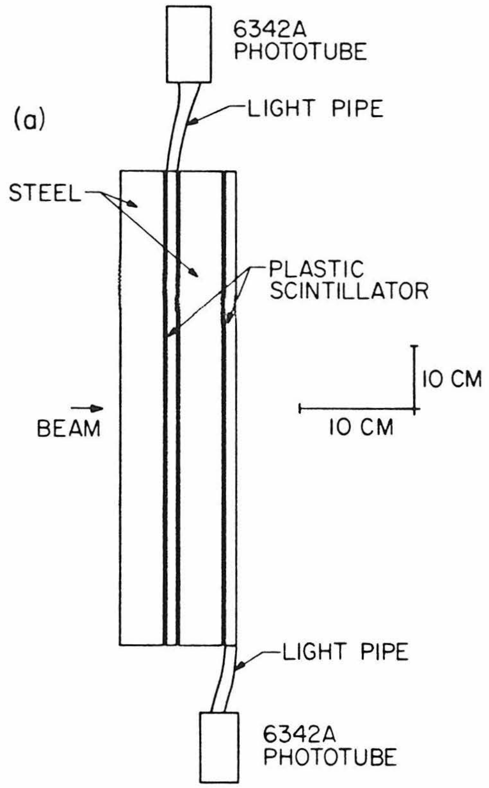

Figure 2-3: (a) Two calorimeter modules.

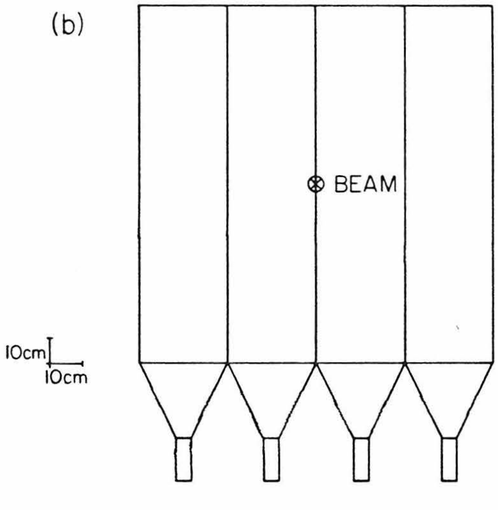

Figure 2-3: (b) A plane of the muon identifier counters. There are ten such planes, each behind a 10 cm steel plate. The phototubes are alternately on the upper and lower sides of each plane.

was placed an LED and on each of the first 31 scintillators was placed a glass fiber which transmitted light from a Xenon spark gap pulser. Other fibers transmitted the pulser light to phototubes not attached to counters and not counting beam particles. These reference tubes also counted the signal from an ^{241}Am α source embedded in a NaI(Tl) crystal. The use of these signals to monitor and correct for changes in the calibration is discussed in Chapter 4.

Long-lived particle decays were separated from short-lived particle decays by varying the effective interaction length, or density, for the hadrons in the 400 GeV shower. This variation was accomplished by moving the plates along a set of rails parallel to the beam direction. Data were taken at three interaction lengths: with plates 1-26 completely compacted, with a gap equal to half the module width between each of plates 1-26, and with a gap equal to the module width. In each configuration, plates 26-41 were moved as a unit, so that plate 27 backed up plate 26 with no gap. Plates 42-45 were not movable. Figure 2-4 shows the positions of the plates in the three configurations.

One meter downstream of the fine-grained target calorimeter was another coarser grained calorimeter sandwich, the muon identifier. This steel scintillator module measured any hadron energy leaking out the end of the target calorimeter and absorbed out these low energy hadrons, leaving only muons to emerge. The module contained 10 steel plates, each 10 cm thick and 112 x 144 cm wide. Behind each plate were 4 plastic scintillators, 1.3 cm thick, 28 cm horizontally by 144 cm vertically (Figure 2-3b). The counters were viewed by 56AVP phototubes

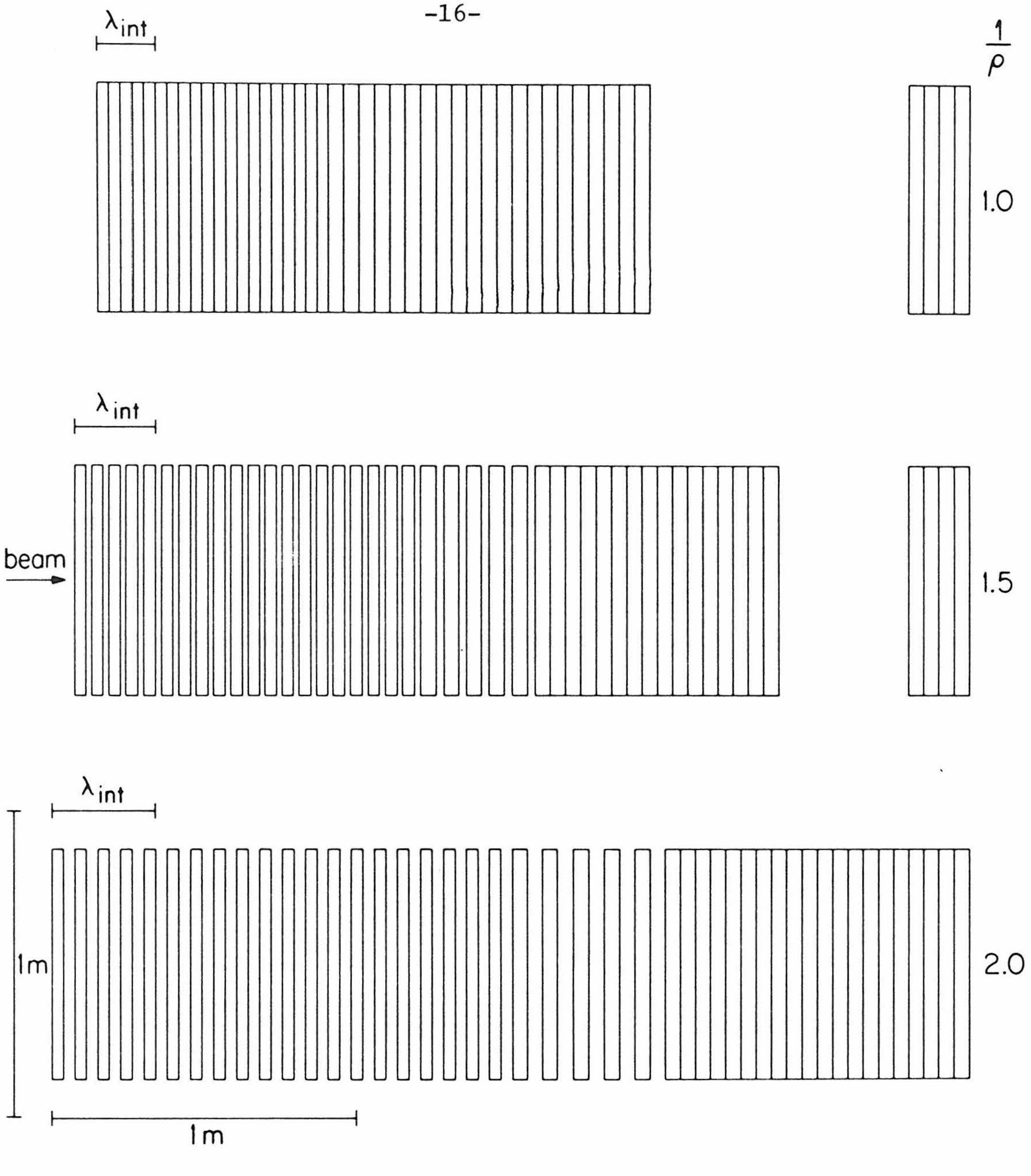

Figure 2-4: The positions of the calorimetry plates are shown for the three density configurations used in the experiment: compacted ($1/\rho = 1.0$), semi-expanded ($1/\rho = 1.5$), and expanded ($1/\rho = 2.0$).

and the signals were pulse-height analyzed. A 20 cm thick steel frame surrounded this module out to 122 cm from the beam line, and was used to identify muons out at wide angles.

The first order gain adjustment for the phototubes of both the calorimeter and the muon identifier was obtained by measuring the minimum ionizing signals in each counter using an incident muon beam. This adjustment was refined for the calorimeter by looking at the profiles of 400 GeV showers and requiring the average profile to be invariant as the interaction point moved along the calorimeter. The resolution at 400 GeV was 3.4% using the shower profile technique at low incident intensity. For the intensities used to collect the data sample, rate-induced effects worsened this resolution to 3.8%, which could be corrected to 3.5% using hardware monitors of the instantaneous rate and the phototube gains. Overall calibration shifts were taken out by normalization to a sample of 400 GeV showers collected continuously along with the muon events.

2.6 The Muon Spectrometer

Tracking the muons began immediately downstream of the target calorimeter, with 8 x-y and 2 u-v planes of wire spark chambers bracketing the muon identifier (Figure 2-1). Signals for each wire of the chambers were read out using a capacitor-diode circuit[13] and encoded as computer words. The momentum and sign of muons were determined by tracing the tracks from these chambers through three iron toroids, each 3 m in diameter. Total $\int B \cdot dl$ of the toroids was 80 kG-m, giving a p_t kick of 2.4 GeV to each muon. The polarity was set to focus positive particles.

Each toroid contained eight 20.3 cm thick disks, so there were 4.9 m of steel in the system. The disks had a 25 cm hole in the center. Copper coils of 60000 amp-turns wound around the disks through the center hole, producing an azimuthal field of ~ 18 kG. After each disk was a 5 cm gap for a scintillation counter; during the E379 run, only the first 3 gaps contained counters. After each 4 disks, a larger gap contained planes of magnetostrictive wire spark chambers, which were read out into multi-time digitizers[14]. The momentum resolution of the system, as measured with an incident muon beam, was 11%. The absolute calibration of the momentum was good to about 3%.

2.7 Trigger Counters

The beam-defining counters have already been described in Section 2.2. Different triggers used various counters downstream of the calorimeter to signal the presence of a muon. Here the physical dimensions and placement of these counters are described (see Figure 2-1).

Mounted on the back of the muon identifier were the C counters, four 77 x 77 cm counters forming a 144 cm square. A hodoscope immediately upstream of the toroids consisted of: S1, a 42.5 cm square with a 30 cm diameter hole, divided in half; and S2, an array of eight 152 cm long paddle counters arranged around the outside of S1 (Figure 2-5a). After each of the first 3 disks of the magnet was a 300 x 300 cm plane of acrylic scintillator (ACR1-3), divided into quadrants, with a 44.5 cm hole in the center (Figure 2-5b). After the 8 disks was a 300 cm square plane, T2, divided in half, and after 16 disks was a similar plane T3. Twenty cm diameter circular counters P1-3 were located next

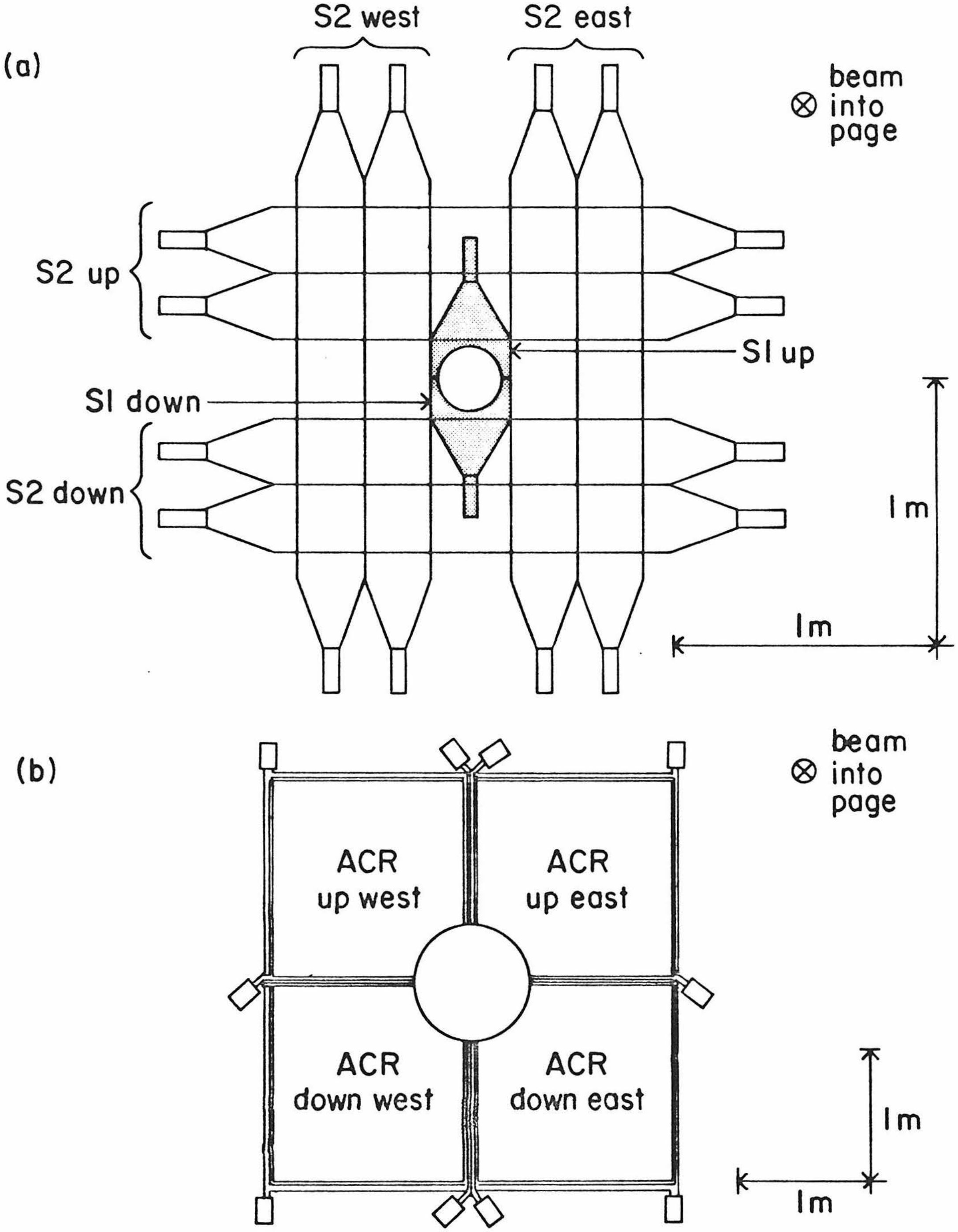

Figure 2-5:

(a) The S1-S2 hodoscope, located just upstream of the toroidal magnets. It was used in the p_t trigger.

(b) An acrylic scintillator plane. There were three such planes installed in the most upstream magnet. These counters were also used in the p_t trigger.

to T2 and T3 and after the last disk. Finally, planes MV (divided into 6 horizontal paddles forming a 150 cm square), S3 (a 150 cm square), and T4 (four quadrants of a 300 cm square) were placed downstream of the spectrometer.

2.8 Data Collection

The data were read out with Camac and with a Unibin into a PDP 11/50 computer and transferred to magnetic tape. The online software was an adaptation of the MULTI system originally written by J. F. Bartlett[15].

The Camac modules were Lecroy 2249A 10-bit ADCs, tagging bit modules, scalers, MTDs, and some non-standard modules[16]. The operation of the special electronics for monitoring the instantaneous rate is described in Chapter 4. The only problem with the electronics worth noting was that the 2249A ADCs exhibited $\sim 5\%$ nonlinearities over the whole range of 1024 channels. The correction required for the nonlinearity was measured for each of the 144 calorimetry ADCs by connecting the input to a counter with an LED attached and varying the voltage applied to the LED.

CHAPTER 3

TRIGGERING

3.1 General Discussion

This experiment had almost 100% acceptance for identifying a muon with $E\mu > 4$ GeV. If the trigger had accepted all these muons, one would expect, from a pulse of 10^5 protons, 2000 events from non-prompt decays and electromagnetic decays. If the production cross section for bare charm were 10 μb and the average branching ratio of charmed particles into muons were 10%, there would be ~ 7 prompt 1μ events per pulse from charm decay. Since the experiment could only handle a trigger rate of approximately 20 events per pulse (because of the spark chamber dead-time), it was necessary to lower the incident proton flux or to tighten the trigger requirements. Lowering the flux would have resulted in the collection of a large number of background events and very few charm events over any reasonable running period. The better alternative was to devise triggers which lowered the absolute rate and also enhanced the signal to background ratio. The muon spectrum from π decay falls considerably faster in p and p_t than does the muon spectrum expected from decays of charmed particles[17]. Hence a minimum cut on p or p_t of the muon could improve the prompt/non-prompt ratio.

The experiment collected data for three weeks with a trigger requiring $p_t > 0.8$ GeV (the p_t trigger) and for one week with a separate trigger requiring $p > 20$ GeV (the high p trigger). For the high p running, the toroid spectrometer was not centered on the N5 beam line, but was shifted 85 cm west so that the high p muons did not enter the central hole (Figure 3-1). The two data sets covered distinct kinematic

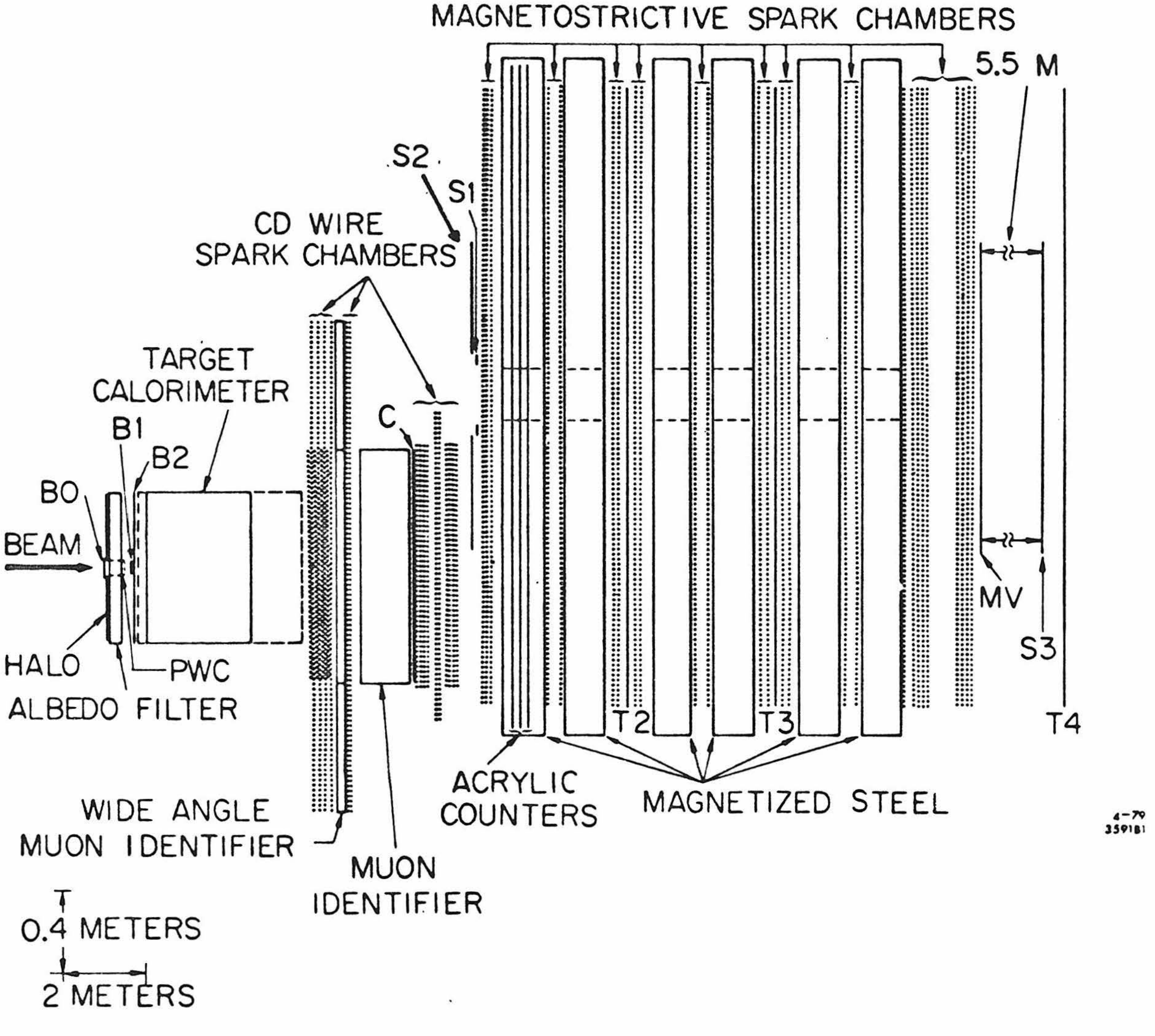

Figure 3-1: The apparatus in the configuration used in the high p data taking (plan view). See Figure 2-1 to compare the configuration used for the high p_t data taking.

regions of D production.

3.2 The IBV Trigger

The clean beam requirement, which was a component of all triggers, was called IBV - Interacting Beam with Vetoes. This signal was separately scaled in two blind scalers, gated on the livetime of the experiment and read after each beam spill, to provide the normalization for the experiment. In addition, the IBV signal went through a prescaler which selected one in 65536 events to trigger the apparatus. These IBV triggers were extremely valuable for monitoring the overall shift in the calorimeter calibration, the absolute rate of out-of-time muon tracks in the spark chambers, and the effect of software cuts on the beam particle. Also, they were used to set independent limits, based on a missing energy search, for production of charm or other kinds of new particles[16,18].

Figure 3-2 is the logic diagram for the IBV trigger. The trigger asked for the coincidence of signals from B0, B1, and B2, and no signal from the halo counter H. (See Chapter 2 and Figure 3-1.) To make sure there had been an interaction near the front of the calorimeter, the sum of pulse height from calorimetry planes 3-10 was required to be greater than 50 times minimum ionizing. The trigger was vetoed by a total pulse height in the calorimeter greater than 600 GeV, which would indicate two interacting particles within the same ADC gate. The signal from BLOB = (B0 + H) • B2 represented a particle incident anywhere in the 76 x 76 cm area of the target calorimeter. A veto on the out-of-time signals from BLOB was added to eliminate particles accompanied by additional beam within ± 90 ns.

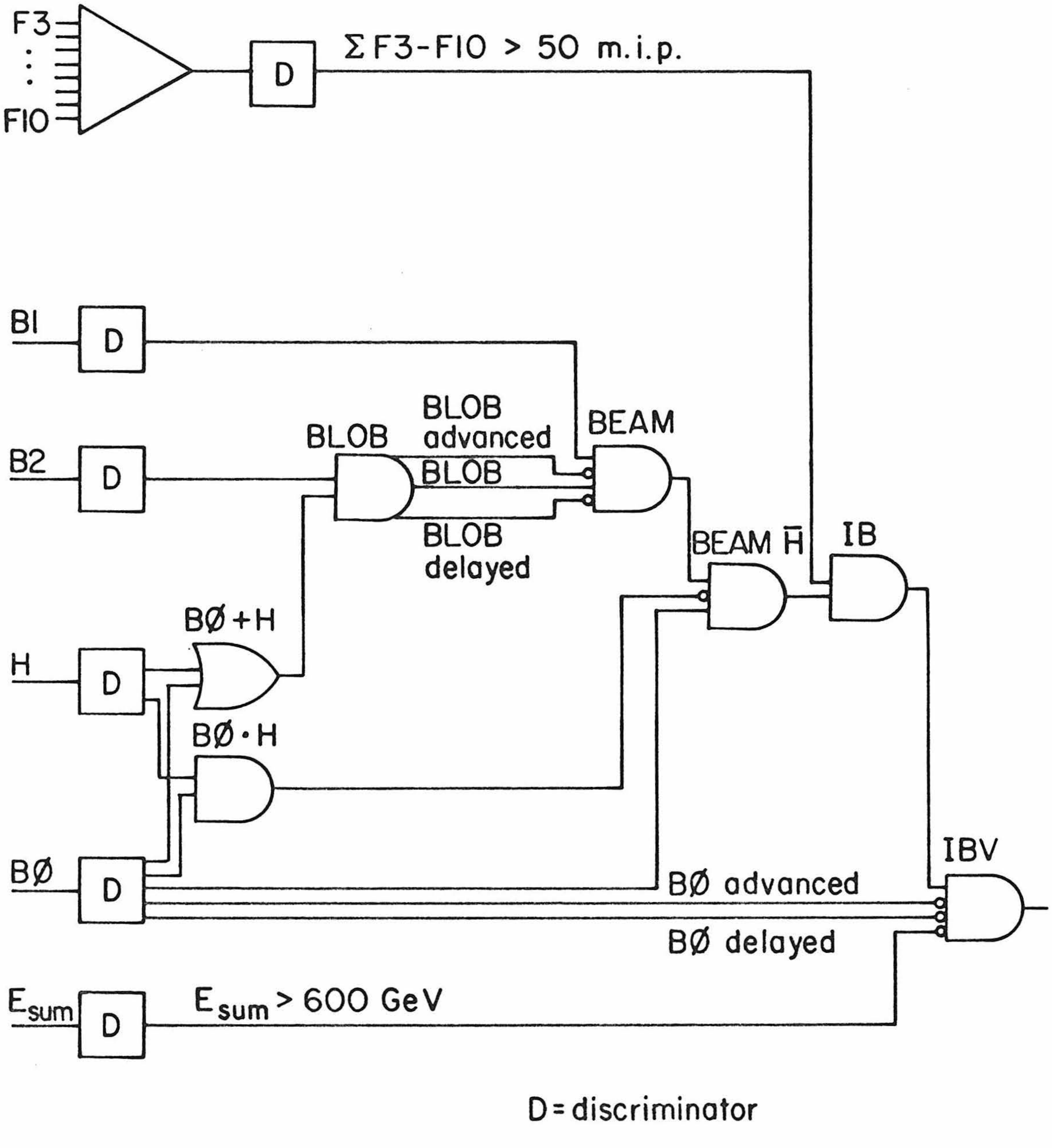

Figure 3-2: The logic diagram of the IBV signal, or clean beam signal, which was required by each of the other triggers and also formed a separate trigger, prescaled by 2^{16}.

3.3 The p_t Trigger

The p_t trigger made use of the focussing properties of the toroids to provide a geometric measure of p_t for focussing (in this case, positive) muons. Briefly, the lower the p_t of the (positive) muon, the sooner the inward p_t kick of the toroids will focus the muon across the axis of the system. Modelling the toroids as a point kick of 2.4 GeV (Figure 3-3), and neglecting energy loss and multiple scattering, the equation for the radius of a muon trajectory after a distance z is

$$r = \frac{p_t}{p} \cdot (z - z_{int}) - \frac{p_{t\ kick}}{p} \cdot (z - z_{cen})$$

if the muon starts at $r = 0$ with momentum p and transverse momentum p_t. Solving this equation for the distance $z = z_0$ at which the muon crosses the axis ($r = 0$) gives

$$z_0 = \frac{p_t \cdot z_{int} - p_{t\ kick} \cdot z_{cen}}{p_t - p_{t\ kick}}$$

Therefore, if $p_t > p_{t\ min} = p_{t\ kick}(z_c - z_{cen})/(z_c - z_{int})$, the crossing point z_0 will always be downstream of z_c, independent of the momentum of the muon. In this simplified picture, a minimum cut on p_t is provided by requiring that the muon not cross the axis until downstream of z_c. Several effects complicate this simplicity, however. Most important are multiple Coulomb scattering, which smears out the value of the p_t cut, and ionization energy loss, which introduces a momentum dependence in the

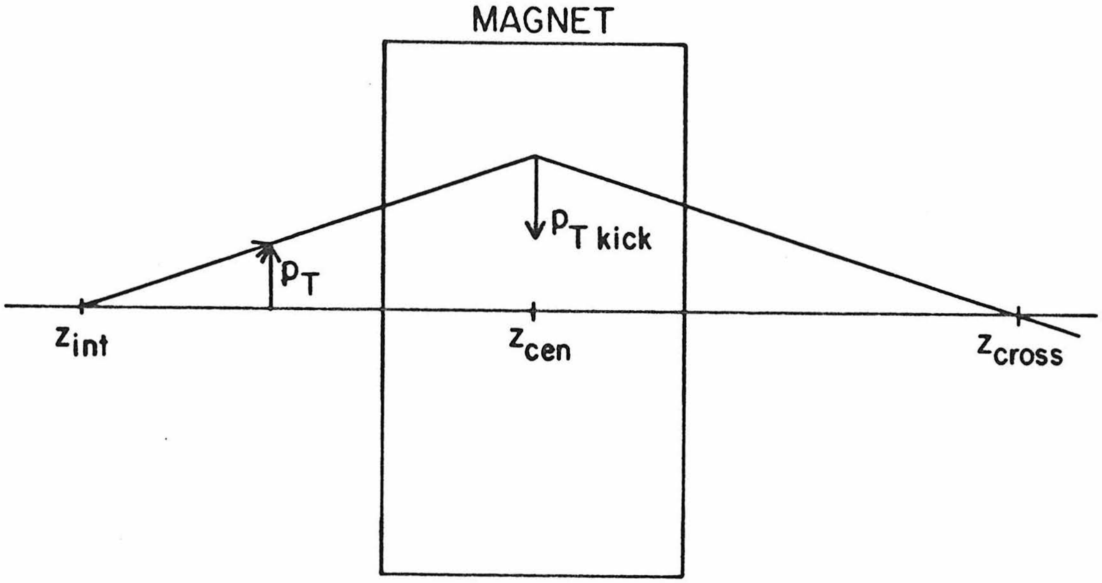

Figure 3-3: A simplified illustration of the concept of the p_t trigger. The value of the transverse momentum of a muon produced at $z = z_{int}$, on the beam axis, is p_T. The total transverse momentum kick delivered by the toroid system is $p_{T\ kick}$. (For positive muons, the kick was directed toward the beam axis.) The z position at which the muon is focussed back across the beam axis is z_{cross}. For larger values of p_T, since $p_{T\ kick}$ is a constant, z_{cross} will be further downstream (for fixed z_{int}). The p_t trigger required that the muon not cross the axis until downstream of a fixed point $z = z_c$. See Section 3.3 for further discussion.

trigger. These effects were even more important because both background and signal have a steep dependence on p and p_t.

The trigger used a set of segmented counters to require a trajectory which remained in the same quadrant of space up to some given longitudinal distance from the interaction. The toroid system was designed to contain 24 quadrant counters, one plane after every 20 cm of steel (see Chapter 2). However, at the time of the run described here, only the first 3 planes were installed. The almost continuous quadrant definition was replaced by counters after each toroid (160 cm of steel). The trigger could therefore be confused by a very low p_t trajectory which crossed and recrossed the axis in between the counter planes. Vetoes in the hole which could cut down the rate of such "S" triggers were undesirable, because the trigger was supposed to be relatively unbiassed between 1μ and 2μ events. The 2μ events contained another class of spurious (low p_t) trigger - the conspiracy trigger in which the positive muon crossed the axis upstream of z_c but the defocussing negative muon happened to be in the quadrant to which it crossed, so that together they provided the signals necessary to trigger. Conspiracy and S triggers were easily removed in the analysis, but they accounted for many of the p_t triggers written on tape. Examples of these trigger types are drawn in Figure 3-4. The small number of negative single muons which fired the trigger were also removed in the analysis.

The logic diagram for the p_t trigger is shown in Figure 3-5. The four parts of the trigger (up-east, up-west, down-east, down-west) represented a signal showing that a muon had traversed the apparatus staying

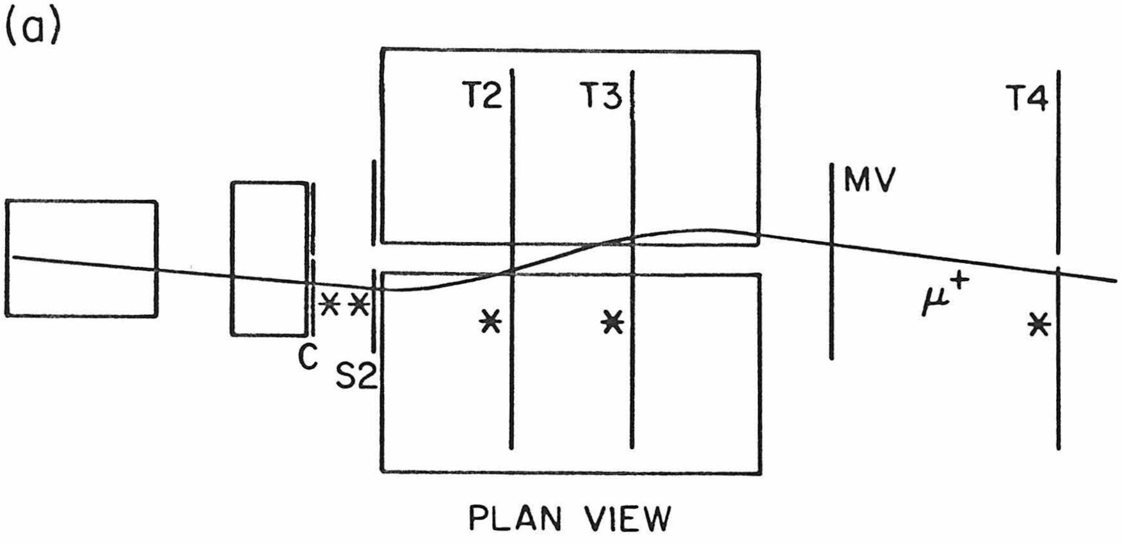

Figure 3-4: (a) "S" trigger. A single low p_t μ^+ provides a p_t trigger by crossing the beam axis from east to west, taking advantage of the lack of horizontal segmentation in counters T2, T3, and MV, and recrossing the axis to give a signal in the proper T4 quadrant.

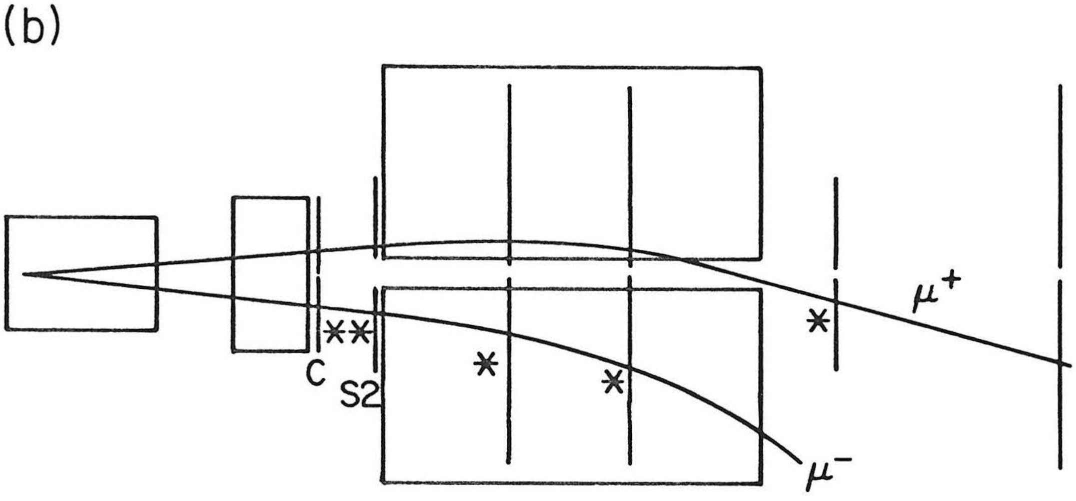

Figure 3-4: (b) Conspiracy trigger. A low p_t μ^+ enters the upper half of the toroids and is focussed into the lower half of MV, failing the trigger requirement. But an accompanying μ^- has entered the lower half of the toroids, giving signals in the lower sections of the upstream counters. These signals plus the MV down signal supply a spurious p_t down trigger.

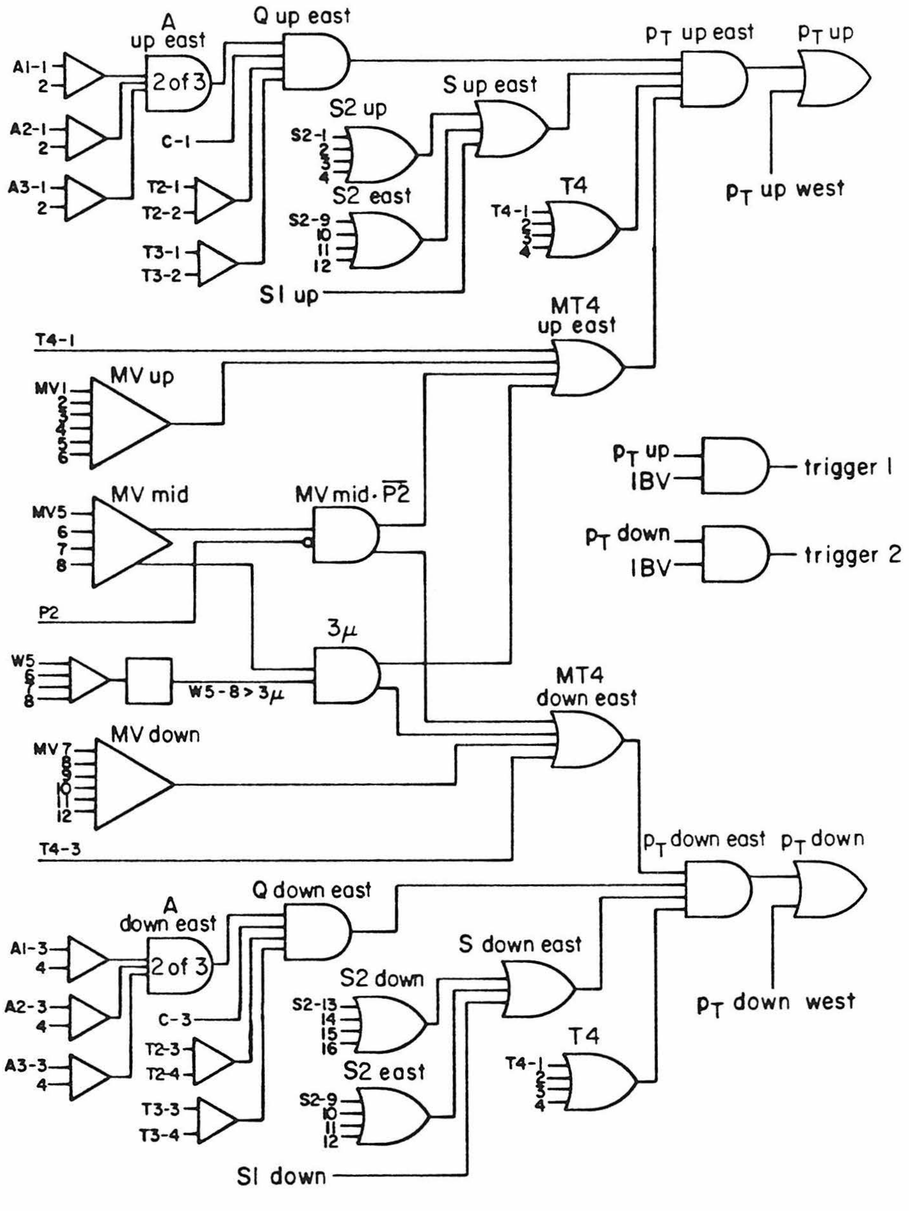

Figure 3-5: The logic diagram of the p_t trigger. The complete logic for the two quadrant triggers p_t up-east and p_t down-east is shown; the logic for the two west quadrants was exactly similar. The logic diagram of the IBV signal is shown in Figure 3-2.

in the appropriate quadrant of space. Two triggers were formed from these parts: p_t up = clean beam·(up-east + up-west) and p_t down = clean beam·(down-east + down-west). The counters forming the four parts were as follows:

$$P_{T\ UE} = C_{UE} \cdot (S1_U + S2_U + S2_E) \cdot A_{UE} \cdot T2_U \cdot T3_U \cdot [MV_U + (MV_M \cdot \overline{P2}) + T4_{UE}] \cdot T4$$

$$P_{T\ UW} = C_{UW} \cdot (S1_U + S2_U + S2_W) \cdot A_{UW} \cdot T2_U \cdot T3_U \cdot [MV_U + (MV_M \cdot \overline{P2}) + T4_{UW}] \cdot T4$$

$$P_{T\ DE} = C_{DE} \cdot (S1_D + S2_D + S2_E) \cdot A_{DE} \cdot T2_D \cdot T3_D \cdot [MV_D + (MV_M \cdot \overline{P2}) + T4_{DE}] \cdot T4$$

$$P_{T\ DW} = C_{DW} \cdot (S1_D + S2_D + S2_W) \cdot A_{DW} \cdot T2_D \cdot T3_D \cdot [MV_D + (MV_M \cdot \overline{P2}) + T4_{DW}] \cdot T4$$

The acceptance of the p_t trigger as a function of p and p_t of the muon in the laboratory is shown in Figure 3-6. The Monte Carlo generation of this acceptance plot included the effects of multiple scattering and energy loss, and assumed that the muon trajectory originated from plate 5 of a compacted calorimeter. The acceptance changed somewhat if the muon originated further downstream (for example, as the decay product of a secondary or tertiary pion) or if the calorimeter were expanded, changing the effective multiple scattering center.

Figure 3-7 shows the acceptance of the p_t trigger versus p and p_t of the parent D meson, in a model where D is produced with $E \frac{d^3\sigma}{dp^3} \propto (1 - |x_F|)^4 e^{-2.5p_t}$, with 40% of its muonic decay into $K^*\mu\nu_\mu$ and 60% into $K\mu\nu_\mu$.

3.4 The High p Trigger

The high p trigger had one important advantage over the high p_t trigger - whereas the high p_t trigger had negligible efficiency for

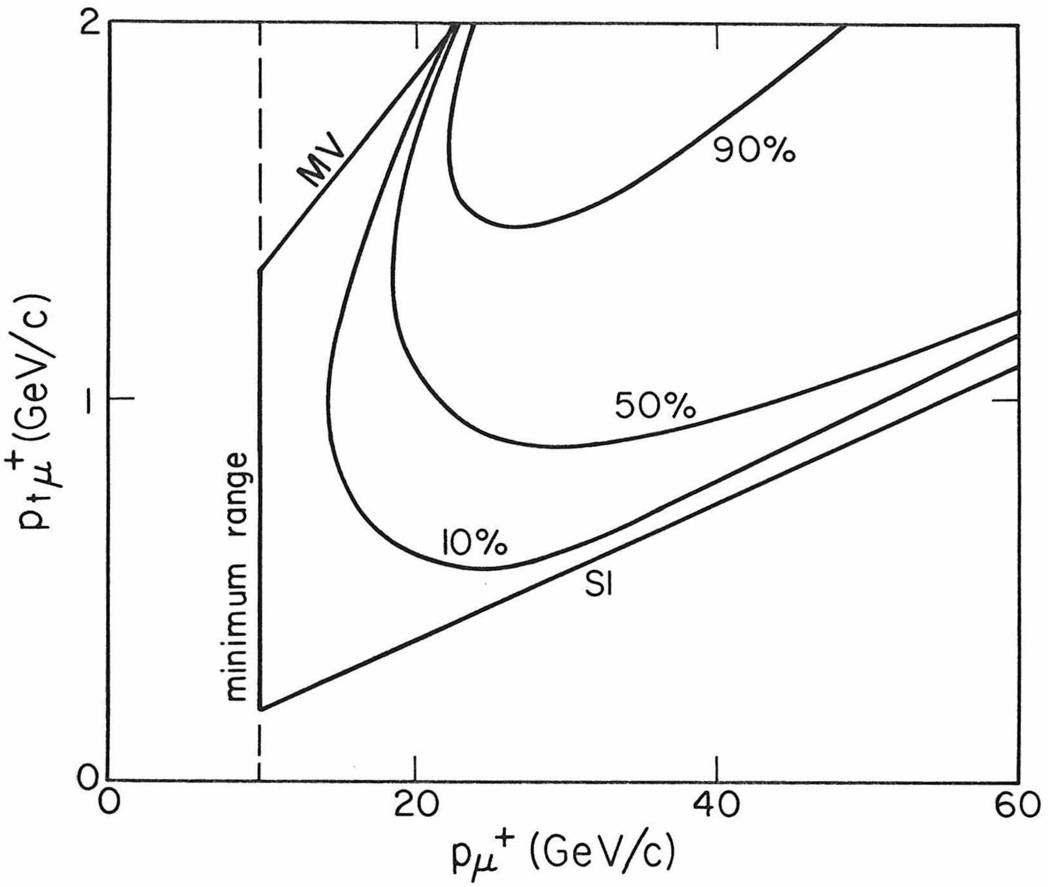

Figure 3-6: Acceptance contours of the p_t trigger. The graph shows the limits of the p_t trigger acceptance calculated using the simplified model of Figure 3-3 (the solid straight lines) and the minimum energy required to penetrate the spectrometer (the dashed line). It also shows contours of constant acceptance as calculated by a Monte Carlo program including the effects of energy loss and multiple scattering.

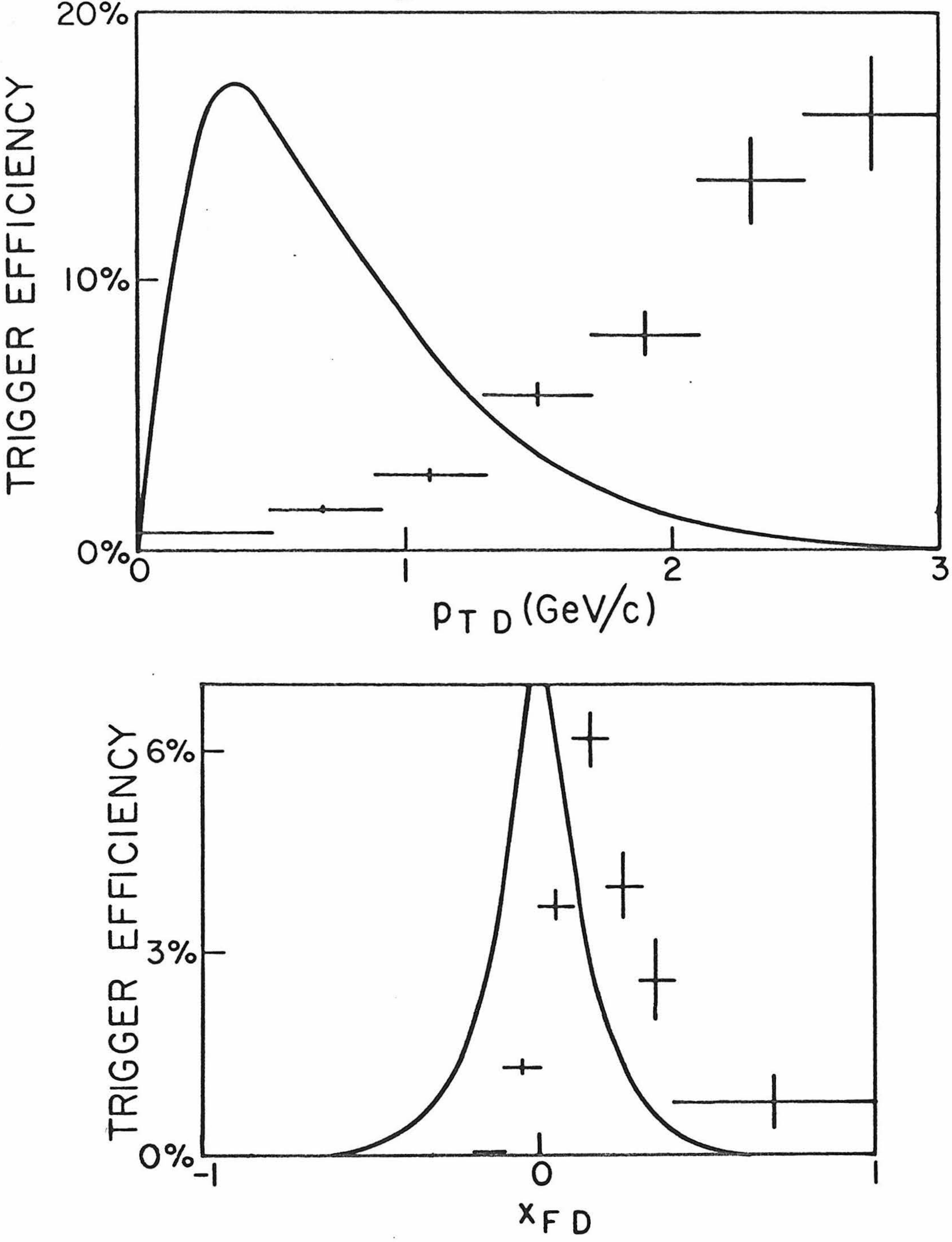

Figure 3-7: The acceptance of the p_t trigger versus p_T and x_F of the parent D meson, using a model in which the D meson is produced with $E\ d^3\sigma/dp^3 \propto (1-|x_F|)^4\ e^{-2.5p_T}$ and $Br(K^*\mu\nu_\mu) = 40\%$; $Br(K\mu\nu_\mu) = 60\%$. The generated distributions (solid curves) are drawn, in arbitrary units, for comparison.

negative muons, the high p trigger had almost equal efficiency for positive and negative muons.

The clean beam (IBV) requirement used for this trigger was identical to that described in Section 3.2. IBV events were again prescaled and written to tape as a calorimetry monitor. The muon requirement asked for muon penetration through the toroid system and for a hit in the counter covering the east half of the toroids (the half which was centered on the beam). The bend angle in the toroid was therefore required to be limited, and thus a lower limit on the momentum was set. Low energy positives (but not negatives) could cross through the hole in the toroids and focus back again to satisfy the trigger, but such events were eliminated in the analysis by requiring at least one muon in each event to have $p > 20$ GeV/c. The logic diagram of the high p trigger is Figure 3-8.

Figure 3-9 graphs the contours of acceptance in p and p_t for positives and negatives. This trigger was useful for a comparison, in the same experiment, of the sign dependence of prompt single muon production. Figure 3-10 compares the acceptance of the high p and p_t triggers and illustrates the small acceptance for D production.

Figure 3-11 shows the acceptance versus x_F and p_t of the parent D mesons assuming the same model as that used in Figure 3-7, described above. The integrated acceptance over these plots is only 3.3%, and the integrated acceptance over the plots of Figure 3-7 is < 3%. The smallness of these numbers represents the major limitation of this experiment in determining σ_{tot} for D production.

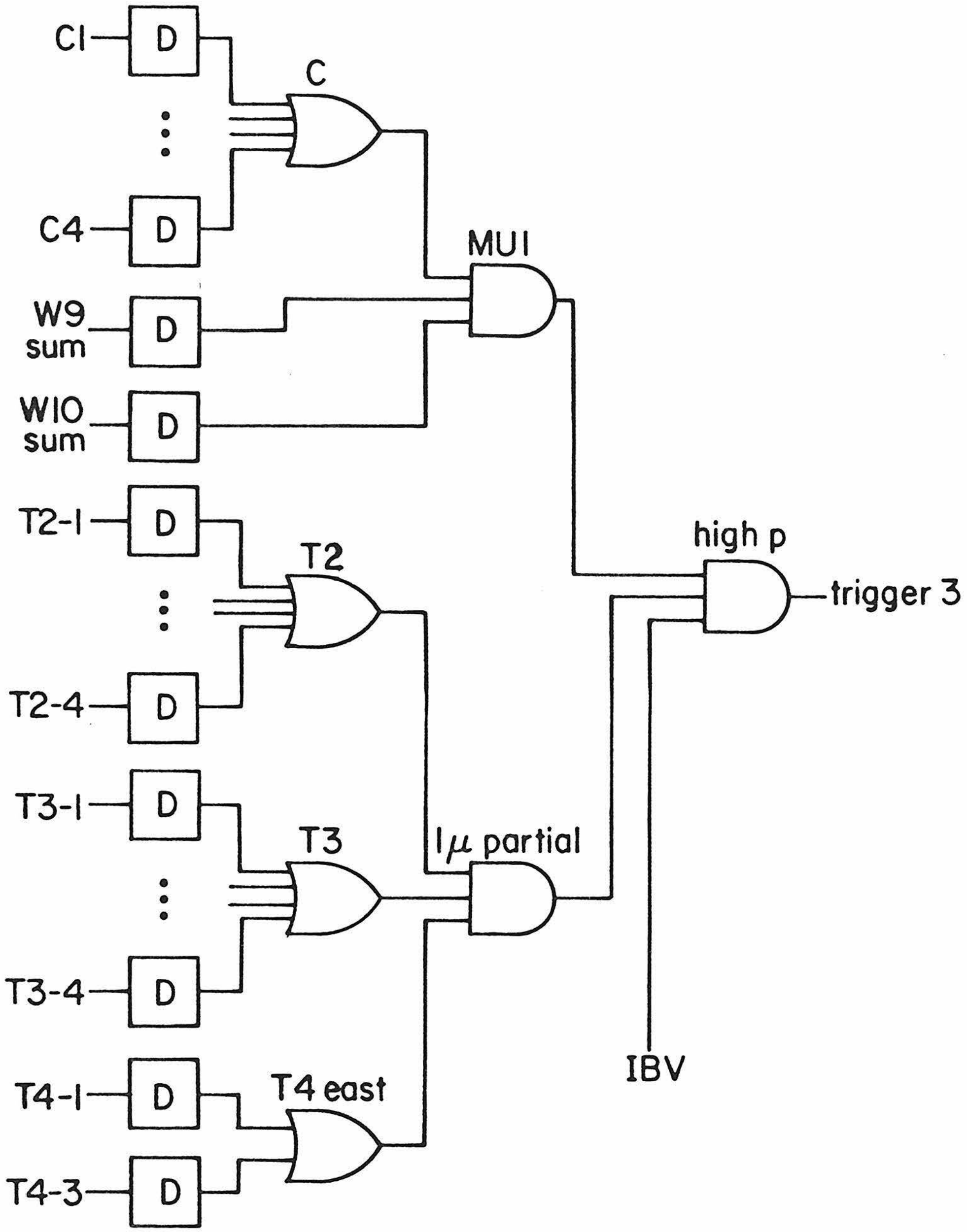

Figure 3-8: The logic diagram for the high p trigger. The symbol D indicates a discriminator. The logic for the IBV signal is shown in Figure 3-2.

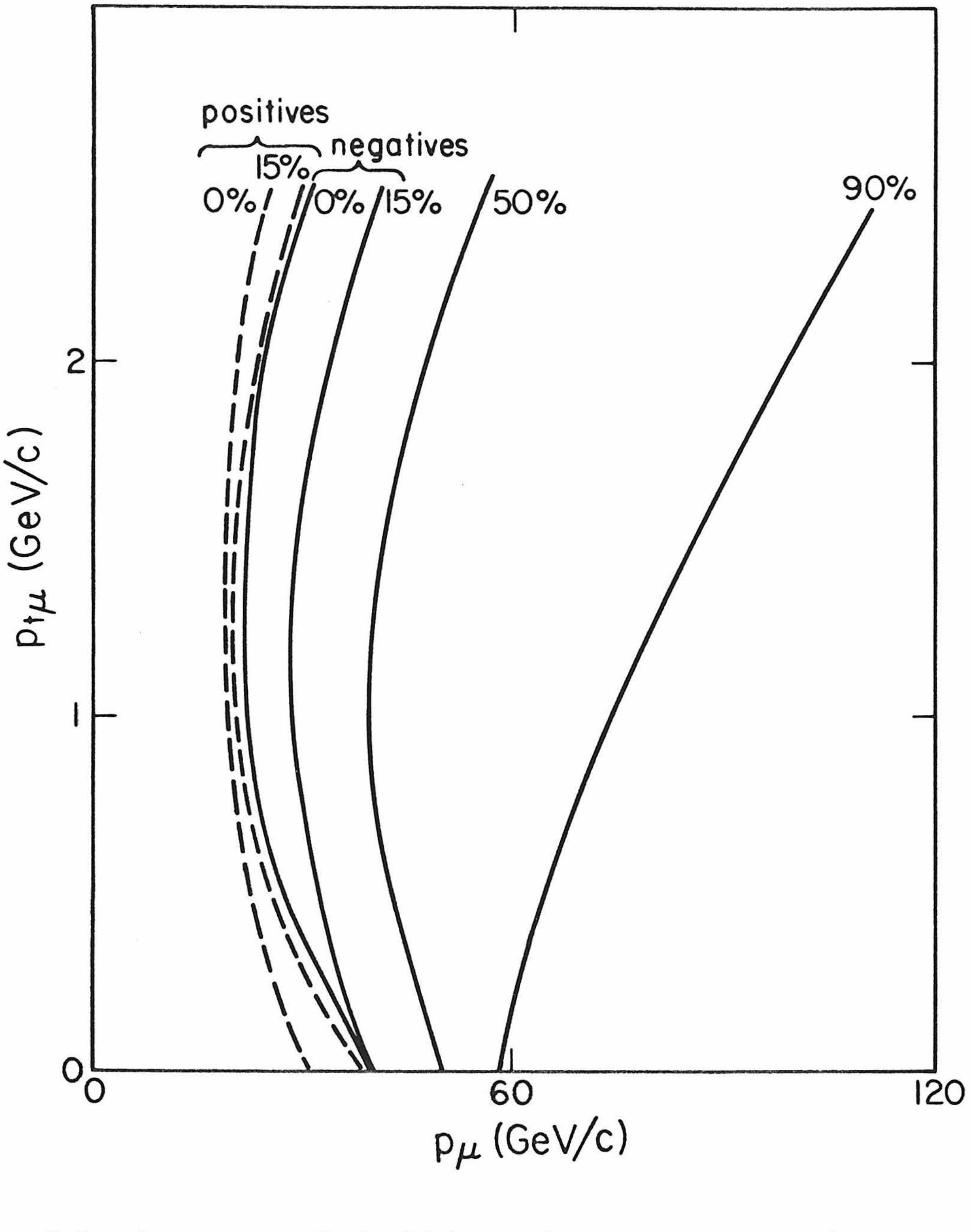

Figure 3-9: Acceptance of the high p trigger versus $p_{t\mu}$ and p_μ. Separate contours are shown for μ^+ and μ^- acceptance at low p_μ; the 50% and 90% contours are the same for μ^+ and μ^-.

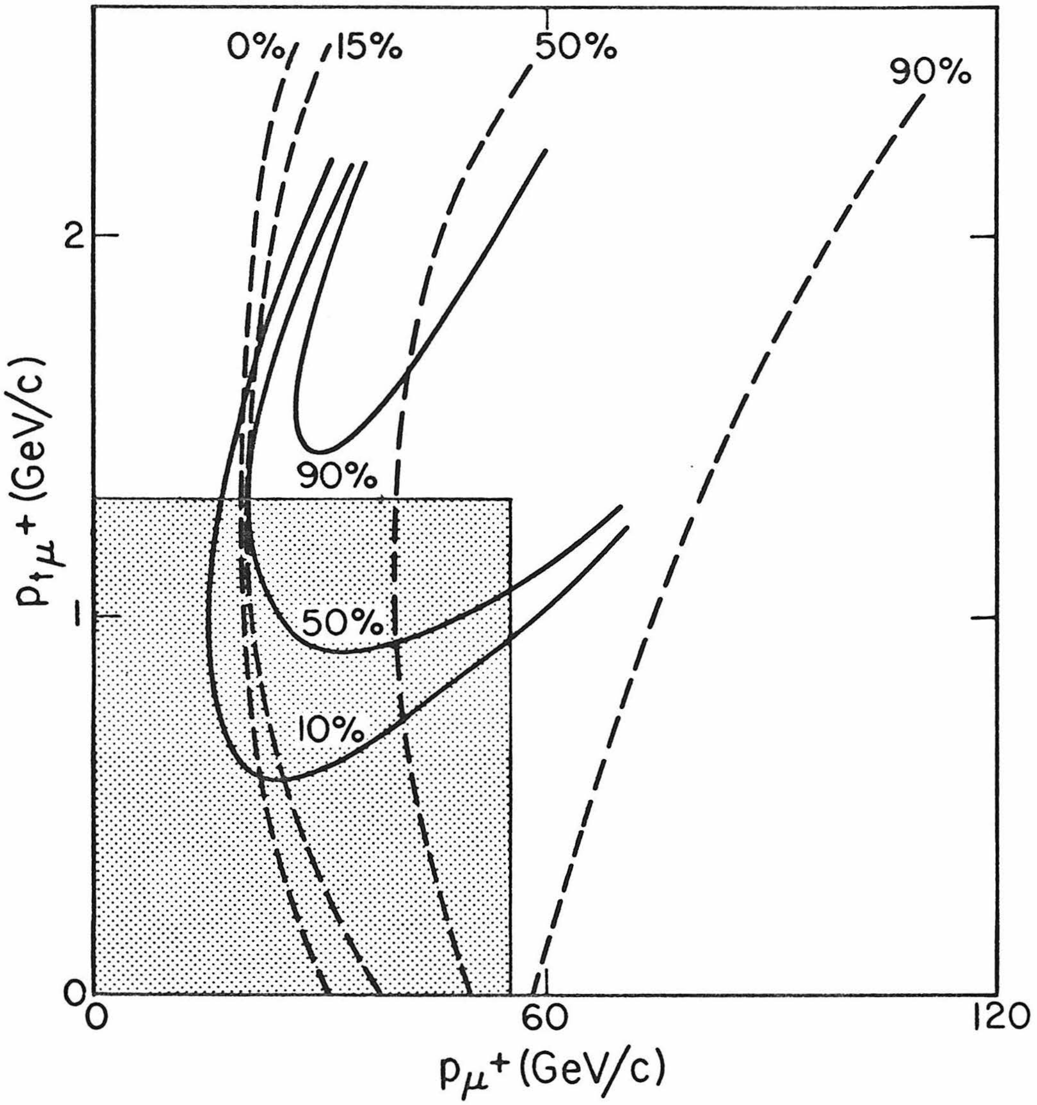

Figure 3-10: The contours of acceptance for μ^+'s from the p_t trigger (solid lines) and high p trigger (dashed lines). The shaded box encloses a region which contains 90% of the μ^+'s from D decay, for most D production models.

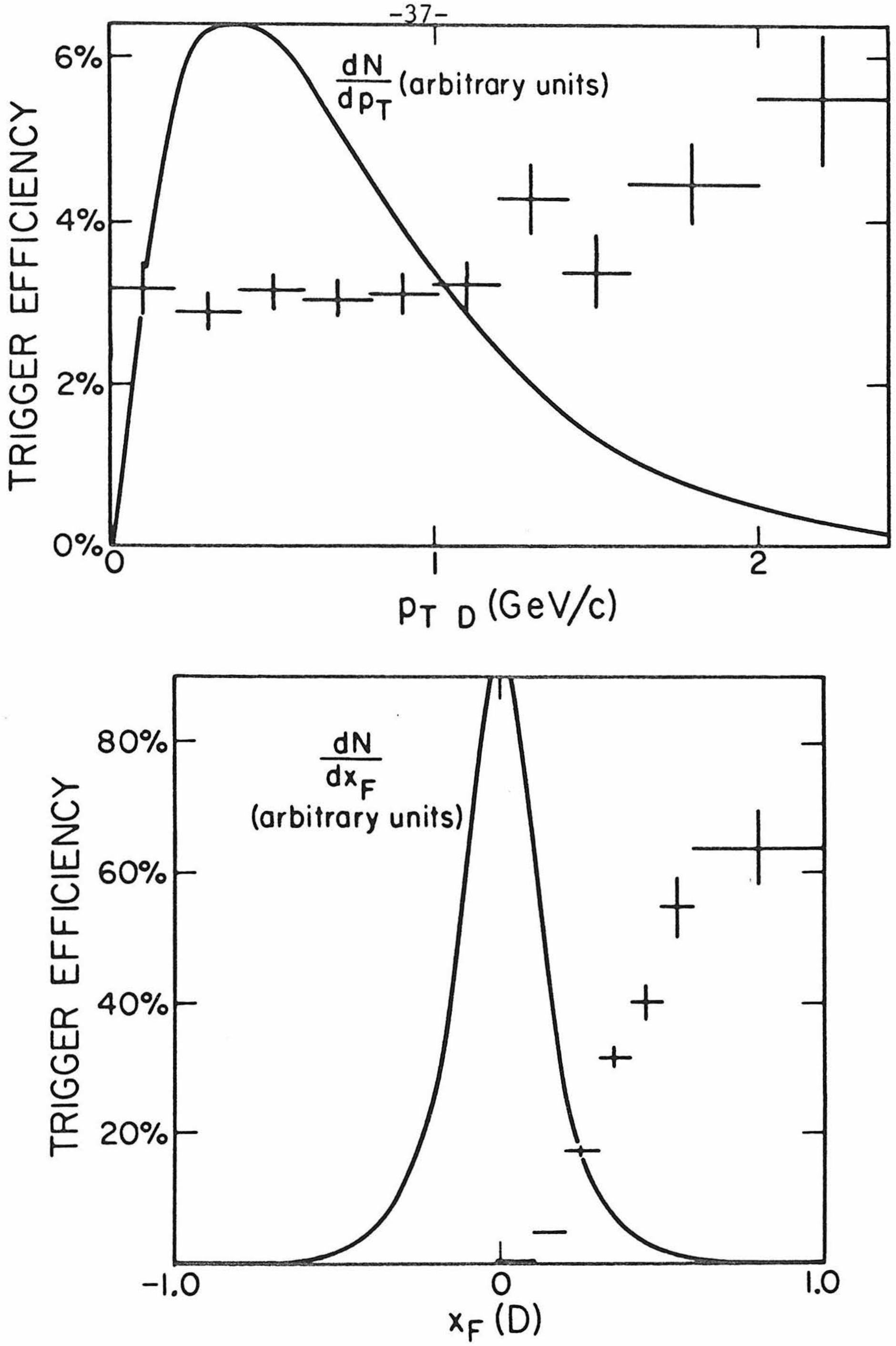

Figure 3-11: The acceptance of the high p trigger versus x_F and p_T of the parent D meson, using a model in which E $d^3\sigma/dp^3 \propto (1 - |x_F|)^4$ $e^{-2.5p_T}$, and Br($K^*\mu\nu_\mu$) = 40%, Br($K\mu\nu_\mu$) = 60%. The integrated trigger efficiency is 3.3%. The generated distributions are shown for comparison.

3.5 Other Triggers Used

A 2μ trigger, prescaled by a factor of 16, was also recorded during the p_t running. It required the clean beam signal, sufficient energy in the last 6 planes of the muon identifier to indicate passage of two minimum ionizing particles, and the penetration of at least one particle through the first toroid. This trigger proved useful as a monitor of the efficiency of the S2 paddle counters, which varied during the run from 70% to 99%. (The efficiency was probably due to an oscillating high voltage supply.) Runs with < 95% efficiency were rejected in the analysis so that any correction for this efficiency was small; the rejected runs contained less than 5% of the data collected.

A low energy trigger was recorded during the high p run which required only the clean beam signal and a signal from the C counters (Figure 3-1) downstream of the muon identifier. This trigger was used to monitor the efficiency of the muon identifier counters used in the high p trigger.

CHAPTER 4

EVENT ANALYSIS

4.1 Purpose of Event Analysis

The task of the event analysis of this experiment was to identify muons in the events and determine their momenta, and to measure the hadronic energy deposited. Also, it was necessary to verify that the muons and the hadronic energy originated in the interaction of one 400 GeV proton (or its cascade) rather than in upstream interactions of the beam or in a second interaction in the calorimeter, nearly coincident with the first. The resolutions in muon momentum and hadronic energy were investigated. The trigger efficiencies and track-finding efficiencies were determined.

4.2 Summary of Data Recorded

Each proton interaction which triggered the apparatus caused up to 1974 16-bit words to be written on magnetic tape. In addition, four special records of calibration and normalization information were written for each beam pulse. The standard event record contained:

(1) tagging bits identifying the trigger and recording the presence of a signal from each of the phototubes on the trigger counters, as well as some logical combinations of these signals

(2) ADC words recording pulse heights representing the energy deposited in the calorimeter and muon identifier counters and some of the trigger counters

(3) ADC words recording pulse heights representing the light seen by the calorimetry counters from the flashing of a spark gap ~ 30 micro-

seconds after the event. The light flash was conducted to the first 31 upstream counters by a bundle of glass optical fibers.

(4) a clock word recording the time of the event trigger relative to the beginning of the beam pulse

(5) a 192-bit shift register counting the beam particles striking the apparatus before the event trigger, in 18.9 nsec intervals, and a similar shift register counting the beam particles arriving before the flash of the spark gap

(6) scalers counting the incident beam intensity during ~ 300 microseconds before the event

(7) words encoding the hits in the PWCs located upstream of the target-calorimeter

(8) spark words from the upstream (capacitor-diode) chambers

(9) spark words from the spectrometer (magnetostrictive) chambers.

The four special records were called the begin spill record, end spill record, pedestal record, and LED record. The begin spill record contained a histogram of the response of the reference phototubes (see Section 2.5) to the ^{241}Am signal during the period between beam pulses. The end spill record contained a similar histogram obtained during the spill, and also the values of scalers counting the incident beam and the firing of counter and logic signals. The pedestal record consisted of ADC values recorded with no signal input. The LED record contained the ADC values recorded when the light-emitting diodes attached to the counters were fired prior to each beam pulse. These values were used to monitor gross shifts in counter calibration while running. Also, the spark gap was fired and the ADC values recorded in the LED record, to measure the response to the flash off the beam spill.

4.3 Extraction of Calorimetry Information

The information from the 45 calorimeter counters and 10 planes of muon identifer counters was used to obtain two parameters of the event, the longitudinal position of the interaction point and the total hadronic energy. To achieve better than 4% energy resolution at 400 GeV required careful calibration and monitoring. The calibration of the counters, using a muon beam and a low intensity 400 GeV proton beam, was described briefly in Section 2.5. For greater detail, see Reference 16. From the calibration procedure emerged a set of constants for converting the ADC channel number into the number of equivalent minimum ionizing particles (m.i.p.). The exact procedure for obtaining the energy was as follows.

(1) Subtract the average pedestal value (offset) from each ADC.

(2) Correct the channel number for nonlinearity using the form $C_{true} = C_{meas}^{a_i}$, where a_i was a constant measured for the i^{th} ADC (see Section 2.8). Most of the constants a_i were less than 5% different from 1.000.

(3) Correct for saturating ADC channels by using the very low gain ADC channels called superlows, which analyzed the pulse height in the sum of each seventh counter; i.e., superlow 1 = counter 1 + counter 8 + counter 15 + ... + counter 43.

(4) Divide by the standard calibration constants for each counter to obtain the equivalent number of m.i.p. x inches.

(5) Correct each of the upstream 31 counters for long term drifts

in the phototube gains (where long term means over a period of hours or days). Only the first 31 counters had optical fiber monitoring, but typically only 3% of the energy was deposited downstream of the monitored counters. The drift was calculated by taking the current average ratio of spark gap signal in counter i to spark gap signal in reference tube 1 and dividing this by the same ratio measured when the counters were calibrated. The result was then multiplied by the drift in reference tube 1 to obtain the drift in the phototube gain for counter i. The drift in reference tube 1 was calculated by taking the ratio of the means of the Am signals in reference tube 1 at the current time compared to the calibration time.

(6) Sum the corrected signals from the 55 planes and multiply by a constant to obtain the total energy in GeV. The constant was determined by comparing the mean pulse height of muonless beam interactions to the beam energy of 400 GeV.

(7) Correct the total energy for effects due to the beam intensity. One effect was the presence of tails of the energy pulses from a preceding event. These tails extended for ~ 300 nsec with approximately an exponential decrease in size. The shift register which located beam particles preceding the event to within ~ 20 nsec was used to correct this effect. The second correction involved the shift in phototube gains which occurred at large instantaneous intensity. Scalers recorded the instantaneous intensity over about 300 μsec before the event, and the fractional change in energy as a function of the integrated intensity was determined from its effect on the spark gap pulse height. This

function was then used to correct the calorimeter energy. For a much more complete discussion of these effects, see Reference 16.

The resolution versus beam energy varied as $\frac{a}{\sqrt{E}}$ and is shown in Figure 4-1a; the linearity of the calorimetry measurement versus beam energy is shown in Figure 4-1b. Figure 4-2 shows the energy distribution for 400 GeV interacting protons on a logarithmic scale.

The general algorithm for finding the steel plate i in which the interaction occurred was to define i as the first plate for which the energy in counter i was greater than n_1 m.i.p. and the energy in counter i + 1 was greater than n_2 m.i.p. Two sets of values were used; $n_1 = n_2 = 30$ in the high p_t analysis and $n_1 = 10$, $n_2 = 30$ in the high p analysis. There was no appreciable difference in muon rates based on the choice of values. Both analyses required $i \geq 1$ and $i < 9$; i.e., an interaction in the first 30.5 cm of steel. The value $i = 0$ meant an interaction upstream of the first calorimeter plate. We excluded $i > 9$ in order to ensure longitudinal containment of the shower, and to minimize those backgrounds which were generated from energy deposited in the downstream quarter of the calorimeter. (See Section 5.6.) The definition of i is illustrated in Figure 4-3.

4.4 General Remarks on Track Reconstruction

The first step in track reconstruction was of course the conversion of the spark words from the CD and magnetostrictive chambers to spark positions in centimeters. The two sets of chambers had quite different types of readout. For the CD chambers, the readout electronics encoded the identification numbers of the wires which conducted a signal from the

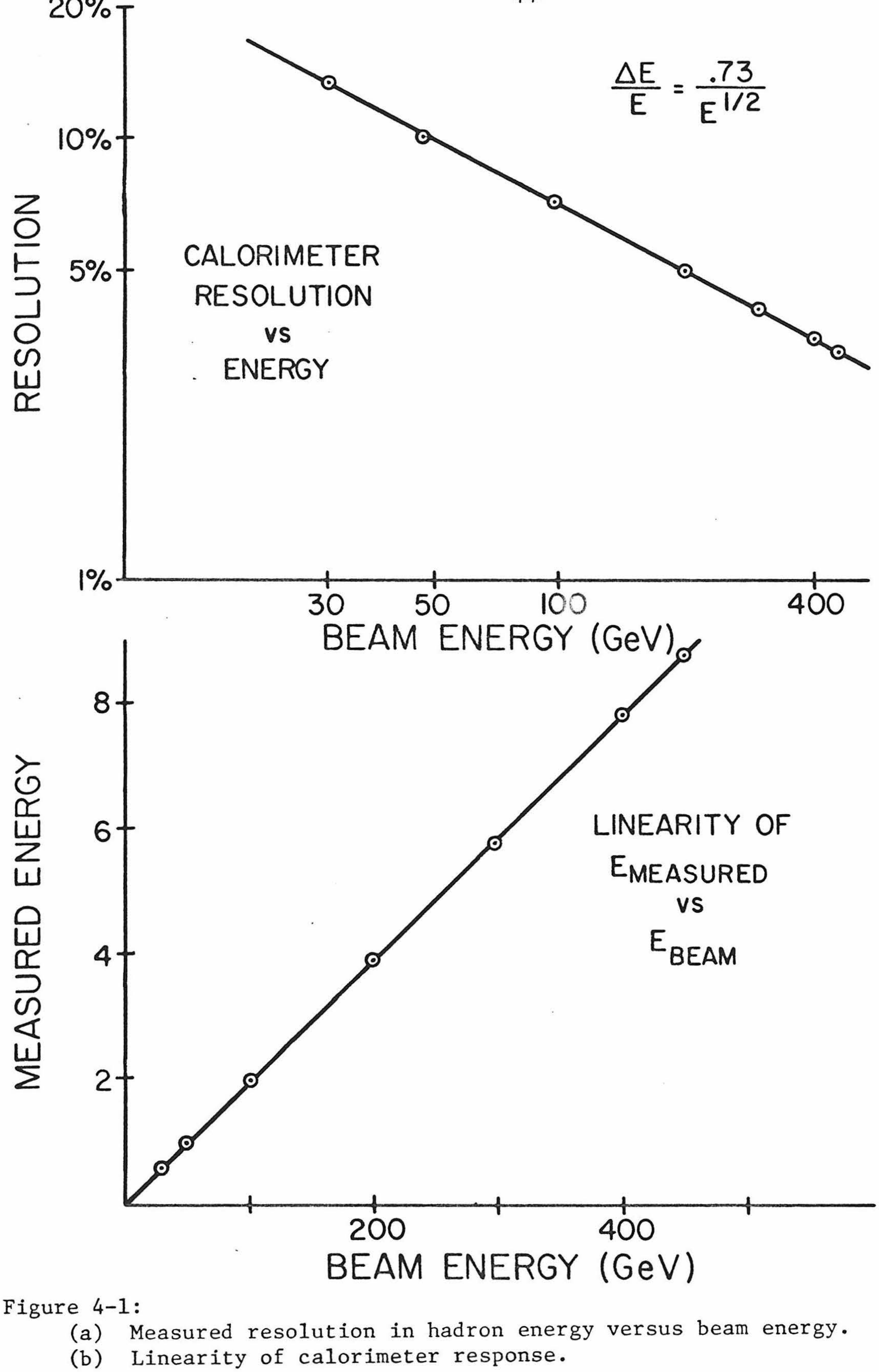

Figure 4-1:
(a) Measured resolution in hadron energy versus beam energy.
(b) Linearity of calorimeter response.

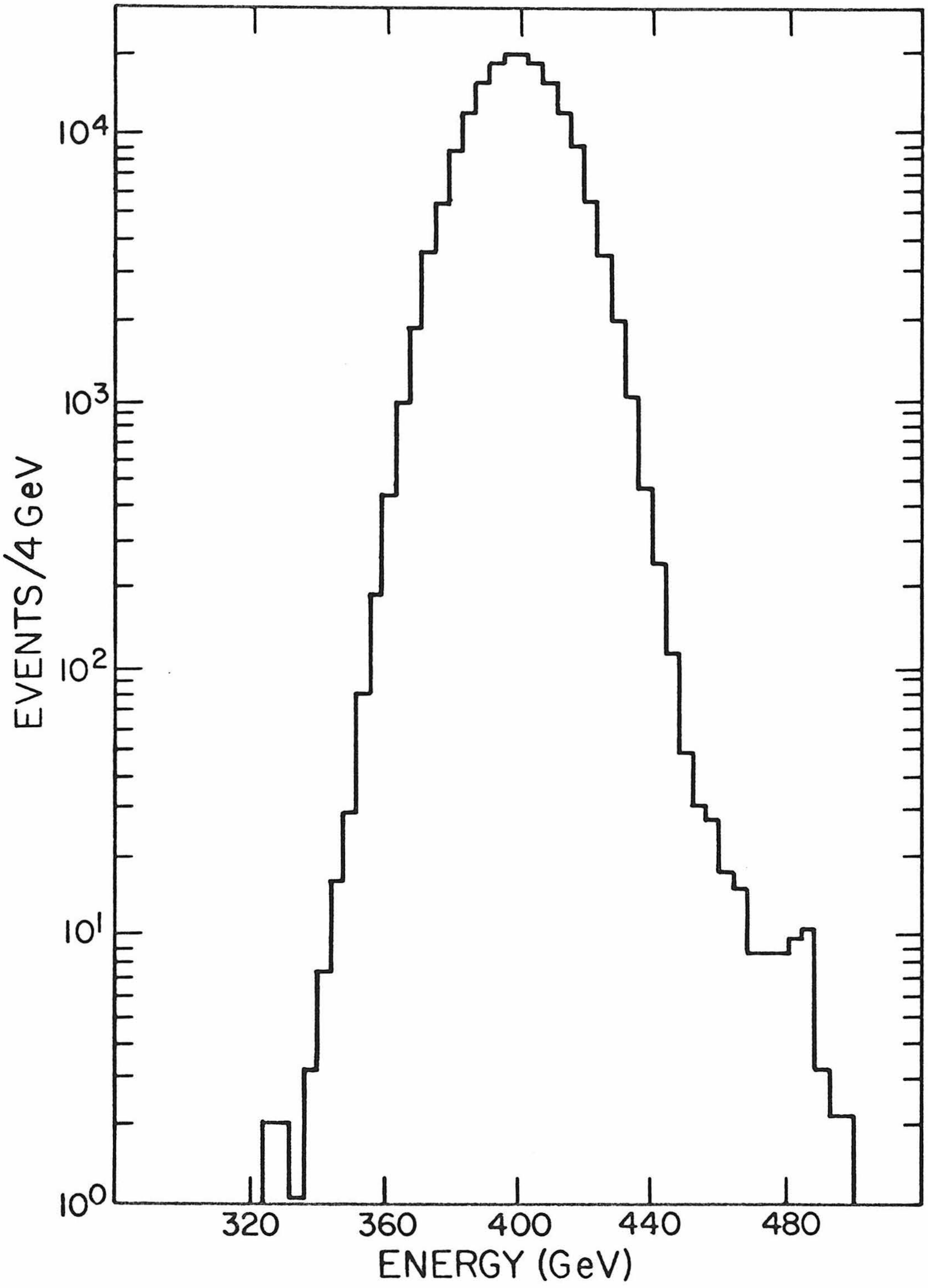

Figure 4-2: Measured energy distribution of 400 GeV interacting proton events with no muon track. (Figure taken from Reference 16.)

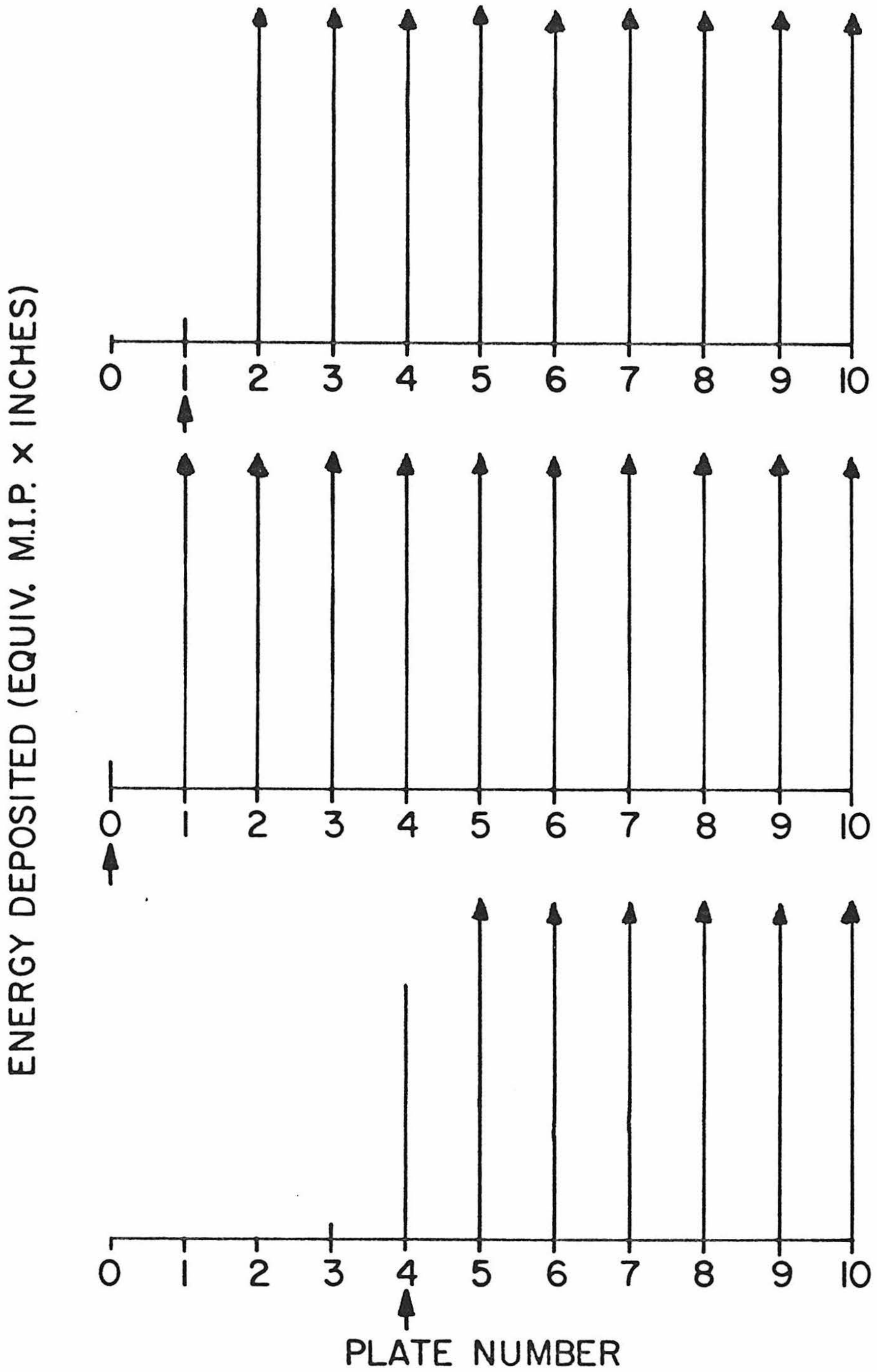

Figure 4-3: For three typical events, the energy in each calorimeter counter is plotted versus the plate number, and the small arrow indicates the plate assigned as the beginning of the shower, i. The event with i = 0 was rejected in the analysis as a possible interaction upstream of the calorimeter.

spark, and the wire number corresponded directly to a known position in space. The magnetostrictive chamber readout digitized the time required for a longitudinal pulse, generated in a magnetostrictive wire by the magnetic field of the spark, to travel across the chamber. The speed of these pulses in the wire was continuously measured with fiducial pulses, and using this speed the spark time was converted to a spark position. With all sparks converted to centimeters using a uniform coordinate system, the different sets of chambers could be treated identically.

Identification of muons emerging from the calorimeter involved finding a track in the CD spark chambers upstream and downstream of the muon identifier. Measurement of the sign and momentum of muons involved finding a track in the spectrometer (magnetostrictive) chambers. The high p_t and high p data analysis used independent programs for both track-finding problems, although the CD chamber configuration did not change between the two data runs. The following section discusses the programs used for the high p analysis (the CIT system) and points out the differences in the SLAC system, which was used for the high p_t analysis, where they are relevant. Separate alignment runs using a muon beam were taken for the high p_t and high p configuration, with the toroids degaussed. Muons produced in the proton shower passed through 2 to 3 meters of steel before entering the first set of chambers (see Figure 2-1). Hence the resolution on the transverse position of the trajectory at the interaction point was poor; sufficient, however, to determine that the muon did not come from outside the steel of the calorimeter. The upstream CD chambers frequently registered hadron tracks emerging from the calorimeter, but these tracks were absorbed in the one meter of steel in the muon identifier. A track in the CD chambers downstream of the identifier was considered a muon. Because the CD chambers had a long memory time for sparks (~ 3 μsec), there was a probability of $\sim 0.5\%$ for each event, at our highest running intensities, of having an out-of-time muon track recorded by the chambers. These tracks could easily be flagged by the program, however. The tagging bits and pulse heights in counters were required to be consistent with the observed trajectory. Even for the lowest energy identifiable muons (~ 4 GeV/c in momentum), there was considerable redundancy in this determination, for the track passed through 10 planes of muon identifier counters and two planes of trigger counters, all hodoscoped. These counters were also used in the high p analysis to identify muon tracks lost due to inefficiency in the spark chambers.

The downstream CD chambers together with the front toroid chambers provided a good measurement of the track angle entering the toroid steel. Eleven more planes of chambers were interspersed with the toroid sections to record the trajectory through the magnetic field. Then came a final set of six planes, called the cart chambers, which measured the exit angle.

4.5 Track Reconstruction Upstream and Downstream of the Toroids

Tracks were reconstructed in the three steel-free regions containing spark chambers using the same set of routines. A search was made in the x and y dimension such that any segment with 3 or more sparks was found. The x and y segments were matched using the u-v sparks in that region; there were 1, 2 and 1 u-v planes respectively in the upstream CD, downstream CD, and cart regions. The one u-v plane in the cart region had a large vertical gap in the center, so an additional matching routine which required the same pattern of hits and misses in x and y for matched segments was used. The upstream and downstream CD u-v matched tracks were extrapolated to the center of the muon identifier and matched, taking multiple scattering into account to set the windows. Various routines were employed to correct for possible errors: eliminating tracks with too many common sparks, searching for matches without relying on the u-v planes, and allowing 2-spark segments in either x or y to match a good segment in the other view.

4.6 Track Reconstruction and Momentum Fitting in the Toroids

In the high p analysis, the procedure for finding a track within the toroid involved finding sparks such that the angular momentum L_z about the toroid axis was constant, using the knowledge that this quantity was conserved except for the effects of multiple Coulomb scattering. This technique was applicable to data with the toroids centered on the beam axis or not centered, the difference between the two cases being only that $L_z = 0$ if the toroids were centered. In the high p_t data for which the toroids were centered, this technique was not used, but the results of the two independent programs were compared on a sample of data and found to be consistent. The initial value of L_z was obtained from the entering CD track or the exiting cart track. Cart tracks were used first, since 2μ events were easier to disentangle after the positive and negative tracks were separated by the field. A toroid track being traced upstream from the cart was matched with a CD track if possible, and discarded if not matched. After tracing all cart tracks, all unmatched CD tracks were traced downstream. Then the resulting complete tracks went through a momentum-fitting procedure which continued to add and delete sparks to improve the fit. The initial value given to the momentum came from fitting a circle to the longest upstream arc of sparks not entering the toroid hole, and obtaining the momentum from the radius of curvature. The fitting routine assumed that χ^2 was quadratic in 1/p and iterated between 5 and 10 times, allowing spark additions and deletions each time. A fit was accepted if it retained at least two good sparks after the final iteration, and the first spark was upstream of the third toroid. The momentum resolution of 11% was measured using both Monte Carle events and an incident muon beam of known energy, and the distribution of Monte Carlo events is shown in Figure 4-4.

4.7 PWC Track-Finding

The program required a hit in at least 3 of the 4 beam PWCs, in both x and y, to define a beam track. The procedure for the y track was simply a straight line search. In the x view, the 16 mrad bend was subtracted and then the x sparks were also fit with a straight line.

4.8 Counter Efficiencies

The high p_t trigger involved the coincidence of signals from a minimum of eight planes of scintillation counters (Section 3.3), and the high p trigger required signals from six planes (Section 3.4). To know the efficiency of the trigger, it was necessary to measure the efficiency of each of the counters for detecting a single minimum ionizing particle.

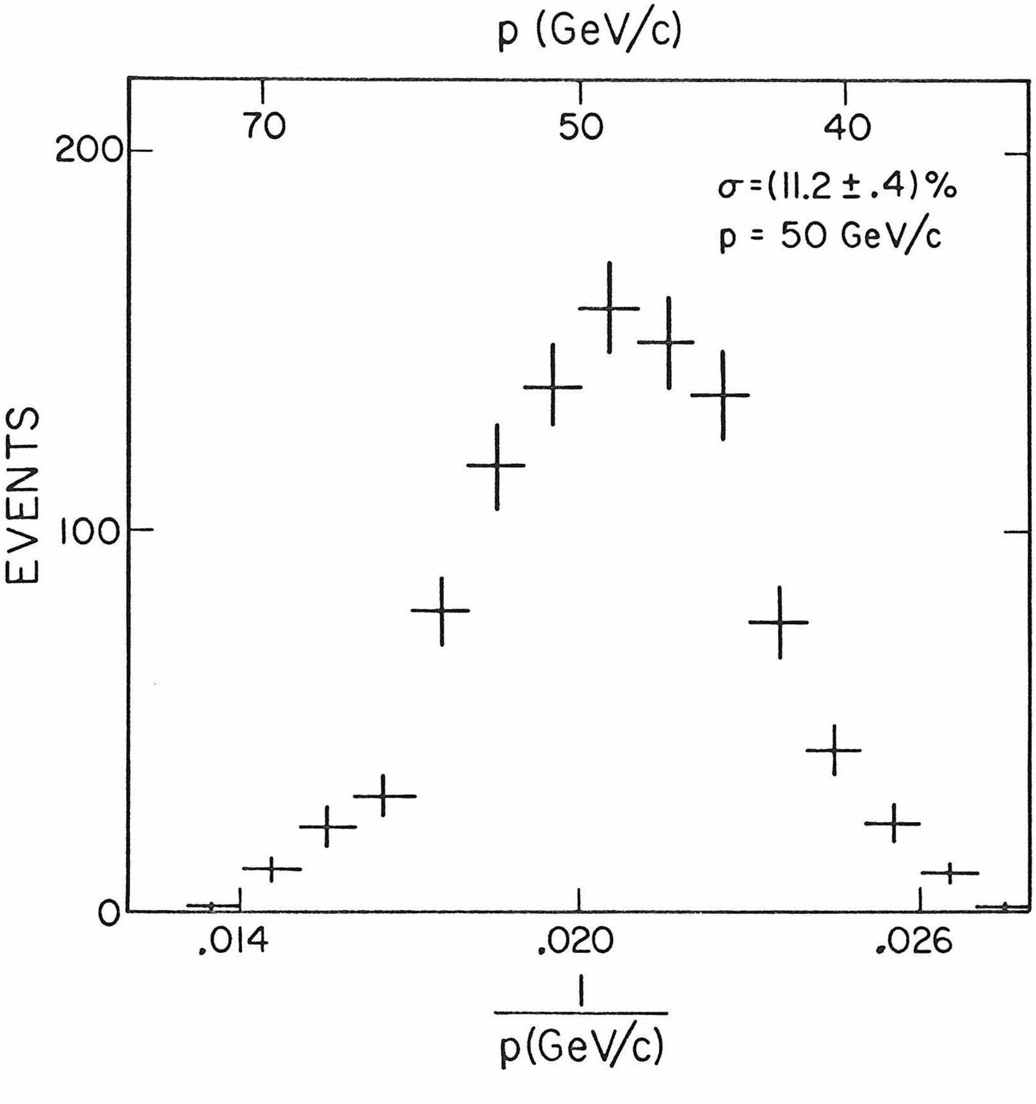

Figure 4-4: Measured distribution in 1/p from a Monte Carlo tape of monochromatic 50 GeV/c muons.

There were two possible methods for these measurements. If another trigger used during the run did not require one of the counters, its efficiency was easily measured using that trigger since all scintillation counter signals were tagged with a coincidence latch. The two triggers used for this purpose were described in Section 3.5; the interacting proton trigger was not used because the low rate of muons in these triggers combined with the relatively small number of events collected meant that the statistics of any efficiency measurement were too low to be useful. For some of the hodoscoped counters, the efficiency was measured using events with two muons entering different hodoscope counters, by requiring one track to satisfy the trigger and studying the efficiency of the hodoscope using the other track. The acrylic counters were known to be inefficient for single minimum ionizing particles, so the acrylic requirement in the high p_t trigger asked for only 2 out of 3 planes; this combination was efficient.

The results of these studies were that all the counters used in the high p_t trigger had > 98% efficiency except the S2 hodoscope, which during a few runs dropped to 70% efficiency. These runs contained so little data that they were simply discarded in the analysis. All counters in the high p trigger were found to be efficient except the muon identifier hodoscope counters. Their efficiency varied with time and also was different for each of the four quadrants. The efficiencies were measured with the low energy trigger (Section 3.5) by extrapolating the muon track to determine which counter it entered, and using the coincidence latches to determine whether the counter fired. The measured efficiency for 2μ events suggested that the two tracks contributed independently to the trigger probability of the event. See Section 5.2 for the table of values of these efficiencies and for discussion of how they were included in the analysis.

CHAPTER 5

HIGH P DATA ANALYSIS

5.1 Introduction

The high p trigger was described in Section 3.4. To review, for this trigger the toroid spectrometer was displaced 85 cm west of the beam axis so that the high momentum muons, which traveled nearly straight down the beam axis, no longer entered the hole in the toroids. (See Figure 3-1.) The condition of high muon momentum was imposed in the trigger by limiting the displacement of the track to ± 88 cm from the beam axis at a longitudinal distance of ~ 700 cm from the center of the toroids. The acceptance of the trigger for negative muons rose from zero at 20 GeV/c to 100% at ~ 60 GeV/c. The acceptance for positives was similar above 20 GeV/c, but positives lower than 20 GeV/c could trigger by crossing the toroid axis and being refocussed into the momentum-defining counter, T4 east.

5.2 Trigger Efficiency

As described in Section 4.8, the W9-W10 summed signal, which was part of the high p trigger, was inefficient for triggering on one minimum ionizing particle. The efficiency for triggering on a particular muon depended on which of the four W10 counters the track went through, so a weight was assigned of $1/\varepsilon i$, $i = 1, 2, 3$ or 4. If an event contained more than one muon track, the total weight was computed assuming the probability of triggering W9-W10 was independent for each track; i.e., the event weight $= 1/\varepsilon$, where $\varepsilon = \varepsilon i + \varepsilon j - \varepsilon i \cdot \varepsilon j$, for an event with one track through counter i and one through j. The mean efficiencies for 1μ and 2μ events are given in Table 5-1 for the data from each of the three density configurations.

5.3 Normalization Corrections and Cuts

The first software selection criteria were directed toward assuring a clean proton interaction. The criteria were (1) no more than one track in the PWCs upstream of the calorimeter, (2) less than 0.3 x minimum ionizing in the halo counter, and (3) a longitudinal interaction position, calculated with the algorithm described in Section 4.3, within the upstream 30.5 cm of the target calorimeter (the first 8 steel plates). These same cuts were applied to the sample of clean beam (IBV) triggers, with no muon track, collected concurrently with the high p trigger. Approximately 18% of the IBV events were removed. This efficiency factor was then put into the calculation of the high p trigger rates.

Another software efficiency correction was needed because events with detected hardware errors likely to interfere with track reconstruction were thrown out. This correction, like the beam cut correction, was made separately for each density so that any variation of the effect of the cut with time did not introduce an error in the extrapolation of rates to infinite density. Table 5-2 gives the raw number of interacting protons, counted during the livetime of the experiment, and the corrections to the normalization for each density.

5.4 Definition of 1μ and 2μ Categories

The first step in defining 1μ and 2μ samples was to define good tracks; i.e., tracks associated with the proton interaction in the calorimeter and not with beam halo or out-of-time interactions. Halo particles inside an area of 76 x 76 cm around the beam were vetoed, but tracks

Table 5-1: W-10 Counter Efficiencies

Density	$\langle \varepsilon_{1\mu}+\rangle$	$\langle \varepsilon_{2\mu}+\rangle$	$\langle \varepsilon_{1\mu}-\rangle$	$\langle \varepsilon_{2\mu}-\rangle$
Compacted	.862	.958	.901	.958
Semi-expanded	.914	.973	.948	.974
Expanded	.842	.946	.896	.949

Table 5-2: Total Number of Protons at Each Density

Density	measured # of protons	fraction removed by beam cuts	fraction removed by hardware errors	corrected # of protons
Compacted	2.920×10^8	.179	.0190	2.342×10^8
Semi-expanded	1.277×10^8	.179	.0493	9.858×10^7
Expanded	1.301×10^8	.172	.0465	1.016×10^8

outside that area would miss the halo counter. Tracks were extrapolated back to the interaction point in the calorimeter and the transverse position there was calculated. If the position lay outside the area of the calorimeter, the track was called a halo track and rejected. The distributions in transverse position are shown in Figure 5-1. Next, each track was extrapolated to determine which of the muon identifier counters and trigger counters it entered. If these counters did not fire, the track was flagged as out-of-time and rejected. The muon identifier counters were particularly helpful in this determination because their signals were pulse-height analyzed and could be used to discriminate between 1 and 2 in-time particles even if the two tracks went through the same counters.

The next cut applied was to require each event to have at least one good track of momentum $p > 20$ GeV/c. The effect of this cut was to eliminate the low energy positive μ's which triggered by refocussing across the toroid axis (see Section 3.4).

Looking at the distribution in number of in-time tracks (including halo tracks) per event, it was found that approximately 1% of the events had no in-time track. Considering the trigger requirement of a penetrating particle all the way through the spectrometer, one should find a muon track in all events. Inspection of computer-drawn pictures of events led to the conclusion that a track existed in all these events which was not found by the computer program. The 1% inefficiency was consistent with a calculation based on the known single spark efficiencies (as low as 70% for some chambers) and the requirements of the track finding algorithm.

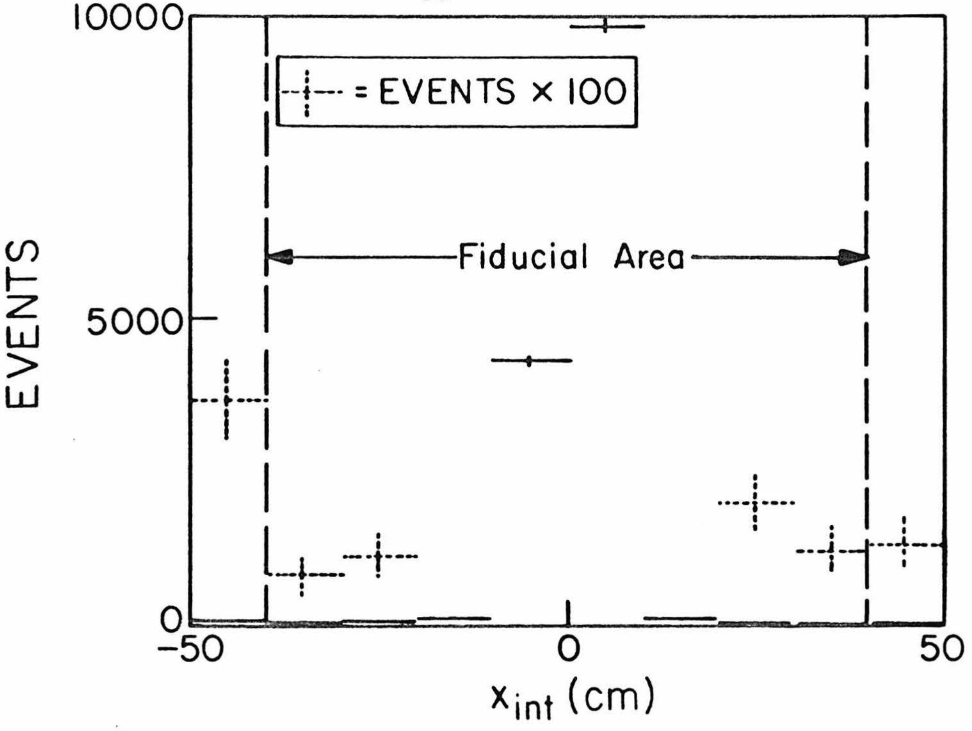

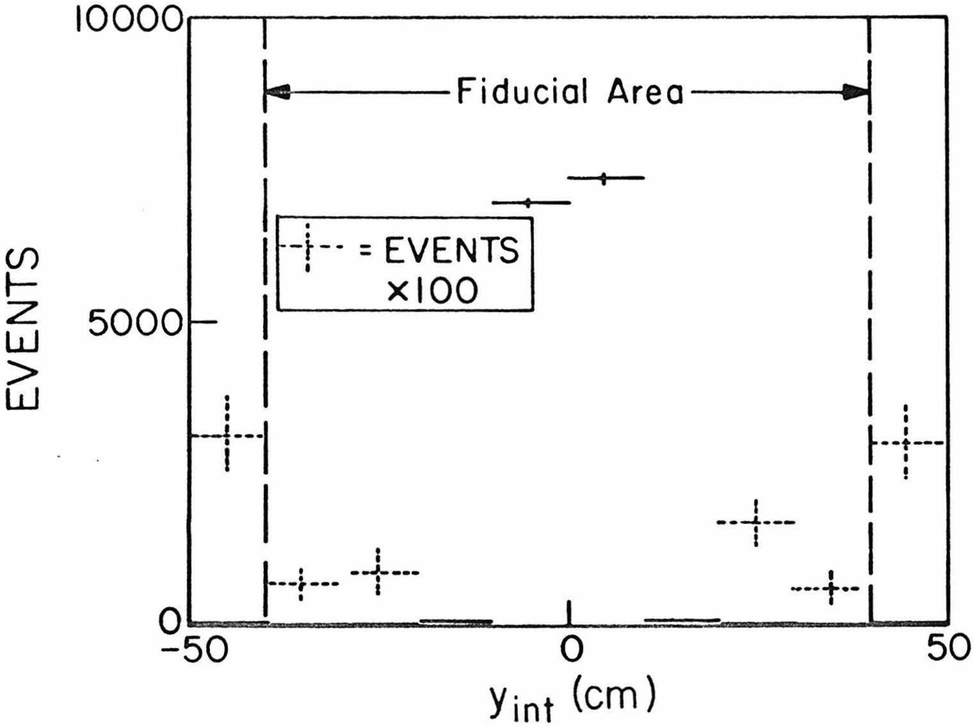

Figure 5-1: Distributions in x and y position transverse to the beam, obtained by extrapolating the muon track upstream to the beginning of the shower. Good tracks were required to have $|x_{int}| < 40$ cm and $|y_{int}| < 40$ cm. This cut eliminated 0.5% of the tracks.

This inefficiency resulted in a migration of 2 track events into the 1 track bin and of 1 track events into the 0 track bin. The inefficiency could be corrected using the muon identifier hodoscope counters.

To review the layout of these counters, there were four 28 cm x 112 cm counters after each of the 10 steel plates. The segmentation was in the x direction. The signals from the 4 counters were summed in the analysis program to provide the energy from each plane, in units of equivalent minimum ionizing particles. One algorithm for determining the number of muons would use the total pulse height from the 10 planes. The histogram of this pulse height showed two peaks for 1μ and 2μ events, well separated. However, there was a mechanism for moving 1μ events into the 2μ peak. Frequently, low energy hadrons exiting the downstream end of the calorimeter could interact in the first plates of the muon identifier, depositing enough energy to cause a 1μ event to move into the 2μ peak. A better algorithm was devised which used a step function to fit the number of muons in the event. The pulse height plotted versus plane number for a 1μ event should fit a flat line at 1 x minimum ionizing; the presence of a second muon would raise the level to 2 x minimum ionizing. The muon identifier profile of each event was fit to a step function with two levels, at 1 and 2 x minimum ionizing, and one parameter, which was the range of the higher level in number of planes. An ideal 1μ event would have a 2μ range of 0; a 2μ event would have a 2μ range of 10. Hadron punchthrough events would have a 2μ range of about 1-4. Figure 5-2 shows examples of the topologies.

The definition of 1μ and 2μ categories used both the spark chamber

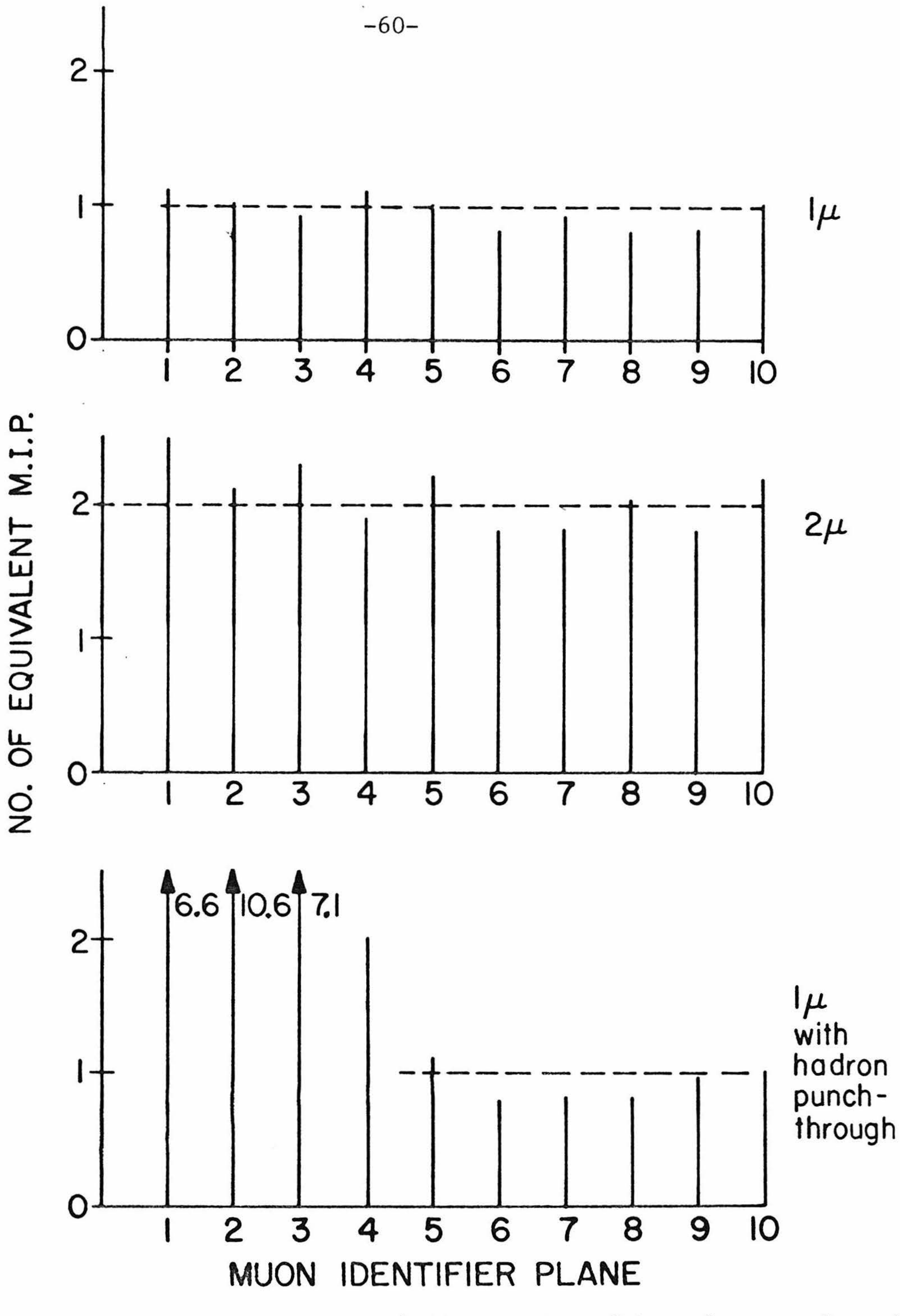

Figure 5-2: For three events, an illustration of how the step function fit counts the number of muons in the event. The pulse height in each muon identifier plane (in units of equivalent minimum ionizing particles) is plotted versus plane number, and a fit to a flat straight line is performed (dotted lines). If the flat line fit indicates 2 muons over at least the first 8 counters, the event is put into the 2μ category.

tracks and the counter algorithm just described. First, the events were divided into 1 track and 2 track categories using the chambers. Examination of the results of the counter algorithm for the 2 track events indicated that 90% of these events had a 2μ range of ≥ 8. The 1 track events exhibited a peak at low 2μ range, from real 1μ events, and a smaller peak at large range from the 2μ events with a missing track. Two new categories called 1μ and 2μ were defined accordingly. The 2μ category contained 2 track events, plus 1 track events with a 2μ range of ≥ 8 and more than 20 sparks in the upstream chambers not assigned to a track. The 1μ category contained the remaining 1 track events. The events shifted from the 1 track to the 2μ category were ~ 3% of the 1 track events. A correction had to be applied, on a percentage basis, for the events in which the second track was missed and the counter algorithm mistakenly gave a 2μ range of < 8. The counter algorithm made mistakes on 10% of the 2 track events, so the 1 track → 2μ transfer events were increased by 10%. Finally, the 1μ category had also to be increased by a percentage factor, determined from the number of 0 track events to be ~ 1%, for the loss of 1μ events into the 0 track category. The percentage corrections were found to be depend slightly on time, so they were calculated separately for each density. They did not depend on p or p_t of the observed track, however. The size of the various inefficiencies and the effect of the corrective algorithms were verified by scanning computer-generated pictures of an event sample from each density.

The next step was to classify each of the tracks in an event as triggering or non-triggering, according to whether the extrapolated track passed through the trigger counter T4 or not (see Figure 3-1). The events were then divided into four categories called $1\mu^+$, $2\mu^+$, $1\mu^-$, and $2\mu^-$, defined as follows:

(1) $1\mu^+$ contained a triggering positive track and no other tracks;

(2) $2\mu^+$ contained a triggering positive track and one other track, either unmeasured or negative;

(3) $1\mu^-$ contained a triggering negative track and no other tracks;

(4) $2\mu^-$ contained a triggering negative track and one other track, either unmeasured or positive.

(Each category was defined on an event-by-event basis and the percentage corrections described above were applied, where appropriate, within each category.)

Note that an event would appear in both the $2\mu^+$ and $2\mu^-$ categories if it contained a negative and a positive track, both of which entered T4. The 2μ categories were defined in this way so that the trigger efficiency of the $2\mu^+$ sample depended only on the positive trajectory and the trigger efficiency of the $2\mu^-$ sample depended only on the negative trajectory. Therefore, the ratio of the $1\mu^\pm$ rate to the $2\mu^\pm$ rate as a function of p or p_t of the triggering $\mu^\pm$ is approximately independent of the trigger efficiency and can be directly compared with the results of other experiments (see Section 7.2).

Some events from the 1 track and 2 track categories were not included in the 1μ and 2μ categories. Events with two muons of the same sign were discarded. Also, events in which no track passed through the fiducial area of T4 were eliminated. These events came either from muons passing through the light pipe of T4 or from noise firing T4 in conjunction with a muon firing the other trigger counters (~ 5% of the events).

The 2μ category would be constant with density if it included only 2μ's from electromagnetic sources. Therefore, the 2μ events which came from two unassociated muons (e.g., double π decay) should be subtracted. Same sign events, clearly from different decays, were already explicitly eliminated. An estimate of the remaining number of unassociated muons was made by multiplying the rate of 1μ category times the rate of interacting proton events from the IBV trigger observed to have an unmeasured or opposite sign track passing all the cuts. This statistical subtraction was made in each bin of p and p_t of the triggering muon.

Using the effective number of protons from Table 5-2, and the numbers of events in the four categories after the corrections listed above, rates for $1\mu^+$, $1\mu^-$, $2\mu^+$, and $2\mu^-$ were calculated for each of the three densities, as a function of p and p_t of the triggering muon.

5.5 Prompt and Non-prompt Rates and Distributions

First, the total rates for 1μ and 2μ events were plotted as a function of inverse density in Figure 5-3. The 2μ rate, as expected, was approximately constant with density. The 1μ rate was linear with a slope corresponding to the non-prompt rate at the most compact density and an intercept corresponding to the prompt rate. The numbers for these rates are listed in Table 5-3.

The prompt and non-prompt distributions in p and p_t were obtained by a similar density extrapolation in each bin of p or p_t. Representative extrapolations in p_{μ^-} are shown in Figure 5-4. The changing relationship

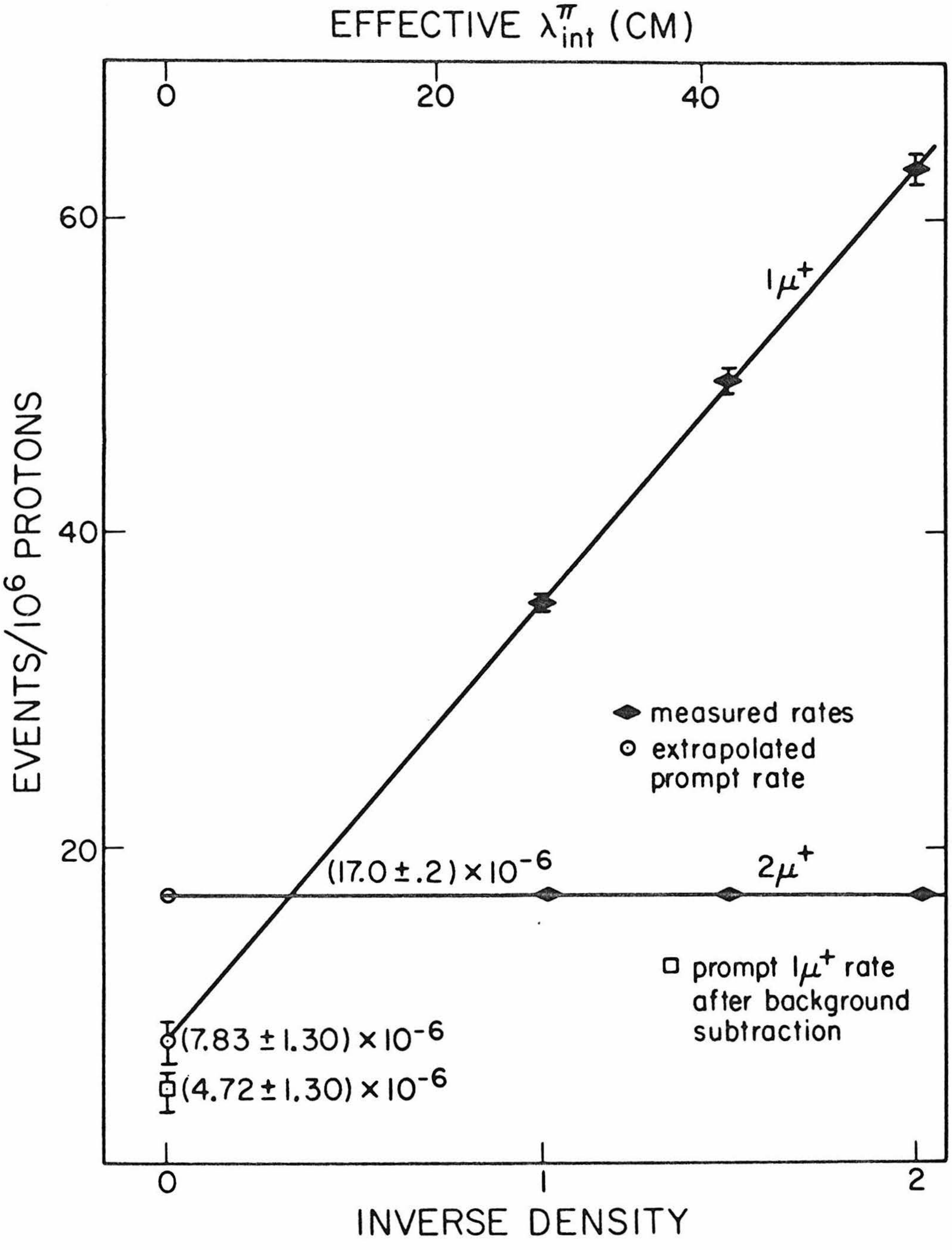

Figure 5-3: (a) The measured $1\mu^+$ and $2\mu^+$ rates from the high p trigger versus effective inverse density. The lines are least squares fits to the measured rates; the values of the intercepts at $1/\rho = 0$ are shown. The intercept of the $1\mu^+$ line measures the apparent prompt $1\mu^+$ rate. The value of the prompt $1\mu^+$ rate after background subtraction is also shown. [Inverse density = 1 corresponds to $\rho = 5.9$ g/cm^3.]

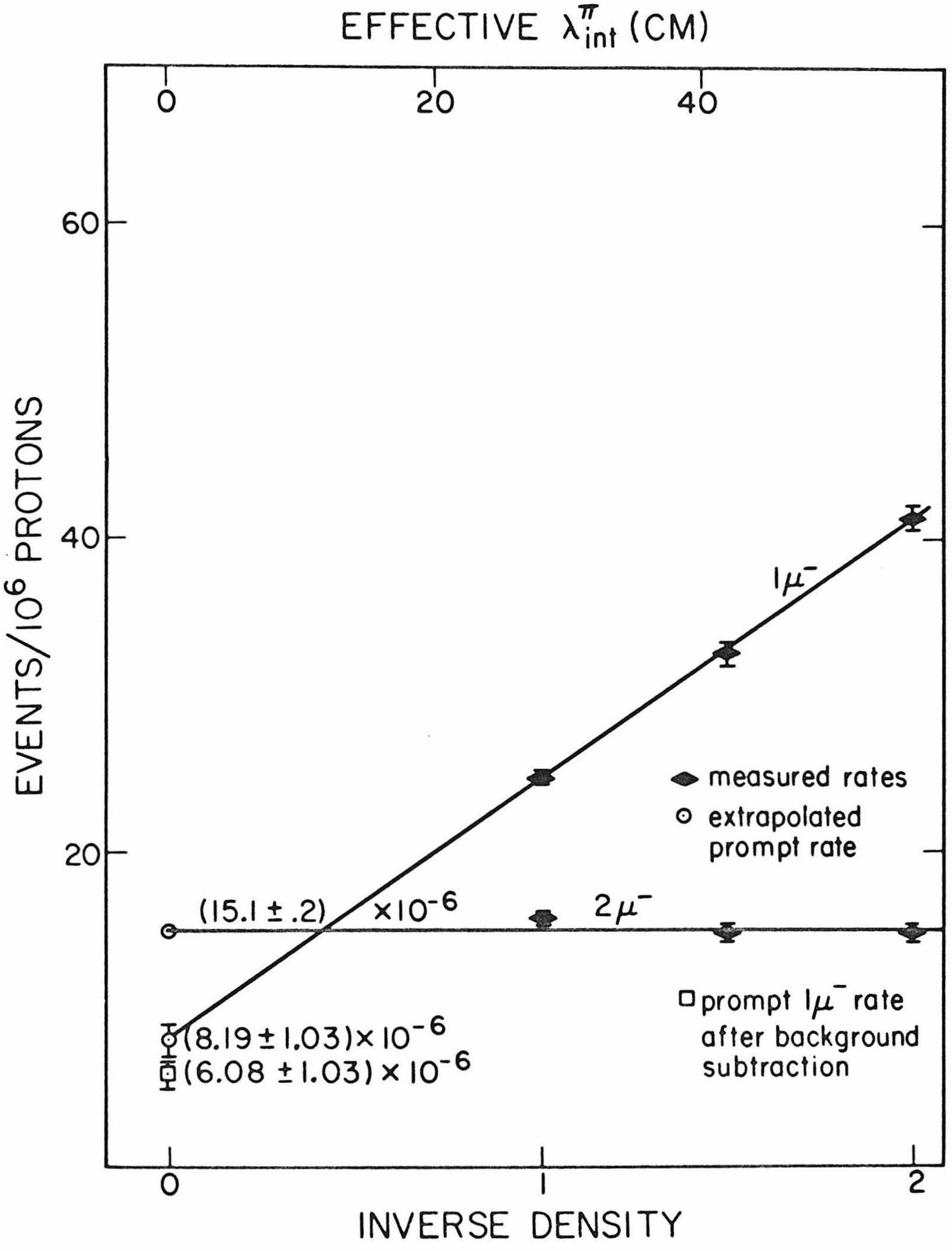

Figure 5-3: (b) The measured $1\mu^-$ and $2\mu^-$ rates from the high p trigger versus effective inverse density. The lines are least squares fits to the measured rates; the values of the intercepts at $1/\rho = 0$ are shown. The intercept of the $1\mu^-$ line measures the apparent prompt $1\mu^-$ rate. The value of the prompt $1\mu^-$ rate after background subtraction is also shown. [Inverse density = 1 corresponds to $\rho = 5.9$ g/cm^3.]

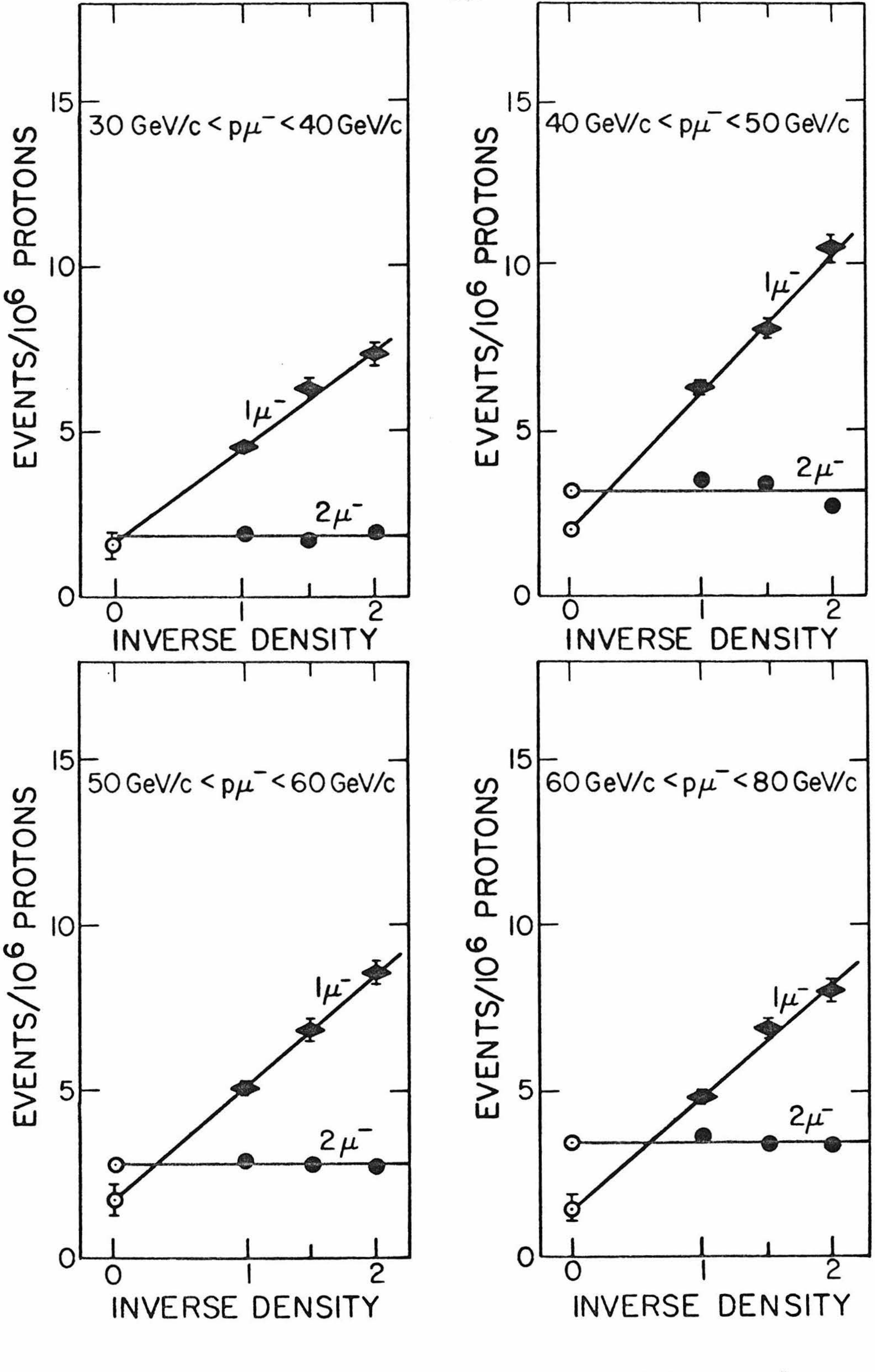

Figure 5-4: Density extrapolations of the $1\mu^-$ and $2\mu^-$ rates for various bins in p_{μ^-}.

of slope and intercept for the 1μ fit reflects the changing ratio of non-prompt to prompt rate as a function of p. The prompt 1μ distributions of p and p_t resulting from such extrapolations are Figures 5-5(a-d); the non-prompt 1μ distributions are Figures 5-6(a-d); the prompt 2μ distributions are Figures 5-7(a-d). The Monte Carlo curves drawn in Figures 5-6 and 5-7 will be discussed in the next section. The prompt 1μ distributions contain backgrounds which must be subtracted to obtain the real prompt 1μ signal.

5.6 Backgrounds in the Prompt 1μ Signal

Now we consider the backgrounds which may contribute to the prompt 1μ signal.

(1) Muons from beam halo or upstream interactions.

These muons were eliminated by the hardware requirements in the trigger of no signal from the halo counter plus the presence of a substantial amount of hadronic energy in the calorimeter. A small remaining contamination at very large transverse distance from the beam was eliminated by accepting only muon tracks which extrapolated to within ± 38 cm of the beam at the interaction point, as discussed above. Since all halo muons were explicitly rejected either by the hardware or by the software, no subtraction for this source from the observed prompt rate was needed.

(2) Muons from hyperon decays.

For the most part, hyperon decays are removed, like π and K decays, by the density extrapolation. But since $\gamma c\tau$ is of the order of 100 cm for hyperons compared to ~ 6000 cm for K's, the deviation from linearity

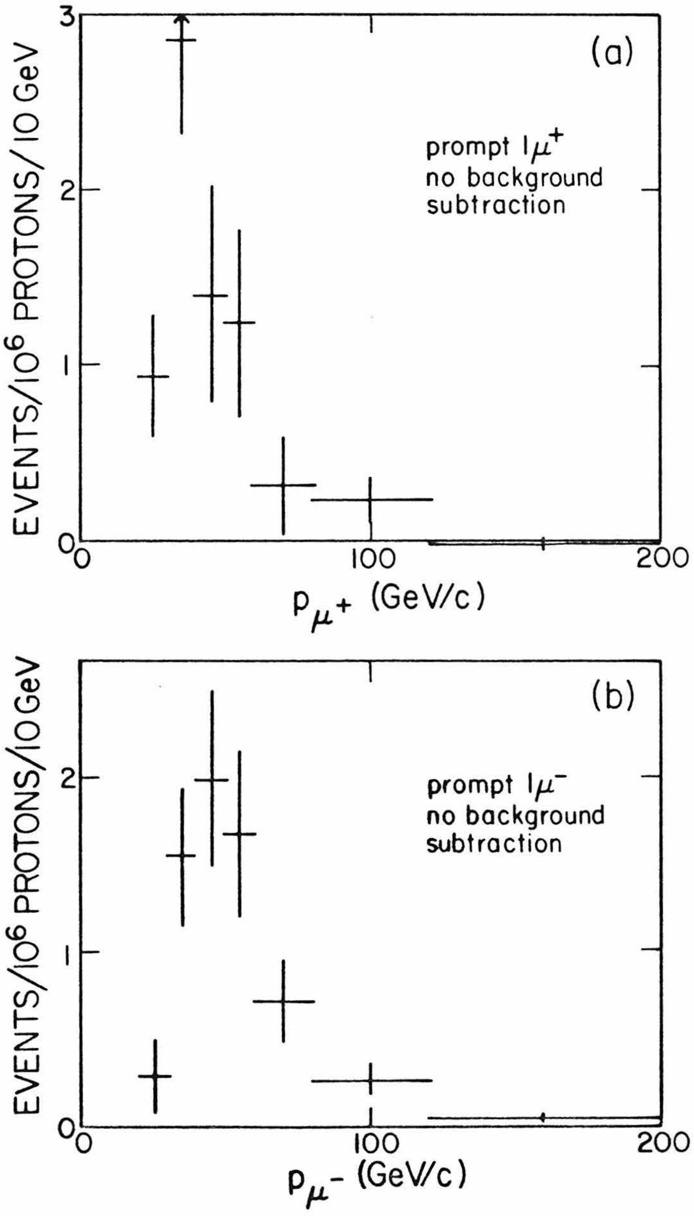

Figure 5-5:

(a) The distribution of the prompt 1μ^+ rate versus p_{μ^+}, before background subtractions.

(b) The distribution of the prompt 1μ^- rate versus p_{μ^-}, before background subtractions.

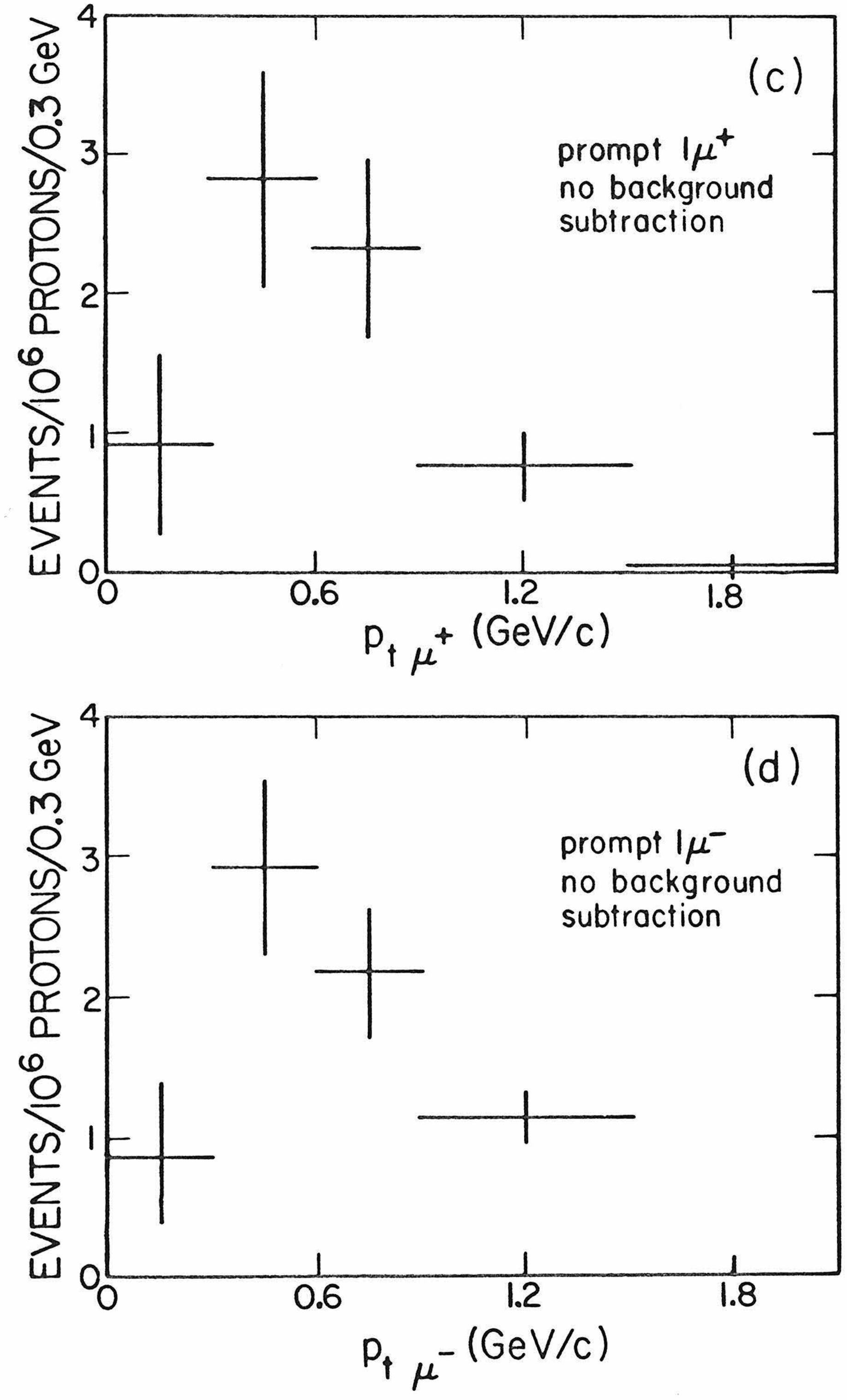

Figure 5-5:

(c) The distribution of prompt $1\mu^+$ events versus $p_{t\mu^+}$, before background subtractions.

(d) The distribution of prompt $1\mu^-$ events versus $p_{t\mu^-}$, before background subtractions.

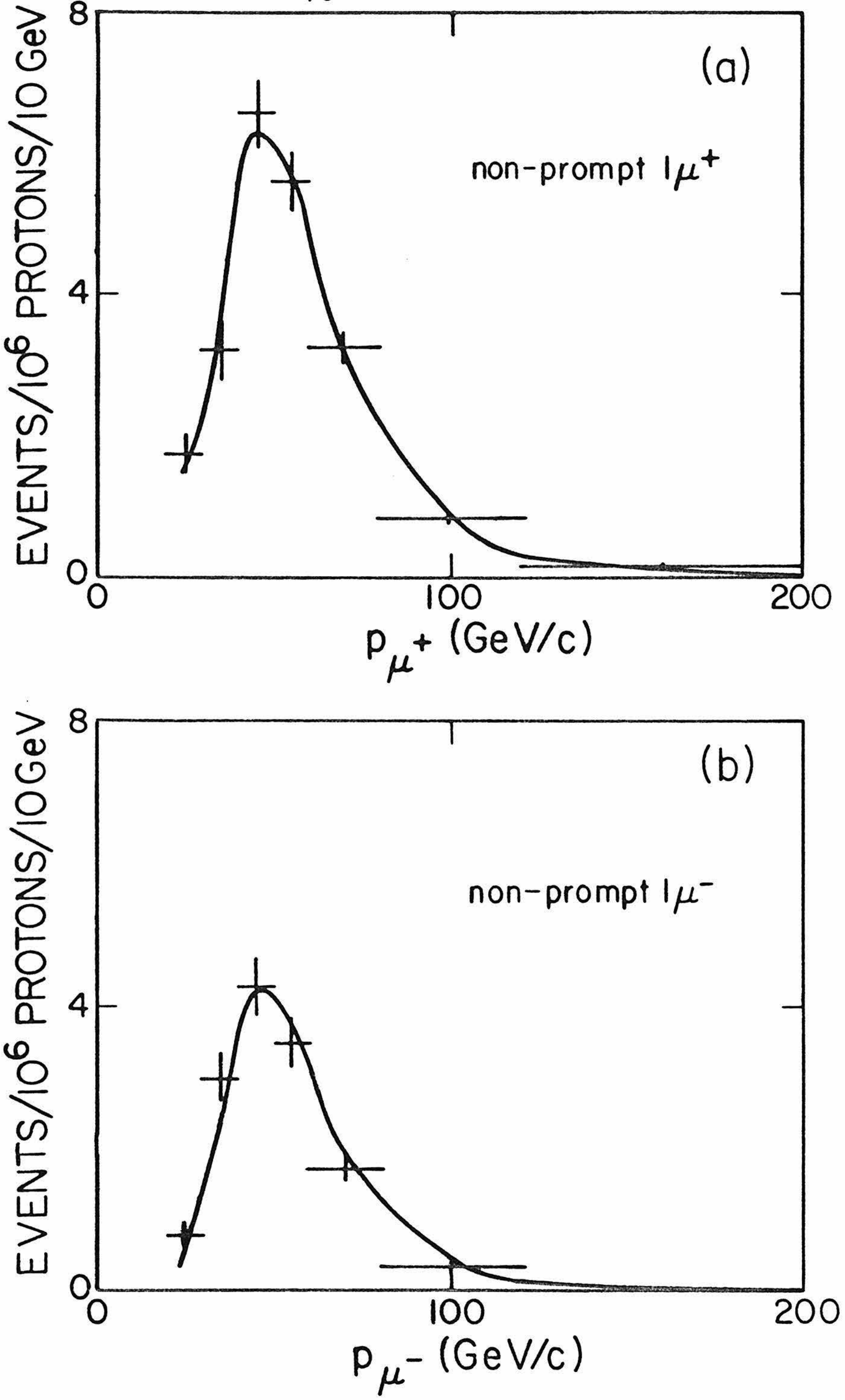

Figure 5-6:

(a) The distribution of non-prompt 1μ^+ events versus $p_{\mu+}$, compared to the Monte Carlo distribution (curve). The Monte Carlo was normalized to the total number of events.

(b) The distribution of non-prompt 1μ^- events versus $p_{\mu-}$, compared to the Monte Carlo distribution (curve). The Monte Carlo was normalized to the total number of events.

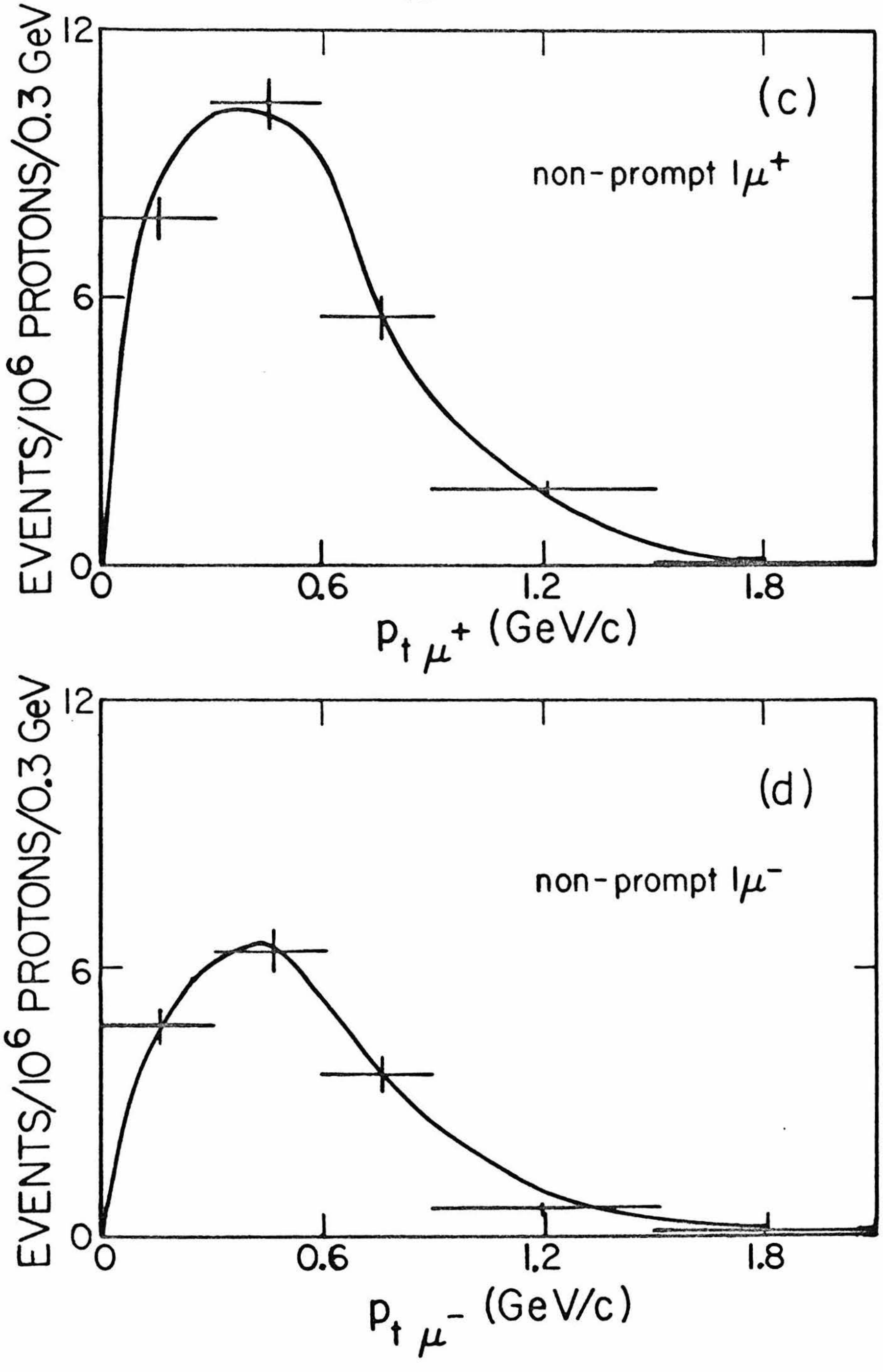

Figure 5-6:

(c) The distribution of non-prompt $1\mu^+$ events versus $p_{t\mu^+}$, compared to the Monte Carlo distribution (curve).

(d) The distribution of non-prompt $1\mu^-$ events versus $p_{t\mu^-}$, compared to the Monte Carlo distribution (curve).

The Monte Carlo distributions were normalized separately for μ^+ and μ^- to the total number of events.

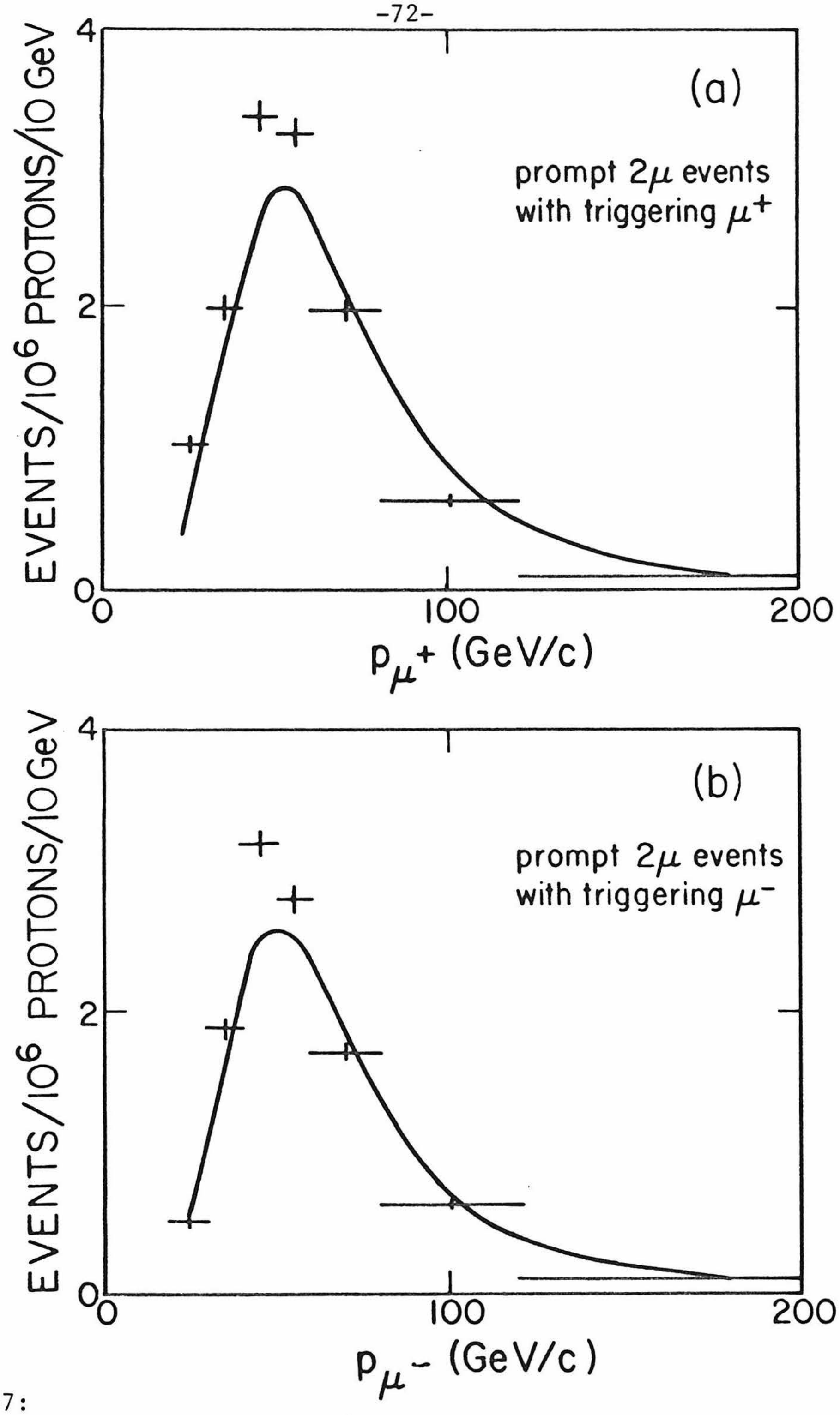

Figure 5-7:

(a) The distribution of $2\mu^+$ events versus p_{μ^+}, compared to the Monte Carlo prediction (curve).

(b) The distribution of $2\mu^-$ events versus p_{μ^-}, compared to the Monte Carlo prediction (curve).

The Monte Carlo distributions were normalized separately for $2\mu^+$ and $2\mu^-$ to the total number of events.

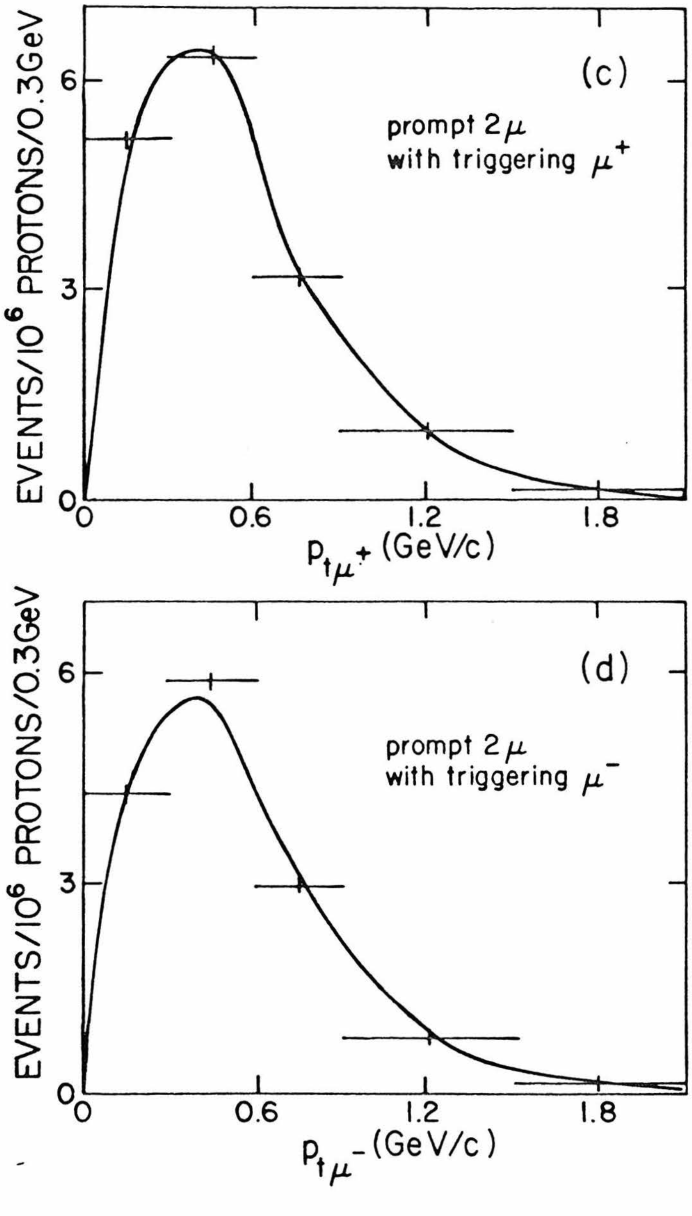

Figure 5-7:

(c) The distribution of $2\mu^+$ events versus $p_{t\mu+}$, compared to the Monte Carlo prediction (curve).

(d) The distribution of $2\mu^-$ events versus $p_{t\mu-}$, compared to the Monte Carlo prediction (curve).

The Monte Carlo distributions were normalized separately for $2\mu^+$ and $2\mu^-$ to the total number of events.

caused by λ_i/λ_d is larger. Calculation showed that the contribution to the $1\mu^+$ signal from Σ^+ decays is less than 0.08% of the signal. The decays Λ^o and Σ^- were calculated to contribute less than 0.09% of the $1\mu^-$ rate. (Cross sections and distributions for hyperon production were taken from Reference 19.) No subtraction was made in the distributions or in the total rate, because this background was not a significant contribution in any bin.

(3) Muons from downstream decays of pions and kaons. The density extrapolation separated out only those non-prompt decays occurring within the 1.2 m section of the target which was expanded. Decays downstream of the density change would of course be independent of the density and would look like a prompt 1μ signal. These decays were calculated using a Monte Carlo program which followed the hadron shower down to the third generation of pions, using distributions and production cross sections from Reference 20. It was permissible to cut off the shower at the third generation because the high energy requirement of the trigger meant that decays from subsequent generations had very little chance of triggering. The agreement of the Monte Carlo predictions with the observed non-prompt distributions was quite good, as illustrated in Figures 5-6(a-d). The Monte Carlo predicted a ratio of background from downstream decays to observed non-prompt muons for each bin in p or p_t. These ratios were multiplied by the observed non-prompt distribution to obtain the background distributions, which were subtracted from the prompt 1μ distributions. (See Table 5-4.) The total subtraction was 24% of the raw prompt $1\mu^+$ rate and 8% of the raw prompt $1\mu^-$ rate.

(4) Muons from $\mu^+\mu^-$ events with one muon unobserved.

The 2μ events sometimes had one muon unobserved either because of its wide angle or its low energy. Muons with $E_\mu < 4$ GeV ranged out in the target or muon identifier. The range limit was the predominant mechanism for misidentifying a 2μ event, because tracks were measured out to ~ 100 mrad in the laboratory frame, which corresponded to 90% of the solid angle in the center-of-mass frame. Again, a Monte Carlo program calculated the sources of $\mu^+\mu^-$ production from the hadron shower, including ρ, ω, ϕ, and ψ decay and the Drell-Yan continuum. The distributions and cross sections used in the Monte Carlo were obtained by scaling the data of Pilcher et al.[21] to $\sqrt{s} = 28$ GeV and an iron target. A calculation of Bethe-Heitler pair production of muons from photons in the shower was also included, using Tsai's parameterization[22] of Bethe-Heitler production and a π^o production distribution equal to the average of π^+ and π^- distributions from Reference 21. All sources of muons were followed down to the third generation. Just as for the downstream decay background, the subtraction was made by taking the calculated ratio of misidentified 2μ's over identified 2μ's and multiplying by the observed 2μ distribution. This procedure was important for the misidentified 2μ's because the calculated 2μ p distribution was not a very good fit to the observed distribution. (See Figures 5-7(a-d).) The total subtraction for this background was 42% of the raw $1\mu^+$ rate and 28% of the raw $1\mu^-$ rate.

5.7 Error Analysis

The errors quoted on the extrapolated rates in Table 5-3 and shown in Figures 5-5 through 5-7 are the errors from the least squares fit to the rates at each density. The errors on the three rates used in the fit were statistical only. Possible systematic effects in the extrapolation were:

(1) deviations from the linearity of the non-prompt muon rate. As discussed in the Appendix, these effects are calculable and negligible.

(2) variation of the trigger efficiency with time, resulting in a spurious variation of rate with density. Such variations were monitored and corrected for, as discussed in Section 4.8; any remaining systematic effect would be much smaller than the statistical errors.

The major systematic errors in the determination of the prompt 1μ rate came from the uncertainty in the two significant background subtractions.

5.7.1 Downstream Decays

The calculation of background from π and K decays downstream of plate 25 is quite straightforward, if one knows the distribution in p and p_t of the hadrons and especially the distribution in number of hadrons versus z position in the calorimeter. Figure 5-6 illustrates the good agreement of the π-K Monte Carlo with the p and p_t distribution of the observed π and K decays. Studies with the Monte Carlo showed that the size of the calculated background was quite insensitive to the π/K ratio (a 5% change in the background for a 50% change in the ratio). A greater sensitivity to the relative contribution of the different generations in the 400 GeV shower was observed. The third generation of π and K production contributed less than 5% of the observed decays, but 20% of the background. Therefore, increasing the size of the third generation relative to the first by a factor of 3 would be unobservable in the p and p_t distributions of Figure 5-6, but would cause a 30% increase in the calculated background. However, there are arguments to limit the possible error in the size of the third generation. The estimated uncertainty in the mean multiplicity distribution of hadron production was 10%. Compounding this error through three generations would give only a 4% uncertainty in the size of the background.

A possible empirical check on the amount of downstream decay background was offered by the distribution in the plate number in which the 400 GeV interaction occurred. Charm decays and 2μ production would be expected to have the same distribution in plate number as the unbiased proton interactions from the IBV trigger. However, the π and K decay rate had a different dependence on interaction position. The downstream decay rate was enhanced for downstream interactions while upstream decays were slightly suppressed. A fit was made to the distribution of the $1\mu^+$ rate at the compacted density, normalized to the distribution of IBV triggers at that density, using a flat component and a component with the distribution obtained from the Monte Carlo for downstream decays (Figure 5-11). The fit did not provide a strict constaint on the background. The Monte Carlo calculation gave the result that 3.2% of the compacted $1\mu^+$ rate came from the downstream decays. The fit gave a value of (11.7 ± 7.7)% of the compacted rate as the coefficient of the downstream decay component.

Because the empirical checks failed to constrain the background, a systematic error of 30% was assigned to the downstream decay subtraction, although no mechanism was apparent for changing the generation ratios to give such an error. In the subtraction of the downstream decays from the p and p_t distributions, only the statistical errors were used. Increasing the third generation by a factor of 3 would not have changed the shape of the background/signal ratio by an amount significant compared with the statistical determination of the ratio in each bin. Note that the 30% systematic error corresponded to a 7% error in the prompt $1\mu^+$ signal and a 2% error in the prompt $1\mu^-$ signal. (See Table 5-4.)

5.7.2 Misidentified 2μ's

The background from misidentified 2μ's had a different source of systematic error. The first two generations contributed 94% of the misidentified 2μ's and 96% of the identified 2μ's, and the background/signal ratio was not sensitive to the relative contribution of the three generations. The ratio was sensitive to the amount of Bethe-Heitler muon production, however, because the Bethe-Heitler pairs contained a larger precentage of unobserved muons than pairs from resonance decay or the continuum. The larger background resulted from the greater asymmetry in E_μ for the Bethe-Heitler pairs. The relative normalization of Bethe-Heitler pair production to other pair production could not be empirically fixed because the observed 2μ p distribution was not well fit by a combination of the Bethe-Heitler distribution and the resonance-continuum distribution. Varying the normalization over the range allowed by the p distribution of the data resulted in a 10% variation in the predicted background. The size of the variation for each bin in p and p_t

of the triggering muon was assigned as the systematic error, but these errors were never as much as 20% of the statistical error in the raw prompt 1μ rate in each bin.

5.8 Summary

To summarize, the analysis yielded a corrected prompt $1\mu^+$ signal of $(4.7 \pm 1.3 \pm 0.4) \cdot 10^{-6}$ events/interacting proton and a corrected prompt $1\mu^-$ signal of $(6.1 \pm 1.0 \pm 0.2) \cdot 10^{-6}$ events/interacting proton. The first error listed is the statistical error and the second is the systematic error. The background subtractions are listed in Table 5-5, and shown in Figure 5-8. The corrected prompt 1μ p distributions are shown in Figure 5-9, and the p_t distributions in Figure 5-10. The errors in the total signal and in the distributions are dominated by the statistical errors from the density extrapolation rather than by the systematic errors in the background subtraction.

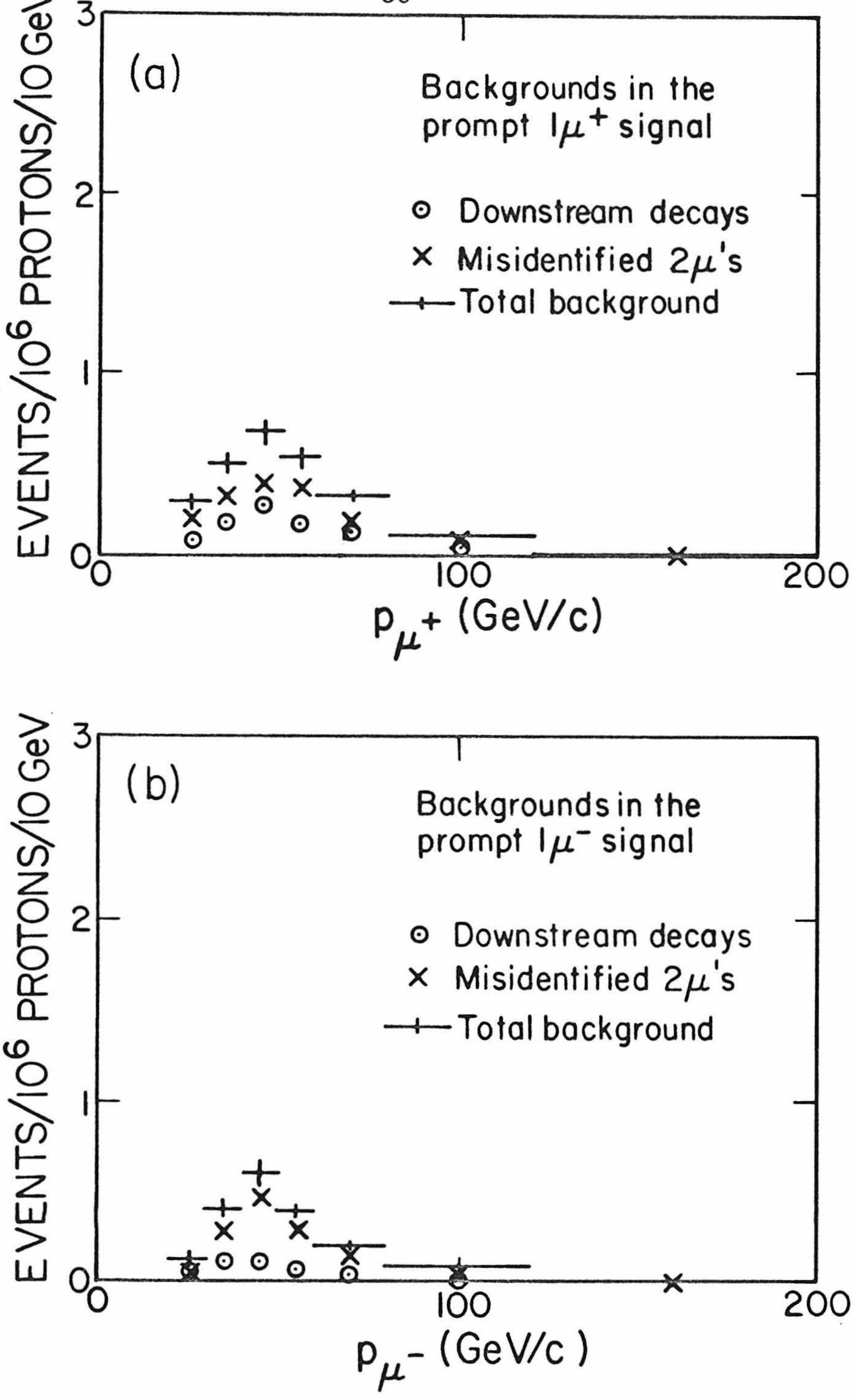

Figure 5-8:

(a) The calculated backgrounds in the prompt $1\mu^+$ signal versus p_{μ^+}.

(b) The calculated backgrounds in the prompt $1\mu^-$ signal versus p_{μ^-}.

Total background is the sum of downstream decays and misidentified 2μ's; the error shown on total background is the sum in quadrature of the errors (not shown) on downstream decays and misidentified 2μ's.

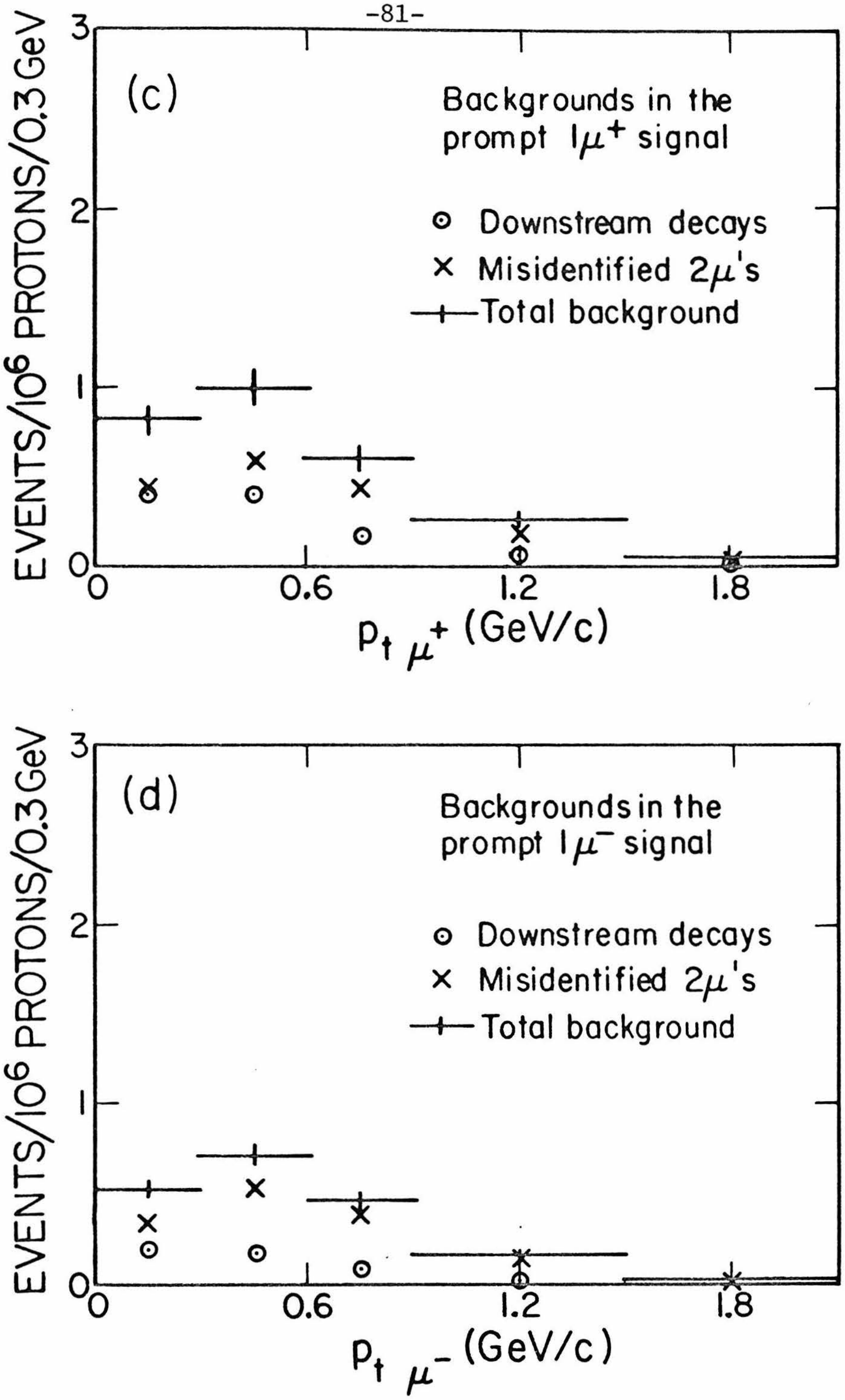

Figure 5-8:

(c) The calculated backgrounds in the prompt $1\mu^+$ signal versus $p_{t\mu^+}$.

(d) The calculated backgrounds in the prompt $1\mu^-$ signal versus $p_{t\mu^-}$.

Total background is the sum of downstream decays and misidentified 2μ's.

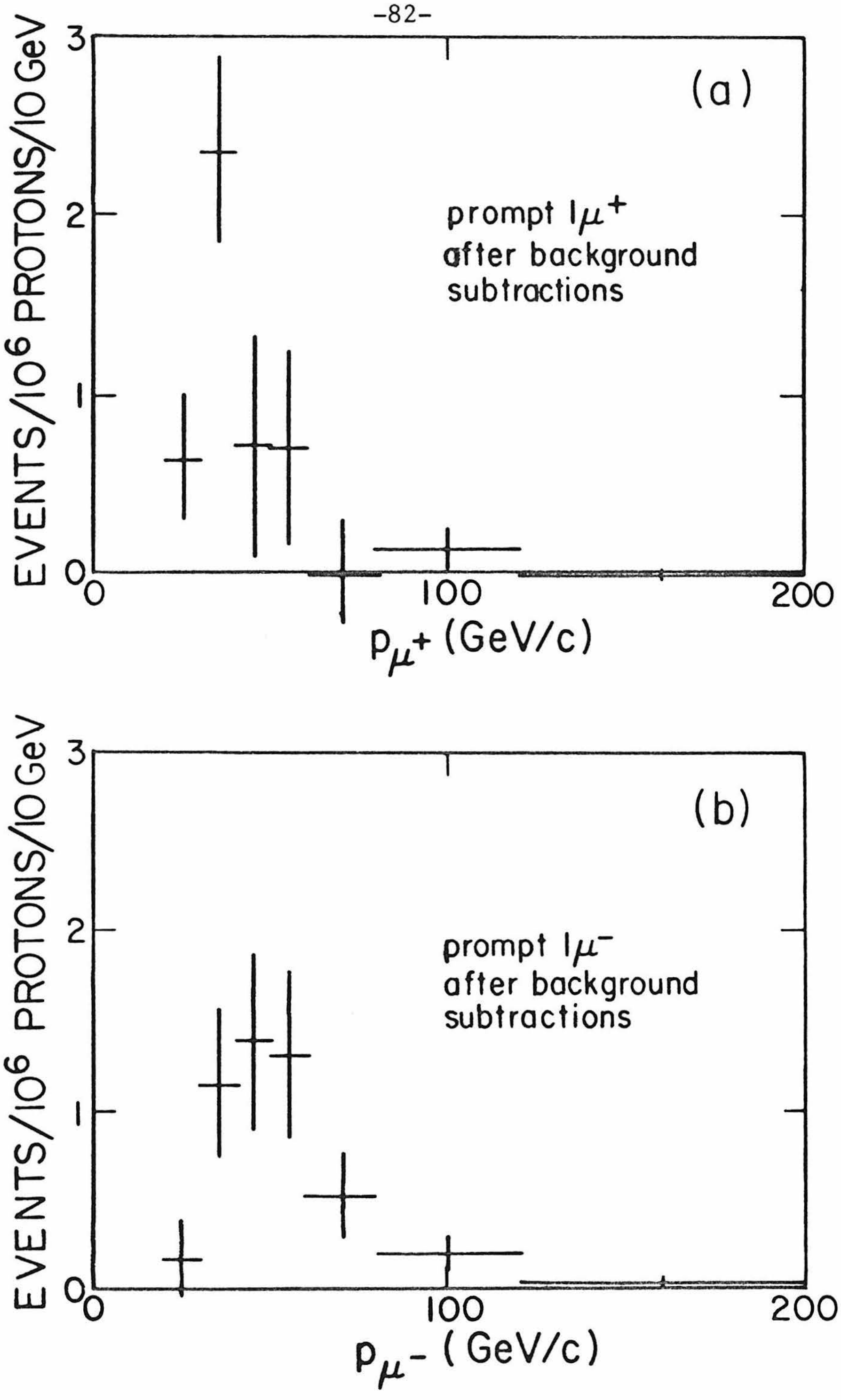

Figure 5-9:

(a) The prompt 1μ^+ distribution in p_{μ^+} after subtraction of backgrounds shown in Figure 5-8.

(b) The prompt 1μ^- distribution in p_{μ^-} after subtraction of backgrounds shown in Figure 5-8.

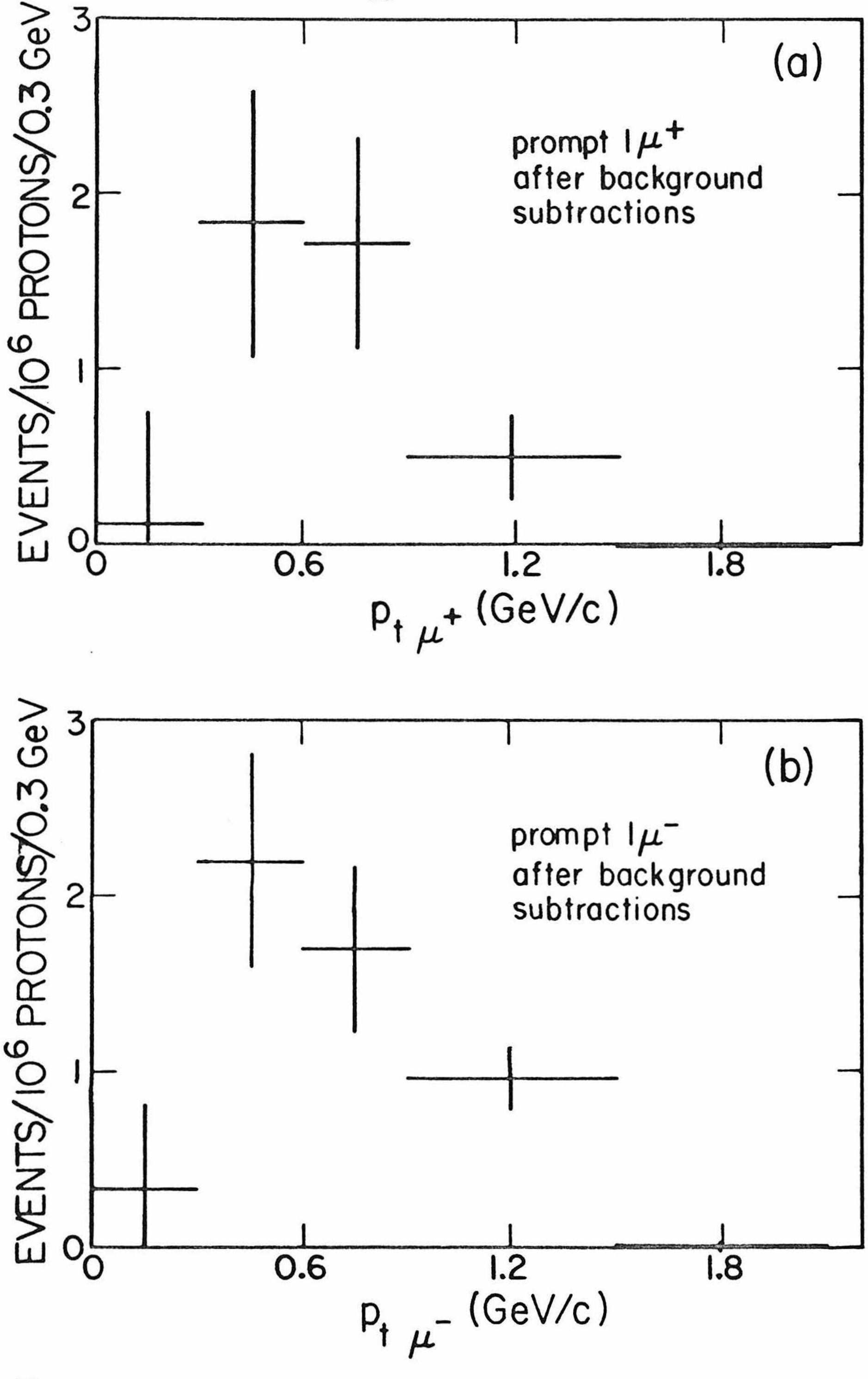

Figure 5-10:

(a) The prompt $1\mu^+$ distribution in $p_{t\mu^+}$ after subtraction of backgrounds shown in Figure 5-8.

(b) The prompt $1\mu^-$ distribution in $p_{t\mu^-}$ after subtraction of backgrounds shown in Figure 5-8.

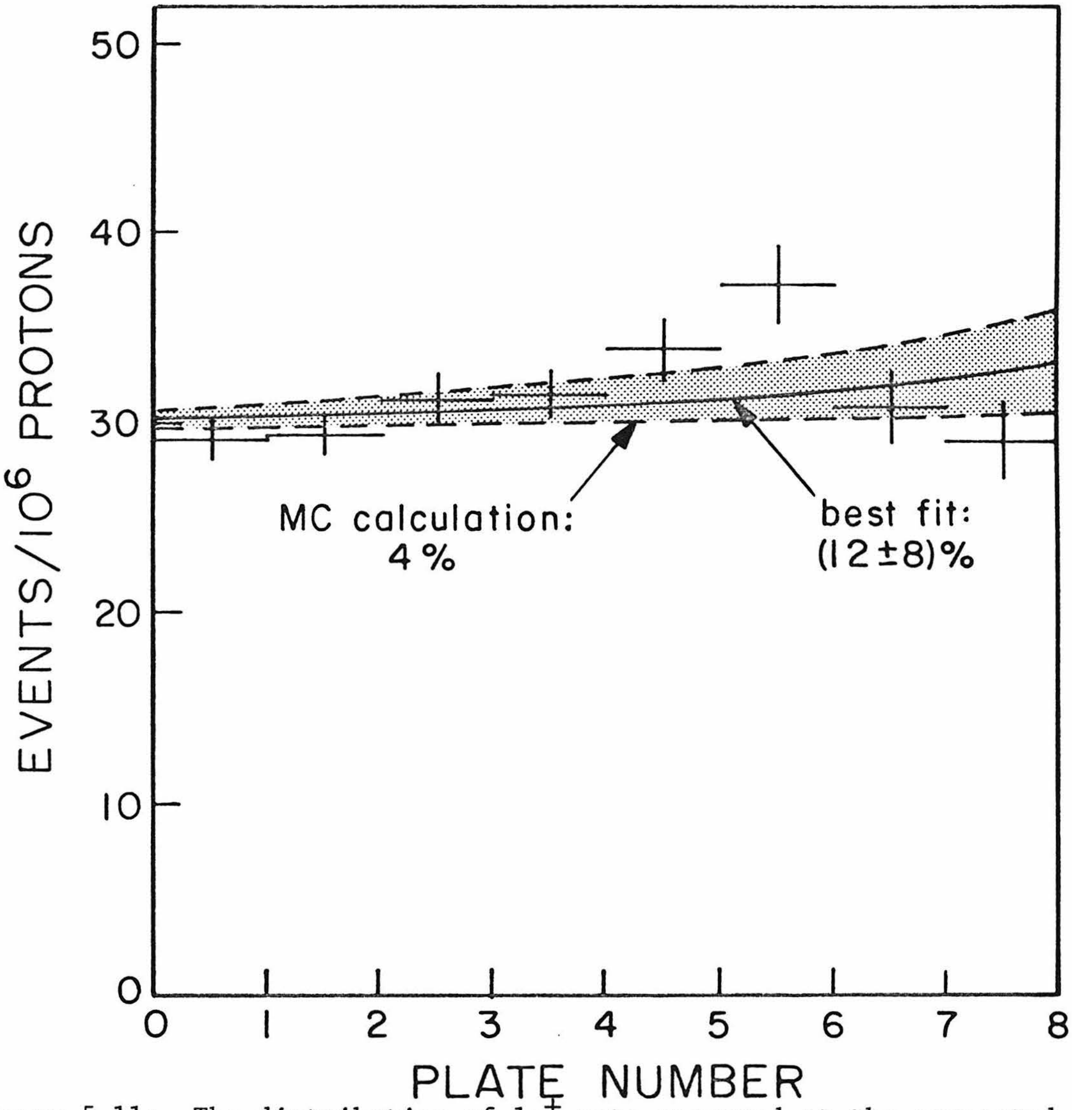

Figure 5-11: The distribution of $1\mu^+$ rate measured at the compacted density versus the plate number in which the 400 GeV interaction took place. (One plate = 3.8 cm of steel.) The solid line shows the best fit to a combination of a flat component (expected shape if there were no downstream decays) and a downstream decay component whose shape was calculated with the Monte Carlo. The shaded area shows the one-standard-deviation limits from the fit, which gave (12±8)% for the size of the downstream decay component. That size had been calculated from the Monte Carlo to be 3.5%, corresponding to the lower dashed line. Three percent of the compacted rate equals 14% of the raw prompt $1\mu^+$ rate.

Table 5-3: Total Rates at Each Density

Rate: events/10^6 protons Density	$1\mu^+$	$2\mu^+$	$1\mu^-$	$2\mu^-$
Compacted	35.54 ± .46	17.30 ± .28	24.75 ± .37	15.80 ± .27
Semi-expanded	49.56 ± .82	16.76 ± .42	32.72 ± .64	14.70 ± .40
Expanded	63.20 ± .97	16.94 ± .42	41.39 ± .73	14.87 ± .39
Intercept	7.83 ±1.31	16.99 ± .23	8.19 ±1.03	15.12 ± .20
Slope	27.73 ±1.01	-	16.52 ± .78	-

Table 5-4: Backgrounds in the Prompt 1μ Signal*

Raw prompt $1\mu^+$	Downstream decays in $1\mu^+$	Misidentified 2μ's in $1\mu^+$	Corrected prompt $1\mu^+$
7.83 ± 1.31	1.13 ± .11 ± .34	1.99 ± .09 ± .23	4.71 ± 1.32 ± .41

Raw prompt $1\mu^-$	Downstream decays in $1\mu^-$	Misidentified 2μ's in $1\mu^-$	Corrected prompt $1\mu^-$
8.19 ± 1.03	0.40 ± .07 ± .12	1.71 ± .08 ± .23	6.08 ± 1.04 ± .26

*All rates quoted are events/10^6 protons; the second error listed is the systematic error.

Table 5-5: Prompt 1μ Distributions and Background Subtractions

p_{μ^+}(GeV/c)	Raw Prompt 1μ	Downstream Decays	Misidentified 2μ's	Corrected Prompt 1μ
20-30	0.931(0.341)	0.079(0.026)	0.211(0.035)	0.641(0.342)
30-40	2.847(0.508)	0.175(0.048)	0.316(0.039)	2.364(0.511)
40-50	1.391(0.603)	0.281(0.051)	0.400(0.051)	0.710(0.601)
50-60	1.241(0.540)	0.174(0.039)	0.370(0.036)	0.700(0.541)
60-80	0.614(0.554)	0.260(0.061)	0.378(0.032)	-0.024(0.554)
80-120	0.922(0.420)	0.145(0.035)	0.249(0.025)	0.528(0.422)
120-200	-0.116(0.189)	0.020(0.010)	0.064(0.010)	-0.200(0.190)
$p_{t\mu^+}$(GeV/c)				
0-0.3	0.928(0.622)	0.390(0.059)	0.427(0.035)	0.111(0.624)
0.3-0.6	2.827(0.757)	0.409(0.075)	0.577(0.044)	1.843(0.761)
0.6-0.9	2.316(0.592)	0.171(0.043)	0.425(0.038)	1.725(0.591)
0.9-1.5	1.513(0.449)	0.139(0.039)	0.379(0.038)	0.991(0.452)
1.5-2.1	0.090(0.174)	0.029(0.013)	0.078(0.018)	-0.017(0.171)
p_{μ^-}(GeV/c)				
20-30	0.284(0.200)	0.057(0.038)	0.068(0.013)	0.159(0.204)
30-40	1.536(0.404)	0.116(0.030)	0.276(0.031)	1.144(0.401)
40-50	1.970(0.489)	0.115(0.028)	0.484(0.047)	1.376(0.492)
50-60	1.669(0.451)	0.079(0.022)	0.295(0.031)	1.295(0.451)
60-80	1.422(0.443)	0.090(0.023)	0.29 (0.027)	1.037(0.441)
80-120	1.054(0.323)	0.034(0.012)	0.236(0.023)	0.784(0.321)
120-200	0.350(0.130)	0.004(0.004)	0.058(0.009)	0.288(0.130)
$p_{t\mu^-}$(GeV/c)				
0-0.3	0.855(0.484)	0.189(0.037)	0.345(0.029)	0.321(0.482)
0.3-0.6	2.914(0.609)	0.173(0.040)	0.539(0.041)	2.201(0.611)
0.6-0.9	2.168(0.470)	0.086(0.023)	0.375(0.032)	1.705(0.471)
0.9-1.5	2.241(0.351)	0.023(0.009)	0.281(0.043)	1.939(0.353)
1.5-2.1	0.094(0.134)	0.011(0.008)	0.050(0.012)	0.033(0.131)

CHAPTER 6

HIGH PT DATA ANALYSIS

6.1 Introduction

The analysis of the high p_t data was very similar in outline to the analysis of the high p data. The major differences lay in the relative importance of various backgrounds and in the fact that the p_t trigger accepted only positive muons instead of muons of both signs. There was little overlap in the acceptance of the two triggers in any region with a significant number of events. The high p_t data were useful as a measure of prompt single muon production in a different kinematic region ($.5 < p_t < 2.5$ GeV/c and $10 < p < 60$ GeV/c) from that covered by the high p data.

6.2 Trigger Efficiency

As mentioned in Section 4.8, the S2 hodoscope, which was included in the p_t trigger, was inefficient during some runs. These runs, which were scattered throughout the running period, contained about 4% of the total data and were omitted from the analysis.

6.3 Normalization Corrections and Cuts

The selection criteria applied to the proton interaction parameters included ones similar to those used in the high p analysis (see Section 5.3): (1) no more than 1 PWC track incident, (2) less than 0.5 x minimum ionizing pulse height in the halo counter, and (3) an interaction beginning in plates 1-8 of the calorimeter. In addition, the shift register counting beam particles (see Section 4.3) was required to show no particle except the triggering particle within the ADC gate (100 ns long), and the total instantaneous rate measured over the period 300 microseconds before the event was required to be less than 8 x 10^6 particles per second. These extra cuts were directed primarily toward assuring a good hadron energy measurement - a measurement not confused by additional incident particles or large rate-induced gain shifts in the phototubes. Note that the average incident intensity was an order of magnitude higher during the high p_t run than during the high p run.

Just as in the high p analysis, the effect of the beam selection criteria was measured by applying the same cuts to the sample of interacting proton events, required to have no muon track, from the IBV trigger. The correction to the normalization was about 20%; the normalizations and corrections for the different density samples are given in Table 6-1.

6.4 Definition of 1μ and 2μ categories

Good tracks were selected with the same procedure given in Section 5.4. Tracks were required to extrapolate to an origin within the transverse area of the calorimeter and to be associated with appropriate tagging bit signals and pulse heights from the counters they passed through.

The track-finding efficiency was better in the high p_t data analysis because of slightly better chamber efficiencies and looser requirements in the track finding program. The efficiency was found to be .995 ± .001 throughout the running, so no significant feeding of 2μ events into the 1μ category or of 1μ events into the 0 track category occurred.

The good μ^+ sample included the spurious triggers described in Section 3.3. It was defined as the set of events passing all the beam cuts and containing:

(1) 1 μ^+ trajectory, which had passed through a set of counters whose signals would satisfy the p_t trigger, which did not cross the toroid axis upstream of the middle of the third toroid, and whose radius from the beam line measured at the upstream face of the toroids was > 17.5 cm.

(2) at most one other good track downstream of the muon identifier, which could either be unmeasured or measured to be negative.

This sample was divided into the $1\mu^+$ category, with only the positive track, and the $2\mu^+$ category, with the positive track and one other track. Note that the efficiency for each sample depended only on the positive trajectory, so that ratios of $1\mu^+$ rates to $2\mu^+$ rates were approximately independent of trigger efficiency. The $2\mu^+$ sample contained some events from non-electromagnetic sources such as double pion decay. An estimate of this rate was made by multiplying the observed $1\mu^+$ rate times the rate of IBV events with an unmeasured or negative track. The estimate was subtracted from the $2\mu^+$ rate in each bin of p and p_t of the positive muon. The total number of events in the two categories at each density and the size of the non-electromagnetic subtraction are shown in Table 6-2.

6.5 Prompt and Non-prompt Rate Distributions

As in Section 5.5, the total $1\mu^+$ and $2\mu^+$ rates were plotted as a function of inverse density to obtain the prompt signals, measured by the intercepts, and the non-prompt $1\mu^+$ rate, measured by the slope of the $1\mu^+$ fitted line. The plot for the total rates is given in Figure 6-1.

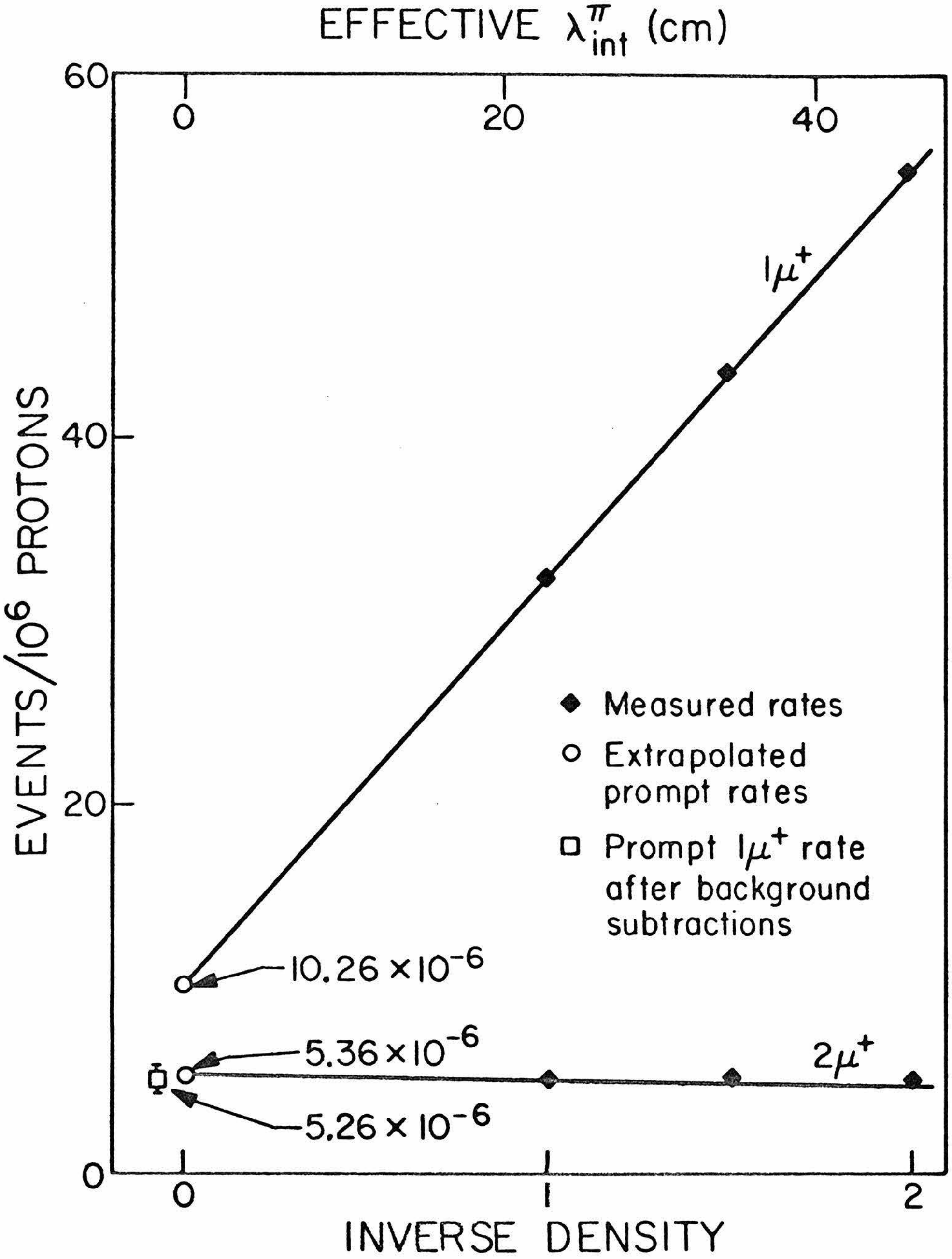

Figure 6-1: (a) The measured $1\mu^+$ and $2\mu^+$ rates from the p_t trigger versus effective inverse density. The lines are least squares fits to the measured rates; the values of the intercepts obtained from the fit are shown. Also shown is the value of the prompt $1\mu^+$ rate after background subtraction. [Inverse density = 1 corresponds to $\rho = 5.9$ g/cm^3.]

The $2\mu^+$ rates in this plot are observed to be consistent with a small negative slope, and in fact the least squares fit yields a slope of $(0.201 \pm 0.094) \times 10^{-6}$ events/proton. This value is consistent with the slope of $(-0.159 \pm 0.161) \times 10^{-6}$ predicted by the 2μ Monte Carlo as the difference between the compacted and expanded rates. The difference is the result of the change in trigger acceptance with density configuration, This acceptance is discussed further in the next section.

The prompt $1\mu^+$, non-prompt $1\mu^+$, and prompt $2\mu^+$ distributions in p and p_t of the μ^+, obtained from the extrapolation procedure with no background subtractions or acceptance corrections, are shown in Figures 6-2 through 6-4.

6.6 Backgrounds in the Prompt 1μ Signal

The possible sources of background in the prompt $1\mu^+$ signal were the same as those considered for the high p data in Section 5.6. Again, halo muons from the beam and hyperon decays were found to be completely negligible as background sources. The two significant backgrounds were decays from π's and K's occurring downstream of the variable density section of the calorimeter and $\mu^+\mu^-$ events for which the μ^- was undetected. The calculation of both these backgrounds was complicated by the possibility of an acceptance change with density configuration.

An acceptance change could result from several effects of the density change. The most prominent effect was that the origin of the muon trajectories moved upstream or downstream as the steel plates moved, so that the total angle subtended by the S1-S2 hodoscope changed. This hodoscope was required in the trigger (see Section 3.3). As the origin

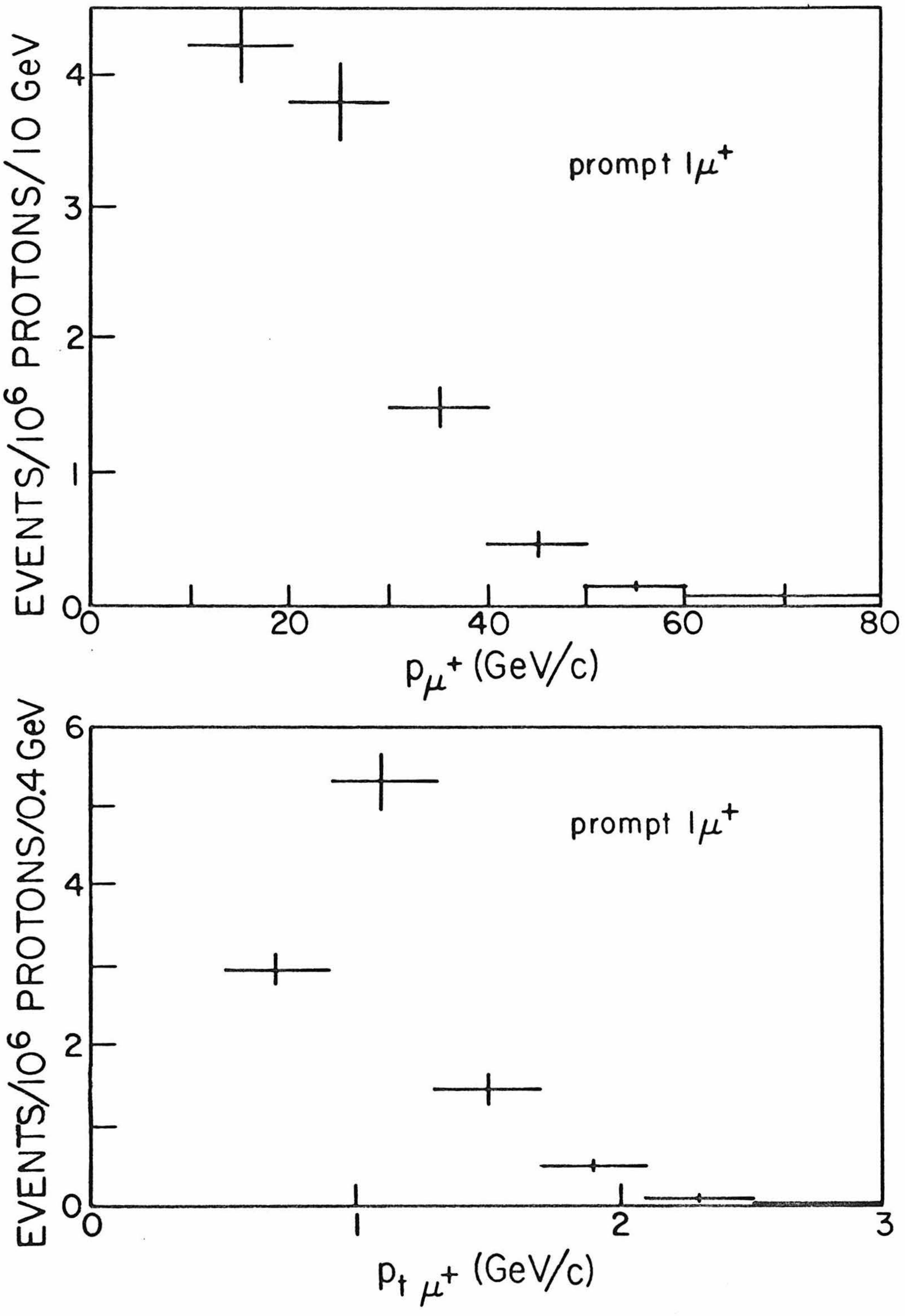

Figure 6-2:

(a) The distribution of prompt $1\mu^+$ events versus $p_{\mu+}$, before background subtractions.

(b) The distribution of prompt $1\mu^+$ events versus $p_{t\mu+}$, before background subtractions.

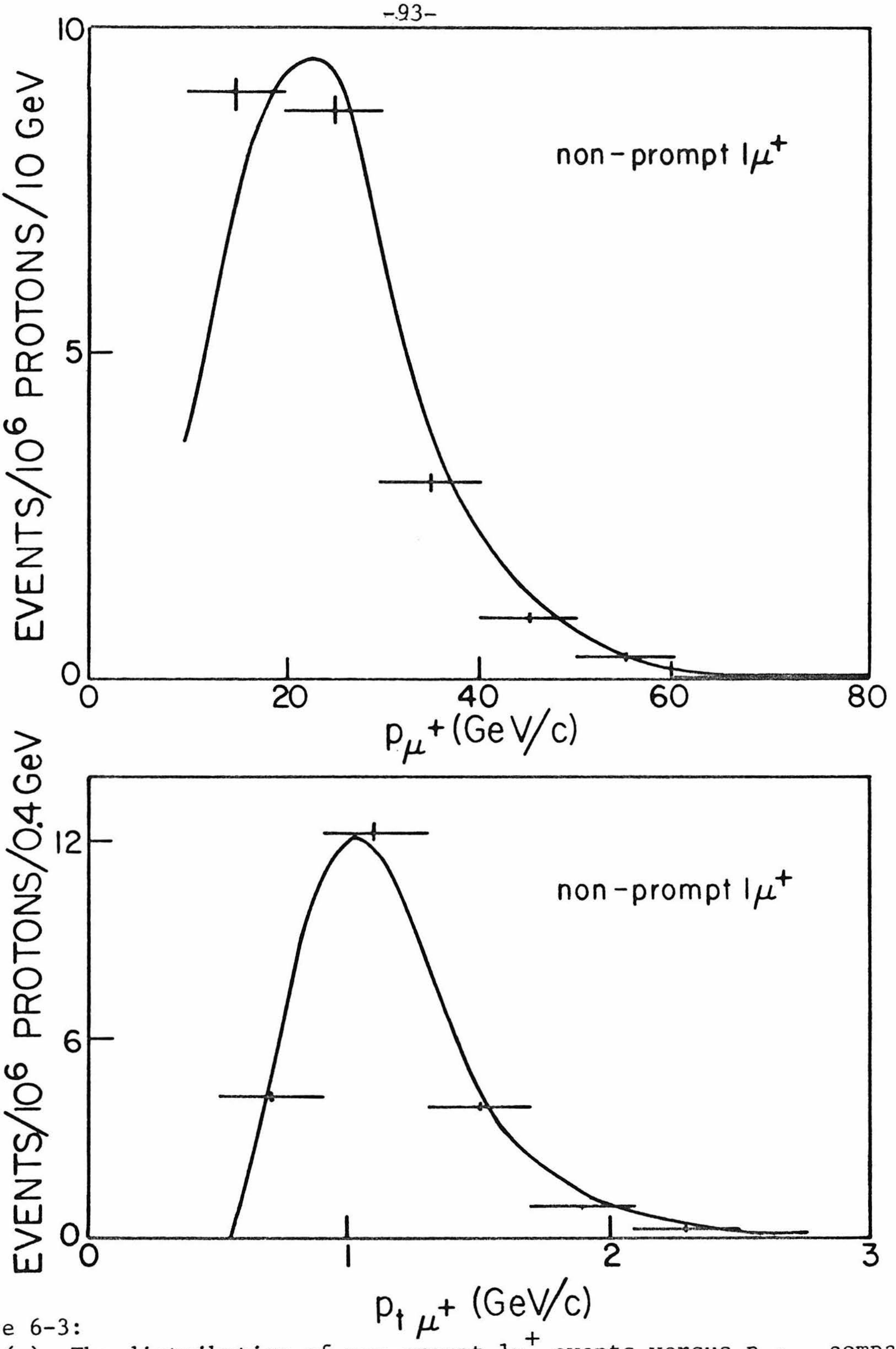

Figure 6-3:

(a) The distribution of non-prompt $1\mu^+$ events versus p_{μ^+}, compared to the Monte Carlo distribution (curve).

(b) The distribution of non-prompt $1\mu^+$ events versus $p_{t\mu^+}$, compared to the Monte Carlo distribution (curve).

The Monte Carlo was normalized to the total number of events.

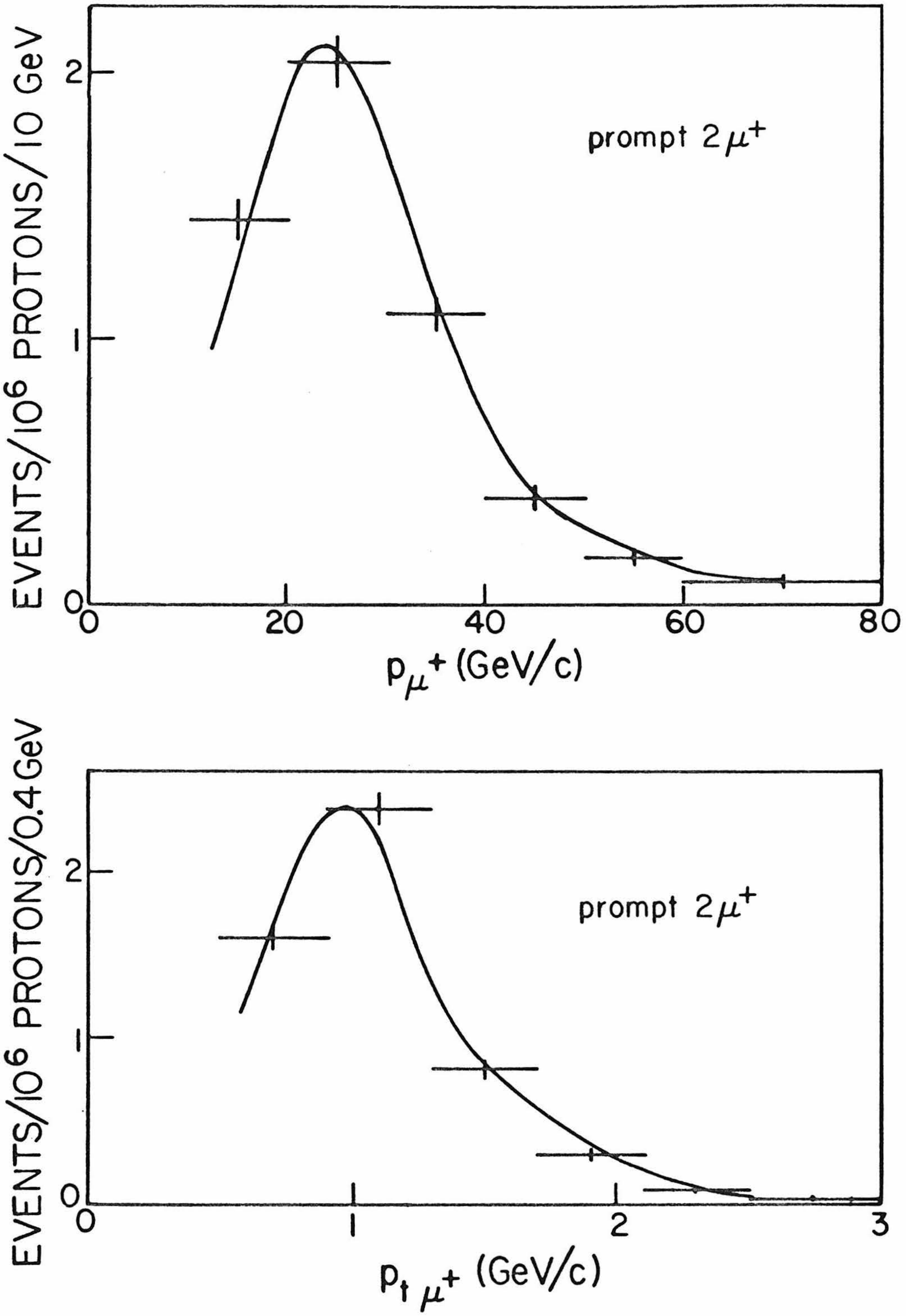

Figure 6-4:

(a) The distribution of $2\mu^+$ events versus p_{μ^+}, compared to the Monte Carlo prediction (curve).

(b) The distribution of $2\mu^-$ events versus $p_{t\mu^+}$, compared to the Monte Carlo prediction (curve).

The Monte Carlo was normalized to the total number of events.

Table 6-1: Total Number of Interacting Protons at Each Density

Density	Measured* # of Protons	Fraction Removed* by Beam Cuts	<S2 Efficiency>*	Corrected* # of Protons
Compacted	2.5533×10^9	.259	.992	1.8726×10^9
Semi-expanded	1.6912×10^9	.182	.992	1.3701×10^9
Expanded	1.3752×10^9	.176	.993	1.1239×10^9

*After bad runs were omitted.

Table 6-2: Number of Events and Corrections at Each Density

Density	$1\mu^+$ Events	$2\mu^+$ Events	Calculated # of Unassociated $2\mu^+$ Events	Corrected # of $2\mu^+$ Events
Compacted	60756	11322	1731.5 ± 7.4	9590.5 ± 106.7
Semi-expanded	59721	8611	1534.8 ± 6.7	7076.2 ± 93.0
Expanded	61392	7453	1958.4 ± 8.7	5494.6 ± 86.8

Table 6-3: Rates and Linear Fits at Each Density

Density	$1\mu^+$ Rate Events/10^6 Protons	$2\mu^+$ Rate Events/10^6 Protons
Compacted	32.44 ± .13	5.12 ± .06
Semi-expanded	43.59 ± .18	5.16 ± .07
Expanded	54.62 ± .22	4.89 ± .08
Intercept	10.26 ± .34	5.36 ± .14
Slope	22.20 ± .25	-0.20 ± .09

of a given trajectory moves downstream, if its radius at the hodoscope is near the hole its trigger efficiency drops; if its radius is near the outer edge of S2 its efficiency rises. Therefore, the effective acceptance change was a function of the distribution in p and p_t of the muon and of the distribution in z of the muon trajectory origins. The best way to include all the variables was to run Monte Carlos of non-prompt decay and 2μ production at both the compacted and expanded density and make an extrapolation similar to that performed for the data. This was done, with results described below.

(1) Muons from $\mu^+\mu^-$ events with the μ^- unobserved. The 2μ Monte Carlo was run with only resonance and continuum calculations because the total Bethe-Heitler contribution to the p_t trigger was found to be $< 0.06 \times 10^{-6}$ out of a 2μ rate of 5×10^{-6} events/proton. The Monte Carlo followed the shower through the third generation of hadron production. The acceptance change was measured as (3.1 ± 3.1)%, consistent with no effect. The p and p_t distribution of the misidentified 2μ events and the identified 2μ events were determined from the extrapolation and the ratio of background to signal as a function of p and p_t was calculated. The ratios were multiplied by the observed 2μ distributions to obtain the estimated background distribution. This background was found to be (27.6 ± 4.2)% of the raw prompt 1μ^+ signal. The Monte Carlo 2μ^+ distributions are compared to the data in Figure 6-4.

(2) Muons from downstream decays of π's and K's. The π and K decays were calculated through the fourth generation in the shower. These decays contained another source of difference between the compacted

and expanded rates besides the acceptance change. In the compacted configuration, there was a gap between plates 41 and 42 which was not present in the expanded configuration (see Figure 2-4). The decay rate in the gap will therefore be doubled when the total π and K decay rates are extrapolated to infinite density (Figure 6-5). The Monte Carlo indicated a total acceptance change for the non-prompt π and K decays of (0.1 ± 1.0)%. The error on the background subtraction could be much improved by calculating the subtraction using only the compacted run, assuming no acceptance change but including the effect of the gap decays, instead of performing an extrapolation of expanded and compacted. The two methods yielded consistent results. With the calculation method, the background was found to be 21% of the raw prompt $1\mu^+$ signal. The non-prompt Monte Carlo distributions are compared to the data in Figure 6-3.

The p and p_t distributions of the backgrounds are shown in Figure 6-6, and the prompt $1\mu^+$ distributions after background subtraction are plotted in Figure 6-7. The total corrected prompt $1\mu^+$ rate was $(5.26 \pm 0.61) \times 10^{-6}$ events/proton.

6.7 Error Analysis

The errors shown in Table 6-3 and Figures 6-1 through 6-4 are the statistical errors from the density extrapolations. As in the error analysis for the high p data (Section 5.7), the primary sources of systematic error are the two background subtractions. The π and K decay background sensitivity was analyzed with respect to the same variations described in Section 5.7. In the high p_t data also, the background was insensitive to the π/K ratio but could accommodate a 30% increase due to

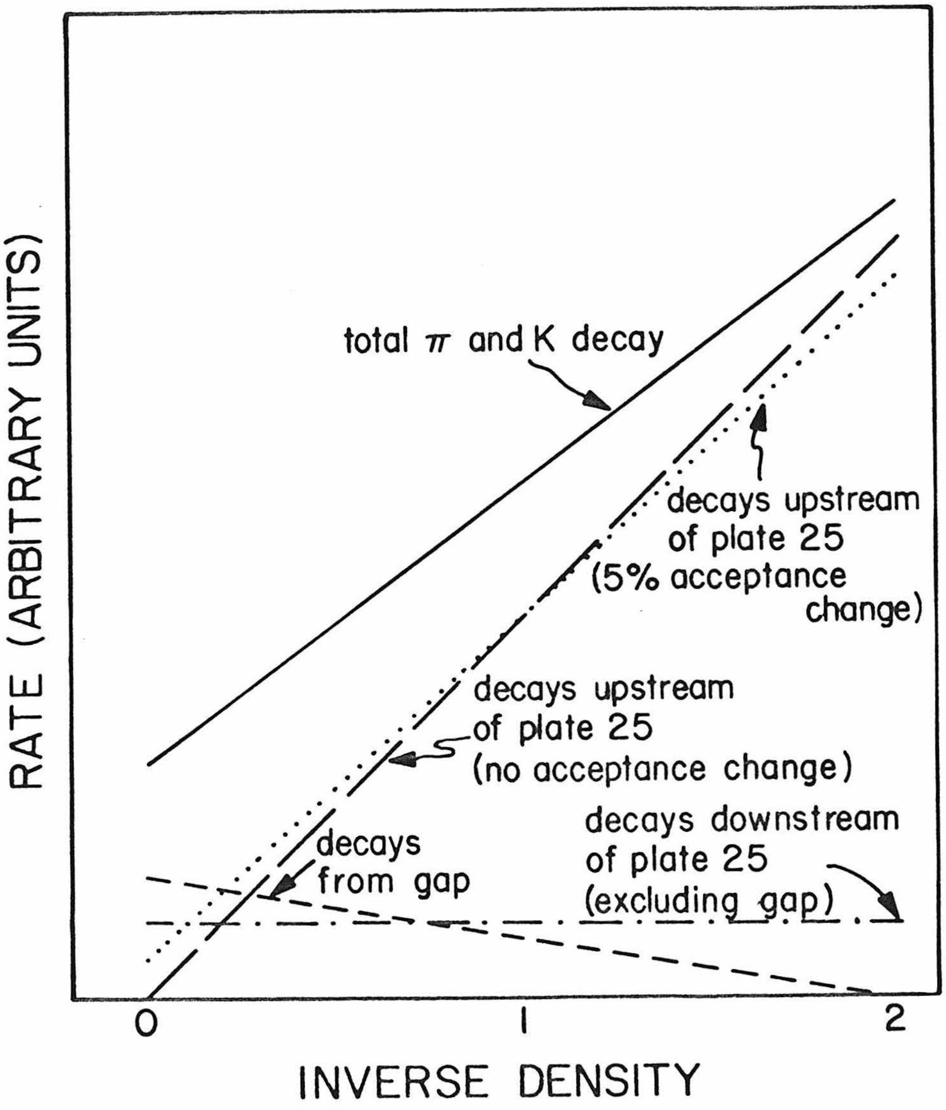

Figure 6-5: Schematic of the contribution of non-prompt decays from different sections of the calorimeter. The size of the downstream and gap decays compared to the upstream decays, and the size of the acceptance change, are exaggerated to show the effects more clearly. The solid line is the sum of the contributions; its intercept at $1/\rho = 0$ represents the background in the prompt 1μ signal from π and K decays.

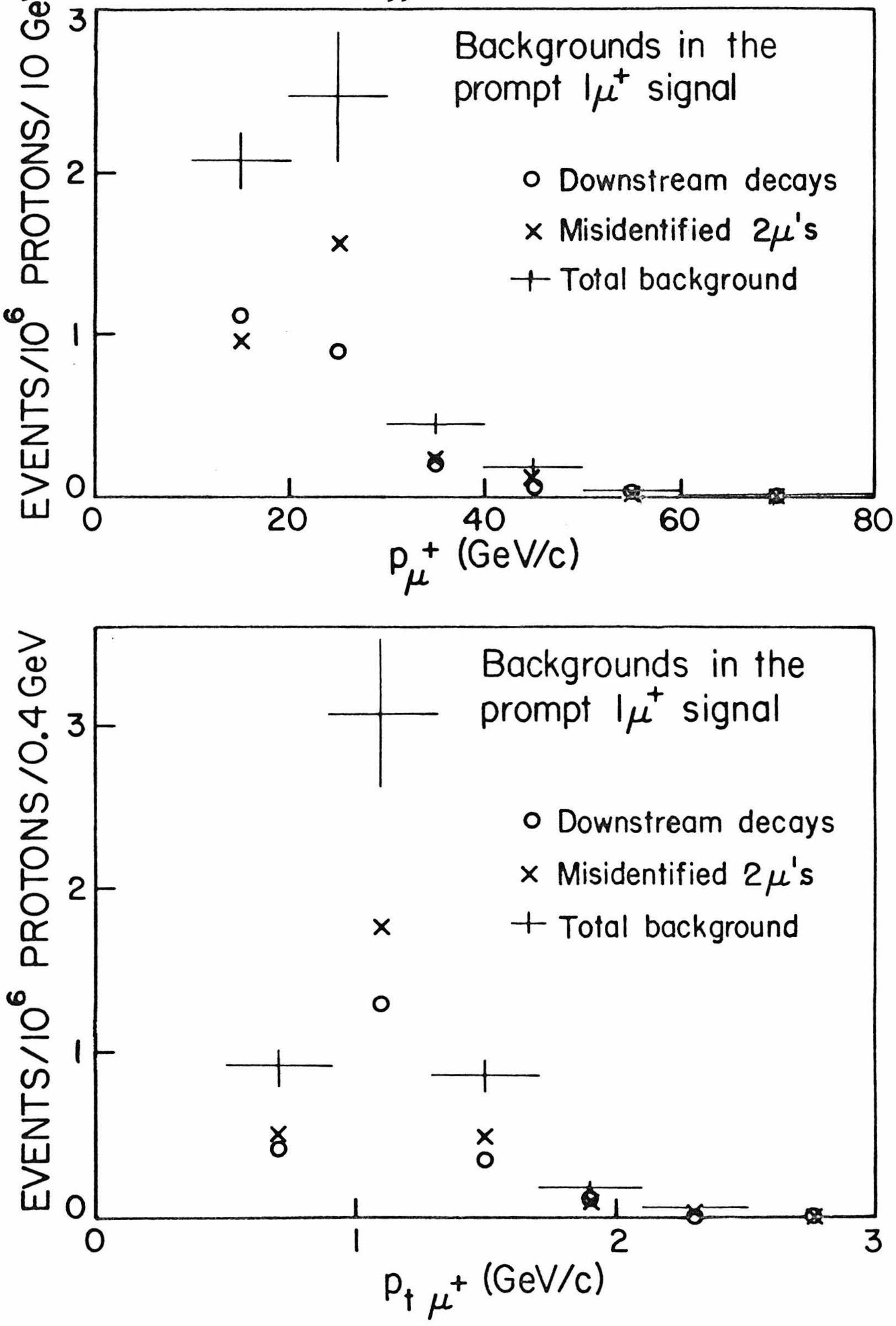

Figure 6-6:

(a) The calculated backgrounds in the prompt $1\mu^+$ signal versus P_{μ^+}.

(b) The calculated backgrounds in the prompt $1\mu^+$ signal versus Pt_{μ^+}.

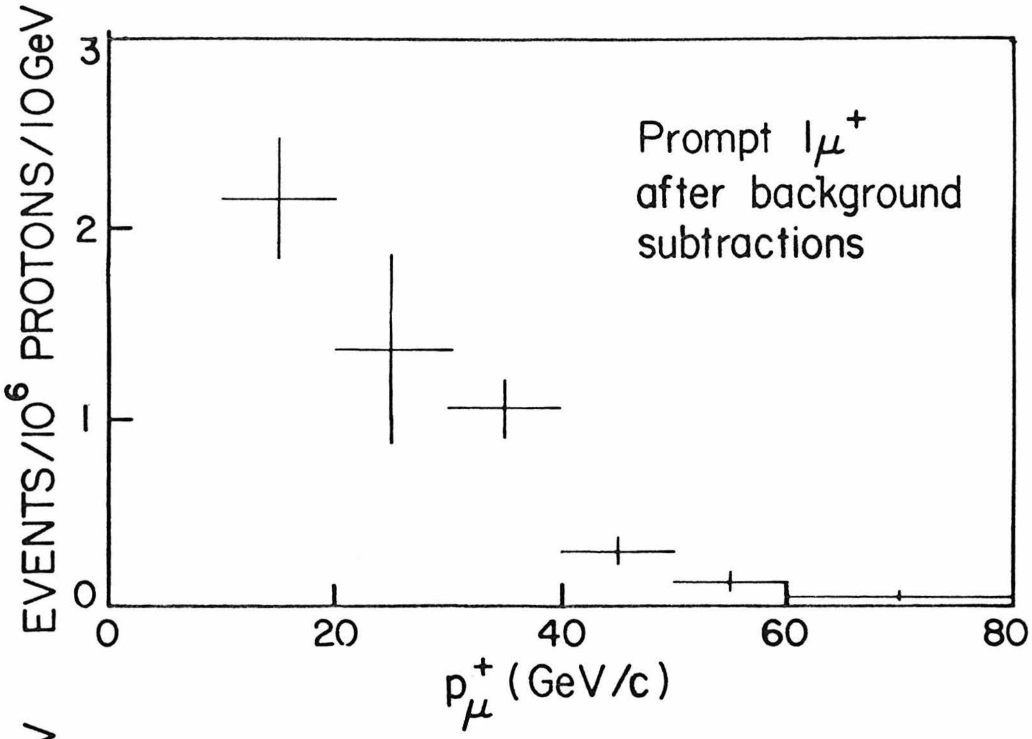

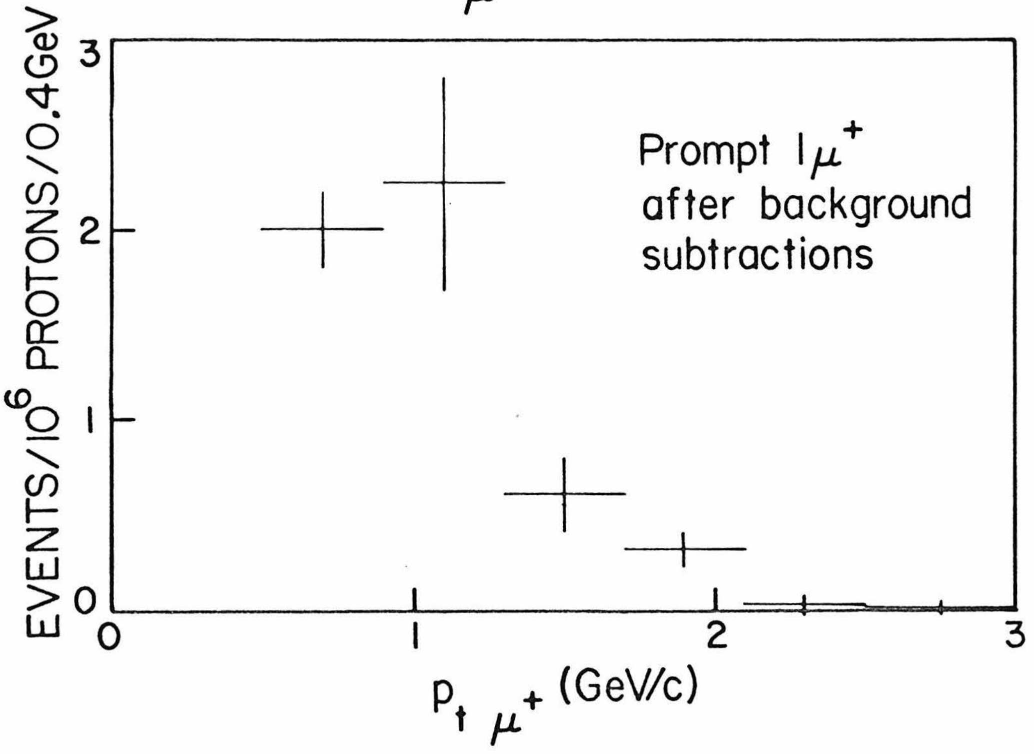

Figure 6-7:

(a) The prompt $1\mu^+$ distribution in p_{μ^+} after subtraction of the backgrounds shown in Figure 6-6.

(b) The prompt $1\mu^+$ distribution in $p_{t\mu^+}$ after subtraction of the backgrounds shown in Figure 6-6.

variation of the third and fourth generation without disturbing the observed agreement between Monte Carlo and data for the non-prompt distributions shown in Figure 6-3. For the p_t trigger data, however, the empirical check provided by the distribution in longitudinal interaction position of the prompt $1\mu^+$ rate resulted in a somewhat stricter limit on the background. The fit to this distribution shown in Figure 6-8 yielded a background estimate of (16 ± 6)%, which should be compared with the Monte Carlo calculation of 21% with a statistical error of 1.5%.

The major error in the misidentified 2μ subtraction did not come from the knowledge of Bethe-Heitler production, since that contribution to the 2μ rate for the p_t trigger was negligible, but from the uncertainty in the size of the acceptance change with density. The Monte Carlo calculation gave (3 ± 3)% for the value of the acceptance change, and this error corresponded to a 15% uncertainty in the size of the background subtraction.

For the high p_t data, the statistical error in the total prompt $1\mu^+$ signal was comparable to the systematic errors. In the subtraction of the background p and p_t distributions, a systematic error was assigned to cover the uncertainty in the acceptance change as a function of p and p_t. The statistical errors in the raw prompt $1\mu^+$ signal still dominated the systematic errors in the p and p_t distributions shown in Figure 6-7.

6.8 Comparison with High p Data

The high p_t data and high p data, as mentioned before, provided data in completely different kinematic regions for prompt muon production. Both analyses yielded a significant prompt $1\mu^+$ signal. The rates and

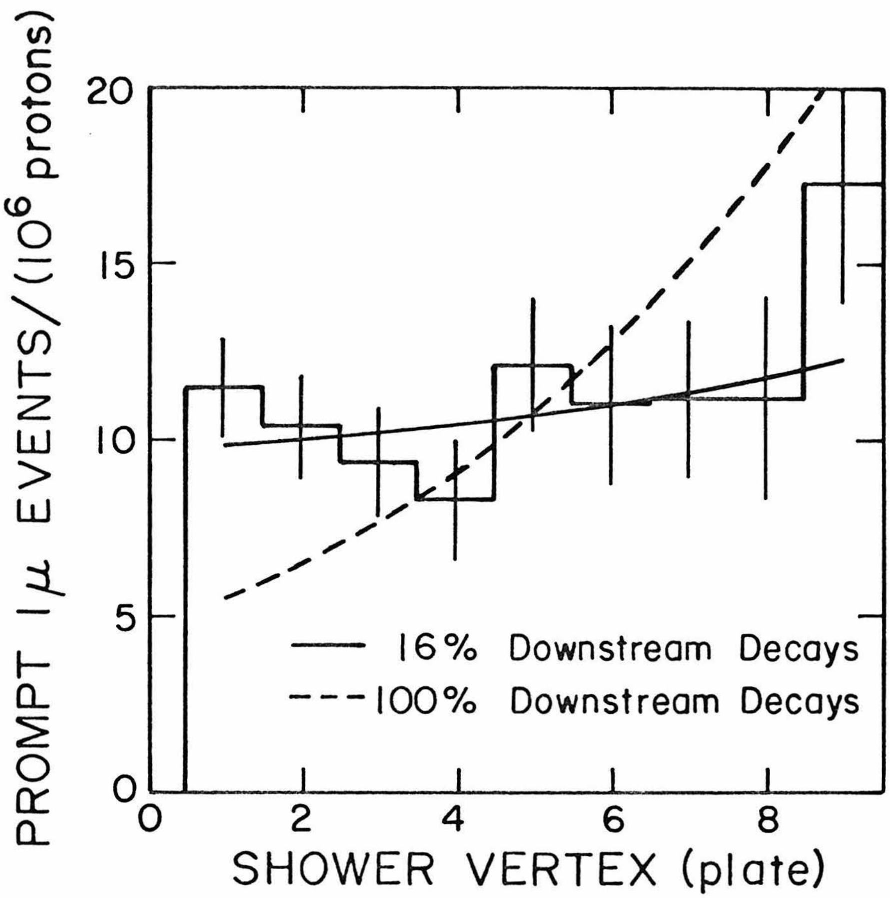

Figure 6-8: The distribution of the prompt $1\mu^+$ rate versus the plate number in which the 400 GeV interaction took place. (One plate = 3.8 cm of steel.) Also shown are the best fit to a flat component plus a downstream decay component (which gives (16±6)% downstream decays in the prompt $1\mu^+$ rate) and the shape expected if there were 100% downstream decays. The calculated size of the downstream decays from the Monte Carlo was 21%.

relative subtractions for the two data sets are listed in Table 6-4.

Table 6-4: Prompt 1μ Rates from the High p and p_t Triggers*

	Raw prompt 1μ	Downstream decays	Misidentified 2μ's	Corrected prompt 1μ
High p ($1\mu^-$)	8.19±1.03	0.40±0.07 ±0.12	1.71±0.08 ±0.23	6.08±1.04 ±0.41
High p ($1\mu^+$)	7.83±1.31	1.13±0.11 ±0.34	1.99±0.09 ±0.23	4.71±1.32 ±0.26
High p_t ($1\mu^+$)	10.26±0.42	2.16±0.13 ±0.22	2.83±0.42 ±0.42	5.26±0.61 ±0.48

---

*All rates quoted are events/10^6 protons; the second error listed is the systematic error.

CHAPTER 7

INTERPRETATION OF THE PROMPT SINGLE MUON SIGNAL

7.1 Introduction

The data analysis of Chapters 5 and 6 established the existence of a prompt muon signal at moderately high p and p_t. The high p data analysis showed that the signal exists for both μ^+ and μ^- at approximately equal levels. The prompt 1μ rates were converted to directly observed cross sections, assuming that the production of the prompt 1μ source depended linearly on target atomic number A. These cross sections are given, in nb/nucleon, in Table 7-1. To calculate a total cross section required a model for the types of source particle produced, their kinematic produced distributions, and their branching ratio into muonic final states. The known heavy particles with appreciable weak decays are the lightest charmed mesons D^+, D^-, D^o, $\overline{D^o}$, and F^+, F^-; the lightest charmed baryon Λ_c^+, the heavy lepton τ, and the lightest bottom particle (whose existence has yet to be demonstrated experimentally). An order of magnitude calculation of rates (see Section 7.8) was enough to exclude τ's and bottom particles as sources of the rates observed in this experiment. Charm production remained a good candidate to explain the signal, so models for charm production were used to fit the data. In this chapter, both the directly observed rates and the model-dependent charm cross sections are compared with the results of other experiments. Also, the limits placed by the data of this thesis on the parameters of some specific charm production models are examined. Section 7.7 compares the existing data on hadroproduction of charm to the theoretical calculations.

Table 7-1: Directly observed cross sections, calculated with the assumption of linear A dependence.

	observed prompt 1μ (events/proton)	σ_{observed} (nb/nucleon)
$1\mu^+$(p_t trigger)	$(5.3 \pm .8) \times 10^{-6}$	72.1 ± 10.9
$1\mu^+$(high p trigger)	$(4.7 \pm 1.3) \times 10^{-6}$	63.9 ± 17.7
$1\mu^-$(high p trigger)	$(6.1 \pm 1.1) \times 10^{-6}$	83.0 ± 15.0

$$\sigma_{\text{observed}} = \#\,\frac{\text{events}}{\text{proton}} \cdot \left(\frac{\sigma_{p-Fe}}{56}\right) \text{nb}/\frac{\text{events}}{\text{proton}}$$

7.2 Comparisons to Other Prompt Single Muon Searches

Only two other experiments have sought to measure the fraction of single muons compared to muon pairs in the prompt signal. One experiment [23] measured the polarization of prompt muons and thus obtained a limit on the number of muons from weak decays (polarized) rather than from electromagnetic sources (unpolarized). Another [24] performed a separation into 1μ and 2μ events similar to the method of this thesis, but with smaller efficiency for identifying the second muon. The first experiment used a 400 GeV proton beam on a copper target and the second used a 200 GeV proton beam on an iron target. The results of this experiment for the ratio of $1\mu/2\mu$ from the two data sets at high p_t and high p compared with those of References 23 and 24 are shown in Figures 7-1 and 7-2. Note that the 2μ rates from this experiment had the calculated number of misidentified 2μ's added in. The 2μ sample was defined so as to have the same trigger efficiency as the 1μ sample, so no correction for trigger efficiency was necessary.

7.3 Calculation of Total Charm Cross Sections

As mentioned above, the conversion of the rate measured in this experiment to a total cross section required a model. Within the framework of the models, the range of parameters consistent with the observed p and p_t distributions was determined, and cross sections were calculated for that range of parameters.

7.3.1 The Production Models

Two simple models were used, both of which assumed that the predominant source of prompt single muons would be the D meson. The higher

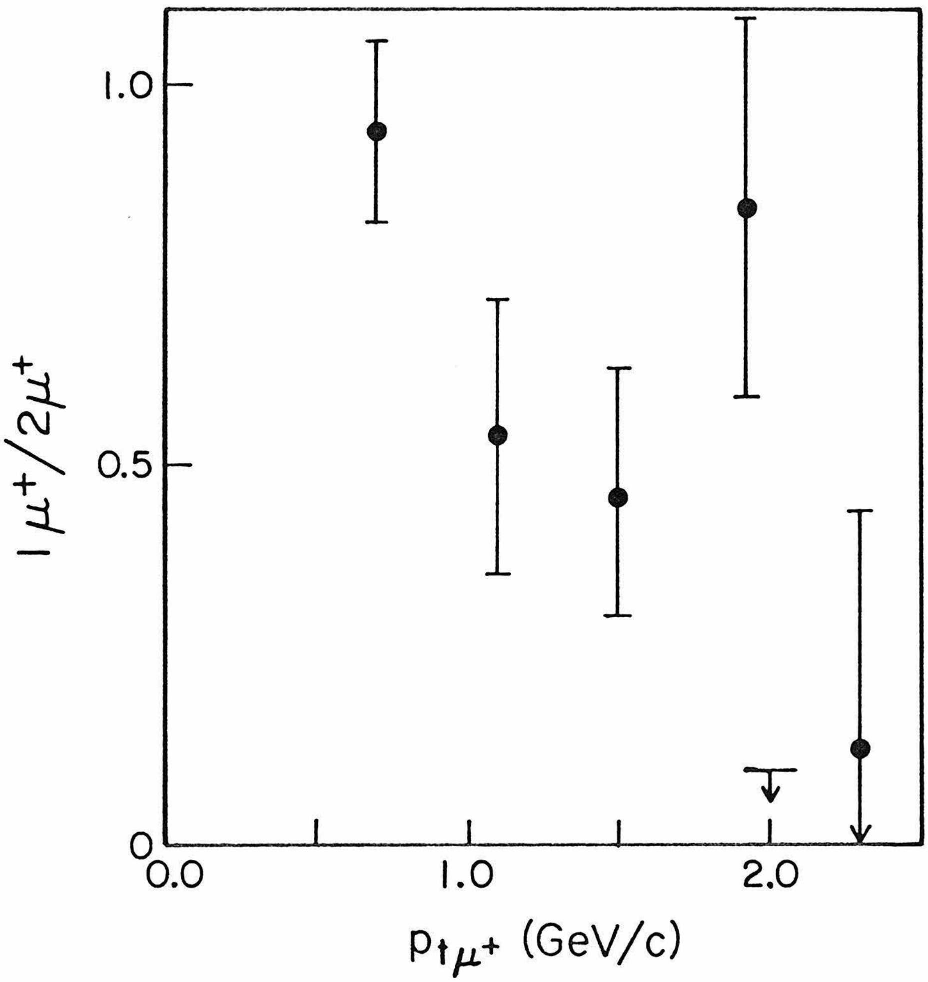

Figure 7-1: The ratio $1\mu^+/2\mu^+$ from the p_t trigger data plotted versus $p_{t\mu}{}^+$. Also shown is the limit on $1\mu/2\mu$ extracted from a polarization measurement at p_t = 2 GeV/c [23].

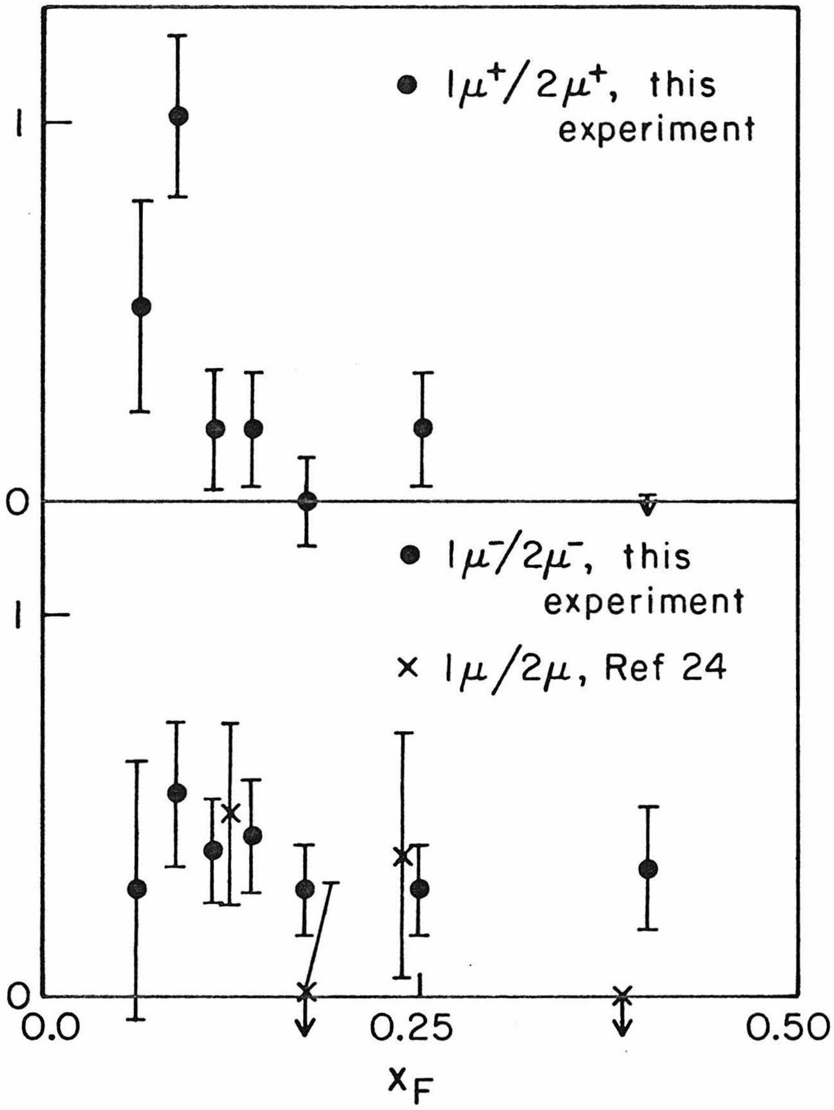

Figure 7-2: The ratios $1\mu^+/2\mu^+$ and $1\mu^-/2\mu^-$ from the high p data plotted versus x_F. Also shown is the ratio $1\mu/2\mu$ measured by the experiment of Reference 24 using 200 GeV protons.

mass D* states cascade down to the D states via strong and electromagnetic decays. Statistical arguments regarding the production ratios and knowledge of the D* cascades indicate[25] that the final result will be a ratio of $D^o:D^+$ production of 3:1. The ratio of D:F production depends on the extent of the SU(3) symmetry breaking; from Reference 25 the ratio is bounded by 2:1 for perfect symmetry and 6.7:1 for symmetry breaking calculated from the ρ:K* ratio. Since this experiment observed only muonic decays, the branching ratios into muons were also relevant. The Delco experiment at SPEAR[26] has measured different semileptonic branching ratios for the D^+ and D^o - the values are $(24 \pm 4)\%$ and <5% respectively. The semileptonic widths calculated from these numbers imply different lifetimes as well for the D^+ and D^o, and such a difference is confirmed by an emulsion experiment using a neutrino beam[27]. That experiment also measured the F lifetime to be close to that of the D^o, indicating a small semileptonic branching ratio for the F as well[28]. Putting these results together, the best assumption was that this experiment, in measuring muonic decays, was observing primarily $D^{\pm}$ mesons. The question of possible contributions from Λ_c-D associated production is addressed in Section 7.6.

The two models of D production used were the single D model, in which D's were produced with an invariant cross section proportional to $(1-x_F)^{\beta} \cdot e^{-\alpha p_t}$, and the continuum model, in which the $D\bar{D}$ pairs were produced in a composite state C with mass m_C, whose invariant cross section was proportional to $1/m_C^3 \cdot (1-x_{FC})^{\beta} \cdot e^{-\alpha p_{tC}} \cdot e^{-\gamma m_C/\sqrt{s}}$. An average branching ratio of 8% into muon states, distributed 60% into

$K\mu\nu$ and 40% into $K^*\mu\nu$[26], was assumed in the total cross section calculations.

7.3.2 Determination of Model Parameters

Monte Carlo simulations of the continuum model for a range of values of α, β, and γ were run for both the p_t trigger and the high p trigger, to calculate the total trigger efficiency and the expected p and p_t distributions of the muons. Tables 7-2 and 7-3 list the χ^2 values obtained for the fits to the p and p_t distributions for μ^+ and μ^- from the high p trigger, where each model was separately normalized for μ^+ and μ^-. The points to note from these tables are the following ones:

(1) The fit to the p_{μ^+} distribution favored a high value of β (steep x_F dependence) while the p_{μ^-} fit favored a low value. However, both distributions could be acceptably fit with β in the range 3-4; the statistical significance of the difference in distributions was ~ 1.5 standard deviations.

(2) The principal conclusion to be drawn from the p_t distribution fits was that they excluded very small (< 0.5) values of $\gamma/\sqrt{s}$; α was scarcely constrained at all by these data.

Normalizing the $D\bar{D}$ continuum model separately for μ^+ and μ^-, as above, is not quite a physically consistent procedure. If only $D\bar{D}$ pairs were produced, the same normalization factor should fit the μ^+ and μ^- distributions. The ratio of $1\mu^+$ and $1\mu^-$ signals should be ~ 1.1 in most continuum models (not 1.0, because of the difference in trigger efficiency at low p). The observed ratio was 0.77 ± 0.26, within about one standard deviation of the expected value. Simultaneous fits to the μ^+ and μ^- distributions, requiring a single normalization parameter, were performed; and the results are summarized in Table 7-4. The same trends are observable in these fits as in the separately normalized ones.

The information from the continuum model fits to the high p data can be summarized as the following set of constraints:

$$\alpha > 0.4$$
$$2.5 < \beta < 5.0$$
$$\gamma > 0.5\sqrt{s}$$

The criterion used in setting these limits was that a set of parameters gave an acceptable fit if each of the four distributions (p_{μ^+}, $p_{t\mu^\pm}$, p_{μ^-}, $p_{t\mu^-}$) had a χ^2 corresponding to a confidence level of >4.6%. This procedure is equivalent to requiring a two standard deviation fit if χ^2 is distributed normally. Figure 7-3 displays graphically some of the χ^2 values.

Results from fitting the continuum model to the p and p_t distributions of the μ^+ data from the p_t trigger are summarized in Table 7-5. These data were not very sensitive to β or γ (except that they also excluded very small γ); they required $\alpha > 0.4$. However, the model did not give an acceptable fit to the p_t distribution, by the criterion described above. The best χ^2 obtained for the p_t distribution was 18 for 5 degrees of freedom (d.o.f.), for a confidence level of only 0.3%. The cause of the bad χ^2 values was the relatively large signal in the bin 0.5 GeV/c < p_t < 0.9 GeV/c (see Figure 6-7); only a model with a very steep p_t dependence could reproduce this level, given the small acceptance in that bin,

Table 7-2: χ^2 values from continuum model fits to high p μ^+ data.

$$\text{Model: } E\frac{d^3\sigma}{dp^3} \propto \frac{1}{m^3}\, e^{-\gamma m/\sqrt{s}}\, (1 - |x_F|)^{\beta}\, e^{-\alpha p_t}$$

χ^2 for the $p_{t\mu^+}$ distribution: (4 d.o.f. : acceptable fit → $\chi^2 < 9.7$)

	$\gamma/\sqrt{s}$ \ α	.400	1.00	2.00	3.50	4.50	10.0
	.177			16.3			
	.527			8.0			
$\beta = 3.00$	1.00	14.4	11.2	4.0	2.2	1.9	1.5
	2.00	11.0	6.6	1.9	1.6	1.6	1.5
	3.54	8.1	3.9	1.3	2.1	2.4	2.5

	$\gamma/\sqrt{s}$ \ β	2.00	3.00	4.00	5.00	6.00
	.177	13.6	16.3	22.8	26.2	28.7
	.527	13.6	8.0	9.3		
$\alpha = 2.00$	1.00	2.3	4.0	5.3	7.4	9.7
	2.00	1.0	1.9	1.8	2.6	3.6
	3.54	0.8	1.3	0.8		

χ^2 for the p_{μ^+} distribution: (6 d.o.f. : acceptable fit → $\chi^2 < 12.8$)

	$\gamma/\sqrt{s}$ \ α	.400	1.00	2.00	3.50	4.50	10.0
	.177						
	.527			10.8			
$\beta = 3.00$	1.00	10.3	10.1	11.0	12.1	12.2	12.1
	2.00	9.8	10.0	11.6	13.0	13.1	12.4
	3.54	9.6	10.1	12.3	13.9	14.0	13.0

	$\gamma/\sqrt{s}$ \ β	2.00	3.00	4.00	5.00	6.00
	.177	13.5		10.7	10.2	10.0
	.527		10.8			
$\alpha = 2.00$	1.00	13.6	11.0	8.7	7.7	7.3
	2.00	14.8	11.6	8.9	7.5	7.3
	3.54	16.0	12.3	9.5		6.8

Table 7-3: χ^2 values from continuum model fits to high p μ^-

$$\text{Model: } E\,\frac{d^3\sigma}{dp^3} \propto \frac{1}{m^3}\, e^{-\gamma m/\sqrt{s}}\,(1 - |x_F|)^{\beta}\, e^{-\alpha p_t}$$

χ^2 for the $p_{t\mu^-}$ distribution: (4 d.o.f. : acceptable fit → $\chi^2 < 9.7$)

	$\gamma/\sqrt{s}$ \ α	.400	1.00	2.00	3.50	4.50	10.0
	.177			24.5			
	.527			10.8			
$\beta = 3.00$	1.00	1.0	8.1	5.2	3.9	4.2	4.7
	2.00	11.4	6.6	3.6	5.9	7.0	9.1
	3.54	11.9	6.1	4.1	9.2	11.1	15.1

	$\gamma/\sqrt{s}$ \ β	2.00	3.00	4.00	5.00	6.00
	.177	18.3	24.5	30.1	34.7	38.1
	.527		10.8			
$\alpha = 2.00$	1.00	4.8	5.2	6.7	8.7	11.1
	2.00	4.8	3.6	3.4	4.0	5.0
	3.54	6.1	4.1	3.1		

χ^2 for the p_{μ^-} distribution: (6 d.o.f. : acceptable fit → $\chi^2 < 12.8$)

	$\gamma/\sqrt{s}$ \ α	.400	1.00	2.00	3.50	4.50	10.0
	.177						
	.527			7.3			
$\beta = 3.00$	1.00	15.0	10.1	7.1	6.3	6.2	6.0
	2.00	15.8	10.4	7.1	6.4	6.3	5.3
	3.54	15.7	10.6	7.4	6.9	6.8	5.4

	$\gamma/\sqrt{s}$ \ β	2.00	3.00	4.00	5.00	6.00
	.177	4.0		10.6	14.0	17.1
	.527		7.3			
$\alpha = 2.00$	1.00	4.0	7.1	11.0	15.4	20.1
	2.00	4.4	7.1	10.5	14.4	18.9
	3.54	5.0	7.4	10.4		

Table 7-4: χ^2 values from continuum model fits to high p μ^+ and μ^- data with single normalization parameter.

$$\text{Model:} \quad E\frac{d^3}{dp^3} \propto \frac{1}{m^3}\, e^{-\gamma m/\sqrt{s}}\, (1 - |x_F|)^{\beta}\, e^{-\alpha p_t}$$

χ^2 for the $p_{t\mu^+} + p_{t\mu^-}$ distributions: (9 d.o.f. : acceptable fit $\rightarrow \chi^2 < 17.1$)

	$\beta=2.00$			$\beta=3.00$			$\beta=4.00$		
$\gamma/\sqrt{s}$ \ α	1.00	2.00	3.50	1.00	2.00	3.50	1.00	2.00	3.50
1.00	20.0	9.4	9.8	25.4	13.7	8.0	31.3	15.7	8.8
2.00	12.9	8.0	13.9	15.9	9.6	9.6	22.0	8.2	7.1
3.54	9.4	9.3	16.7	12.9	7.3	14.4	17.2	5.2	11.1

χ^2 for the $p_{\mu^+} + p_{\mu^-}$ distributions: (13 d.o.f. : acceptable fit $\rightarrow \chi^2 < 22.5$)

	$\beta=2.00$			$\beta=3.00$			$\beta=4.00$		
$\gamma/\sqrt{s}$ \ α	1.00	2.00	3.50	1.00	2.00	3.50	1.00	2.00	3.50
1.00	20.1	18.1	20.0	19.4	18.1	17.9	21.3	18.4	18.2
2.00	21.0	19.6	22.3	19.4	18.6	19.0	20.8	18.0	18.4
3.54	22.0	21.5	23.0	20.0	18.8	21.0	20.7	18.5	19.3

but such a model did not fit the shape above p_t of 0.9 GeV/c. Fitting only the data above 0.9 GeV/c generated acceptable fits for α in the range $1 < \alpha < 3$.

The continuum model fits to the p_t data were in agreement with the constraints already determined by the high p data.

Using the single D model, the high p μ^+, high p μ^-, and high p_t data were fit with various values of α and β (note that these now describe the distributions of the D rather than of the $D\bar{D}$ pair). The high p data required $\alpha > 1$ for μ^+ fits and $1 < \alpha < 3$ for μ^- fits, both of which were insensitive to β. The p_t data were insensitive to β, but required $\alpha > 1$, again fitting the data above $p_t = 0.9$ GeV/c. The χ^2 values for these fits are given in Table 7-6.

A variation of the single D model was also tried. The model was as before, except that the p_t dependence was changed to e^{-6m_t}, where $m_t = \sqrt{m_D{}^2 + p_{tD}{}^2}$. The χ^2 values for these fits with $\beta = 3$ for both the high p and p_t data are given in Table 7-7. This model was not an acceptable fit to either of the data sets by the standard criterion (although it was not significantly worse for the high p_t data than the regular single D model).

7.3.3 Total Cross Sections

The total detection efficiency for the range of models which gave acceptable fits to the data varied from 1 to 3% for the high p data (for muons of one sign) and from 1 to 3% for the high p_t data. Table 7-8 lists efficiencies and corresponding total cross sections for the allowed range of parameters for the two data sets. For the high p data, the

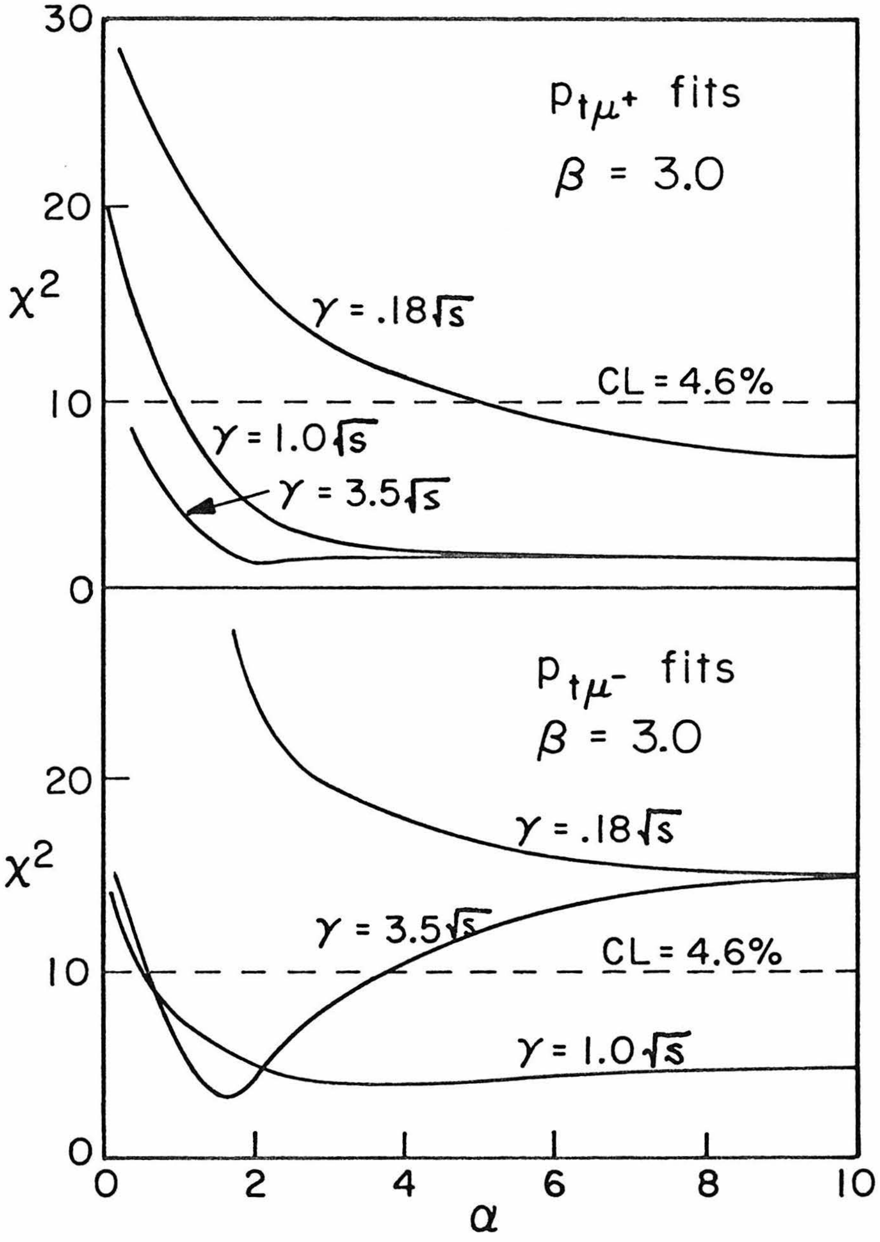

Figure 7-3: χ^2 values for some continuum model fits to the p_t distributions from the high p data, illustrating the strong dependence on γ of the constraint obtained on α (see Section 7.3.2 for the description of the model).

Table 7-5: χ^2 values from continuum model fits to high p_t μ^+ data

$$\text{Model:}\quad E\frac{d^3\sigma}{dp^3} \propto \frac{1}{m^3}\, e^{-\gamma m/\sqrt{s}}\, (1 - |x_F|)^{\beta}\, e^{-\alpha p_t}$$

χ^2 for the $p_{t\mu^+}$ distribution: (6 d.o.f. : acceptable fit = 12.8)

	$\gamma/\sqrt{s}$ \ α	.400	1.00	2.00	3.50	4.50	10.0
$\beta = 3.00$	.117		171.8	118.0	93.9		
	1.00	324.8	72.0	42.0	29.1		
	2.00	247.7	56.3	25.8	23.7		
	3.54	260.0	53.4	29.4	25.3	27.6	27.2

	β \ α	2.00	3.50	4.50
$\gamma = 2.00$	3.00	25.8	23.7	
	4.00	29.3	25.5	18.2
	5.00	26.0	20.7	20.7

χ^2 for the p_{μ^+} distribution: (5 d.o.f. : acceptable fit = 11.3)

	$\gamma/\sqrt{s}$ \ α	.400	1.00	2.00	3.50	4.50	10.0
$\beta = 3.00$	.117		44.1	31.3	29.0		
	2.00	44.4	20.6	16.5	13.1		
	3.54	40.0	16.6	12.9	10.6	9.6	13.7

	β \ α	2.00	3.50	4.50
$\gamma = 2.00$	3.00	15.6	11.5	12.5
	4.00	12.0	14.3	15.9
	5.00	10.6	12.3	12.1

Table 7-6: χ^2 values from single D model fits

Model: $$E\frac{d^3\sigma}{dp^3} \propto e^{-\alpha p_t}\,(1 - |x_F|)^{\beta}$$

High p μ^- data:

$\beta \backslash \alpha$	$p_{t\mu^-}$				p_{μ^-}			
	1.00	2.00	3.50	4.50	1.00	2.00	3.50	4.50
3.00	34.7	6.7	22.7	29.3	2.3	2.7	4.0	4.1
5.00	46.5	6.0	17.1	25.3	5.4	3.5	3.7	3.9

High p μ^+ data:

$\beta \backslash \alpha$	$p_{t\mu^+}$				p_{μ^+}			
	1.00	2.00	3.50	4.50	1.00	2.00	3.50	4.50
3.00	24.8	2.6	4.0	6.1	15.0	20.8	24.3	25.6
5.00	40.8	3.8	3.2	5.7	9.7	14.5	18.8	19.9

High p_t μ^+ data: (normalized and fit to data with $p_t > 0.9$ GeV/c)

$\beta \backslash \alpha$	$p_{t\mu^+}$				p_{μ^+}			
	1.00	2.00	3.50	4.50	1.00	2.00	3.50	4.50
3.00	55.8	6.1	16.6	14.6	47.1	23.2	12.8	20.6
4.00	52.6	4.5	13.7	16.4	40.4	22.4	13.2	17.3
5.00	58.2	3.9	14.7	12.5	32.9	18.8	12.2	19.5

Table 7-7: χ^2 values from single D model with m_t dependence

$$\text{Model:}\quad E\frac{d^3\sigma}{dp^3} \propto e^{-6m_t}(1-|x_F|)^{\beta}$$

$$m_t = \sqrt{p_t^2 + m_D^2}$$

	χ^2 / d.o.f.	
Data Set	p	p_t
High p μ^+	23.1/6	2.2/4
High p μ^-	4.0/6	13.3/4
High p_t μ^+	12.7/5	21.6/5
		14.6/4 (above $p_t = 0.9$ GeV/c)

Table 7-8: Efficiencies and total cross sections for different models.

α	β	γ	Data Set	ε	$\sigma(\mu b/\text{nucleon})^*$
2	3	-	High p μ^+	.0467	17.1
			High p μ^-	.0452	22.9
			High p_t μ^+	.0258	34.6
2.5	3		2μ w/M.E. [31]	.0022	14.7
			2μ w/M.E. $\langle B^2 \rangle=.004$	.0022	22.1
2	5	-	High p μ^+	.0300	26.6
			High p μ^-	.0284	36.4
			High p_t μ^-	.0274	32.6
2.5	5		2μ w/M.E.[31]	.0014	23.8
			2μ w/M.E.$\langle B^2 \rangle=.004$	.0014	35.7
1	3	1	High p (simultaneous fit)	.0233	41.7
			High p_t μ^+	.0409	21.8
1	3	3.5	High p (simultaneous fit)	.0184	53.7
			High p_t μ^+	.0333	26.8
3.5	3	1	High p (simultaneous fit)	.0162	58.3
			High p_t μ^+	.0182	49.0
3.5	3	3.5	High p (simultaneous fit)	.0139	60.2
1	4	1	High p (simultaneous fit)	.0173	57.8
1	4	3.5	High p (simultaneous fit)	.0146	67.4

*Statistical + systematic data errors in σ are $\approx 25\%$ max.

Table 7-9: Cross sections from other experiments using proton beams.

Group	Target	$\sqrt{s}$	σ(μb /nucleon)	Model
BEBC	Cu	28	11-22	$E\frac{d^3\sigma}{dp^3} \propto e^{-2p_t}(1-x_F)^3$
CDHS	Cu	28	7-14	
CHARM	Cu	28	14.5-29	
Coremans-Bertrand et al.	Ilford emulsion	28*		
Bozzoli et al.	"	28*		
Niu et al.	emulsion	28	30±20	
Sandweiss et al.	Ar	28	~ 40	
Pilcher et al.	Cu	28	< 59	$\frac{d\sigma}{dxdp_t} \propto (1-x)^4 e^{-2.5p_t}$
CCHK	p	52	150-2000	varied models
Baum et al.	p	55	< 140	Bourquin-Gailliard
Chilingarov et al.	p	53,63	21.9 ± 5	
Pilcher et al.	Fe	19	< 26	$\frac{dx}{dxdp_t} \propto (1-x)^4 e^{-2.5p_t}$

Table 7-10: Cross sections from other experiments using pion beams.

Group	Target	$\sqrt{s}$	σ(μb /nucleon)	Model
LEBC	p	17	~ 40	
BGRST(BEBC)	p	12	19 ± 11	

models were normalized with the simultaneous fit to the μ^+ and μ^- distributions, as described above, so that only one cross section for each model is given. If the cross sections were calculated for μ^+ and μ^- separately, they differed by (50 ± 27)% (the ratio of the prompt signals, corrected for the difference in efficiency), with the μ^+ cross section smaller. The cross sections were computed from the formula:

$$\sigma_{\text{charm}} = \frac{\text{prompt } 1\mu \text{ rate} \times 13.6 \text{ mb/nucleon}}{\varepsilon \times B}$$

where ε was the detection efficiency from the model, B was the average branching ratio to muons (0.08), and 13.6 mb was the cross section per nucleon for protons on iron at $\sqrt{s} = 28$ GeV[29].

The cross sections in Table 7-8 have not been corrected for production of charmed particles from the cascade as well as from the primary interaction. The size of this production was calculated for the continuum model with parameters $\alpha = 2$, $\beta = 3$, $\gamma = 2$. Pion production of charm was negligible, the production from secondary leading protons contributed $\approx 10\%$ of the total, and the production from tertiary protons contributed $\approx 1.5\%$. These numbers were almost the same for each of the three data samples - high p μ^+, high p μ^-, and high p_t μ^+. The shape of the muon momentum distributions did not change significantly when a 12% contribution from the secondary distributions was added. The conclusion was that the determination of acceptable model fits was not affected by the secondary cross sections, but that the cross sections in Table 7-8 should be reduced by a factor of 0.88 to obtain the cross section for 400 GeV protons alone. The major uncertainty in the calculation of secondary production was the excitation curve. The form $e^{-10.8m/\sqrt{s}}$ was used, because this form fits the ψ data[30].

Also shown in Table 7-8 are some cross sections calculated from observations in this experiment of double prompt muon production[31], identified by missing energy in the final state indicative of neutrinos accompanying the $\mu^+\mu^-$ pair. The efficiencies have been corrected from those given in Reference 31 based on present knowledge of the different semileptonic branching ratios of the D^o and D^+.

7.4 Comparison with Other Charm Searches

The range of cross sections obtained in the previous section can be compared with the cross section measurements or limits from other searches for the hadronic production of charm. The other experiments may be divided into four classes:

(1) experiments that detect hadronic decay products and search for resonances in the invariant mass distributions[32-37]. References 35 and 37 discuss the detection of the charmed baryon Λ_c and are separately treated in Section 7.6.

(2) experiments that detect short tracks (of order 100 microns) that correspond to the range of charm lifetimes. The detection methods include emulsions exposed to hadron beams[38-40] and a high pressure streamer chamber[41].

(3) experiments that detect prompt neutrinos (often called beam dump experiments). These are discussed in Section 7.5.

(4) experiments that detect prompt charged leptons - either single muon (this experiment, [24]), single electrons[42-43], or μ-e coinci-

dences[43-44].

The results of those experiments which use proton beams are listed in Table 7-9; some results from pion beams are given in Table 7-10. All the cross sections were rescaled to the assumption of 8% semileptonic branching ratio and linear A dependence if necessary. The limits quoted for the emulsion experiments of References 39 and 40 are taken from the curve of lifetime versus cross section given in Reference 45 for $\tau = 3 \times 10^{-13}$ seconds.

7.5 Comparison with the CERN Beam Dump Experiments

The CERN beam dump experiments searched for a prompt neutrino signal produced by dumping a 400 GeV proton beam into a copper target which absorbed most of the long-lived hadrons before they could decay. The three detectors were the large bubble chambers Gargamelle and BEBC and the magnetized iron detector from the WA-1 neutrino experiment. All observed a finite signal for prompt neutrino production [46-48]; the cross sections reported in the first run varied from 10-100 μb/nucleon (assuming linear A dependence). More recent numbers from the BEBC, WA-1, and CHARM groups (CHARM is another counter neutrino detector) [49] are listed in Table 7-9 and vary from 10-20 μb/nucleon for a single D model with $\alpha = 2$, $\beta = 3$.

The acceptance for each of the beam dump detectors was the forward 10 μster - a half angle of 1.8 mrad. The resolution in $p_{t\mu}$ of this experiment (~ 300 MeV) made it unfeasible to cut the high p data to reproduce this very forward acceptance, and the high p_t data were of course in a very different kinematic region. A comparison using models for D production can be made, however. Figure 7-4 shows the plot of $(\nu_e + \bar{\nu}_e)$/proton/μster versus E_ν as measured by BEBC. Also plotted is the quantity $(\mu^+ + \mu^-)$/proton/μster, obtained by normalizing a D production model to the high p data of this experiment, then using the model to calculate the number of μ's in the forward 10 μster.

7.6 Comparison with the ISR Λ_c Measurements

Spectrometer experiments at the CERN ISR[35-37] have observed a resonance in hadronic channels that has been interpreted as the $\Lambda_c(2280)$, the lightest charmed baryon. Using a diffractive model for associated production of Λ_c-D states, these experiments obtain large cross sections, of order 100 microbarns, for such production.

Monte Carlos for a diffractive model have been compared with the data for this experiment, and two conclusions are drawn from the comparison (see Figure 7-5):

(1) The diffractive model does not give an acceptable fit to the data (CL of 4% for the p_{μ^-} distribution and 0.2% for the p_{μ^+} distribution). However, a substantial amount of diffractive production in combination with $D\bar{D}$ production could fit the data.

(2) The $\mu^+\mu^-$ asymmetry in total rate and in x_F dependence induced in the diffractive model are in the direction of the asymmetry observed in the data.

A further point to note is that the efficiencies for the μ^+ and μ^- from the diffractive model were 9% and 12.5% respectively - about a factor of 3 higher than the largest efficiency obtained in the continuum model. Therefore, even if all the observed rate in this experiment

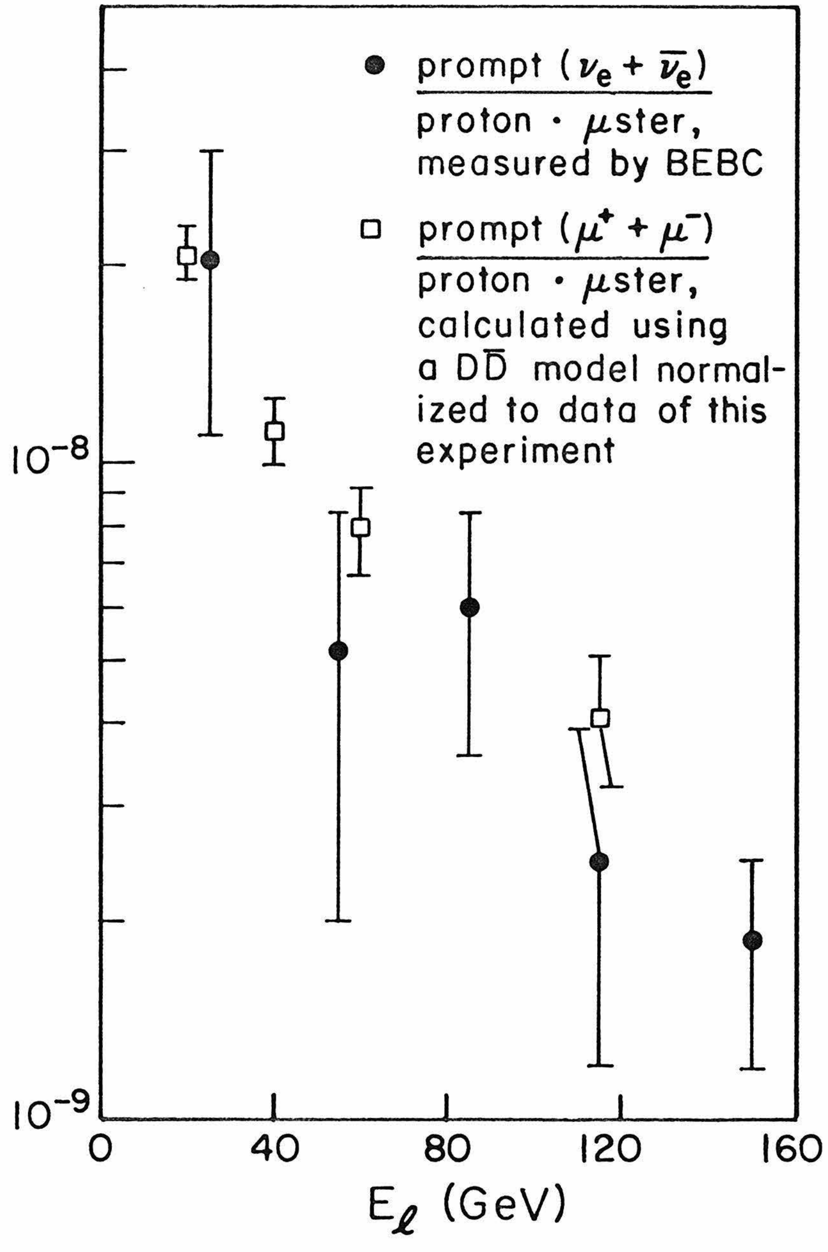

Figure 7-4: The prompt neutrino rate measured by BEBC [49] is compared with the rate in the forward 10 μster calculated using a $D\bar{D}$ continuum model normalized to the high p data of this experiment. The model had parameters $\alpha = 1$, $\beta = 2$, and $\gamma = 3$; and the normalization corresponded to a total cross section of 30 μb/nucleon.

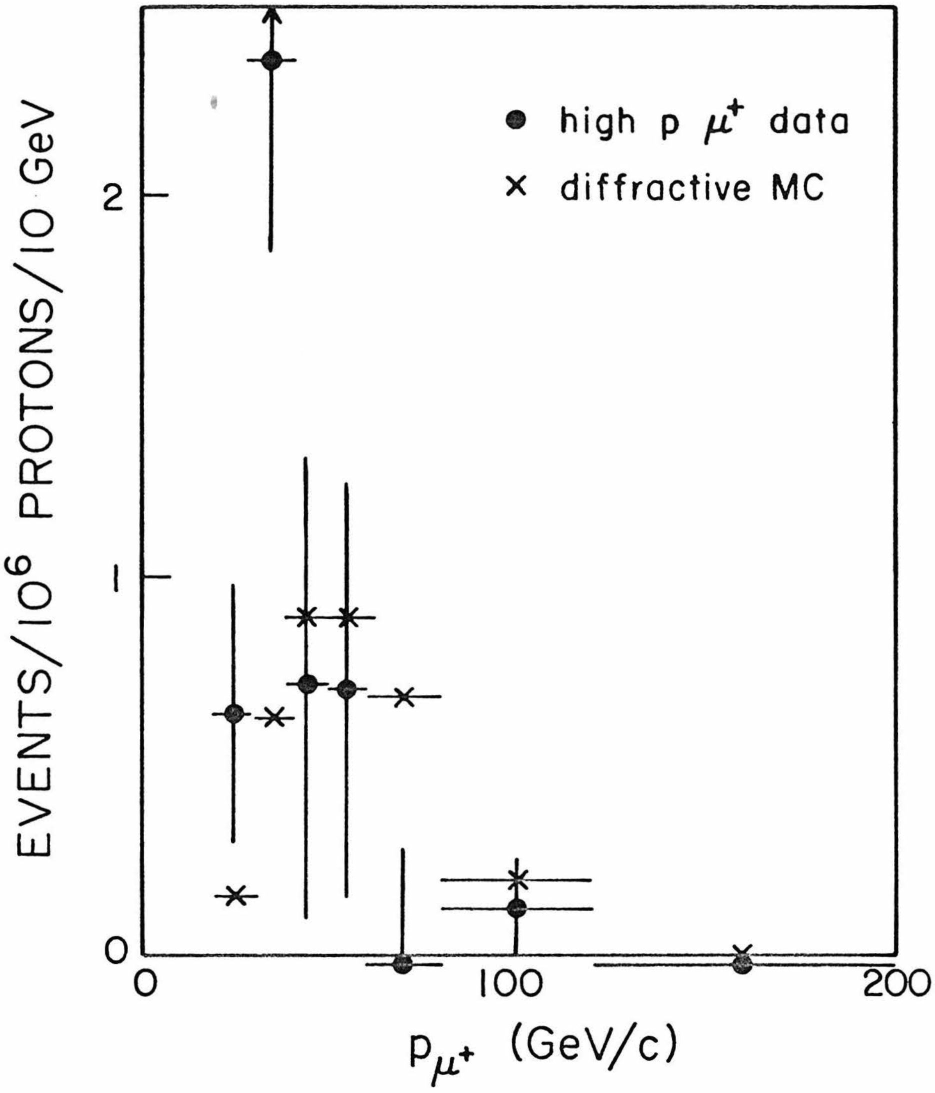

Figure 7-5: a) The p distribution of the high p μ^+ data is compared with the distribution obtained from a Monte Carlo of Λ_c^+ produced diffractively (Section 7.6), normalized to the observed signal. The χ^2 value is 21/6 degrees of freedom.

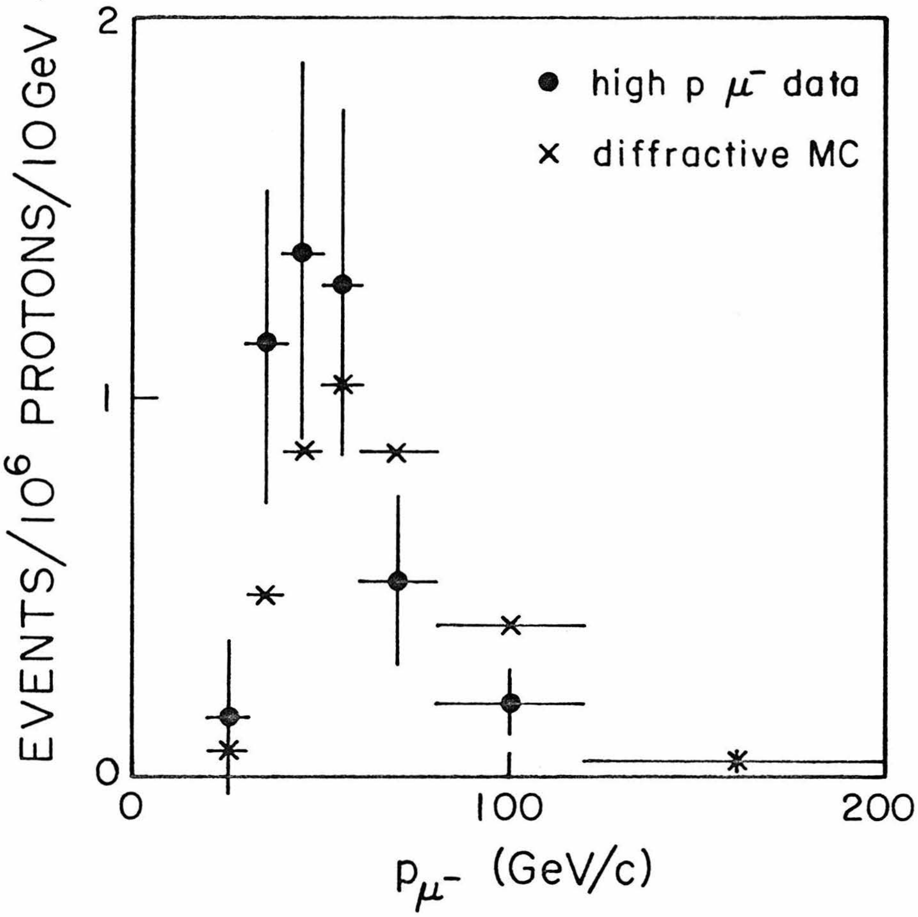

Figure 7-5: b) The p distribution of the high p μ^- data is compared with the distribution obtained from a Monte Carlo of D's produced diffractively (Section 7.6), normalized to the observed signal. The χ^2 value is 13/6 degrees of freedom.

resulted from diffractive production, the calculated cross section would be 14 μb/nucleon for the μ^+ signal and 8 μb/nucleon for the μ^- signal, assuming a 5% semileptonic branching ratio for Λ_c^+ [50] and an average 8% branching ratio for the accompanying D meson. The excitation curve $e^{-10.8\sqrt{\tau}}$, mentioned above, gives a factor of 2.4 increase from $\sqrt{s} = 28$ GeV to 63 GeV, implying a 95% CL limit from these data of ~ 55 μb at the ISR energies. The cross sections calculated from the three ISR observations of a Λ_c^+ peak are 35 μb, 135 μb, and 515 μb[51].

7.7 Theoretical Predictions of Charm Production

A firm prediction of charm production using the framework of QCD has proved elusive. Calculations have been performed for the processes of quark fusion and gluon fusion (Figure 1-2) by many theorists[8]. These calculations generally agree that the resulting total cross sections are less than 5 μb at $\sqrt{s} = 28$ GeV. Larger cross sections have been obtained either by using a lower charmed quark mass than the standard choice of 1.8 GeV/c^2[52] (a mass of 1 GeV/c^2 is required to produce $\sigma \sim$ 40 μb at $\sqrt{s} = 28$ GeV) or by including contributions from other diagrams [53]. Enough data now exist to claim a preponderance of evidence that σ at $\sqrt{s} = 28$ GeV is greater than 10 μb and could be considerably larger. Data should soon exist which provide a more model-independent determination of the cross section[54]. These data offer an inviting opportunity to test QCD if a realistic calculation can be made.

7.8 Other Possible Sources of Prompt Single Muons

Sources of prompt single muons other than charm decay are expected to be small. The production cross section for $\tau^+\tau^-$ pairs is expected theoretically to be equal to the cross section for $\mu^+\mu^-$ pairs of invariant mass greater than $2m_\tau$; this cross section has been calculated[55] to be of order 10^{-4} μb/nucleon, using a formula which fits the $\mu^+\mu^-$ data up to masses of 15 GeV/c^2. The cross section for bare bottom states is predicted in QCD calculations[56] to be around 10^{-2} μb/nucleon at $\sqrt{s} = 28$ GeV. An examination of multimuon final states in this experiment[57] established limits of 4×10^{-2} μb/nucleon for bottom states.

Utilizing the observations in this experiment of double prompt muons from weak decays[31] as well as the observation of single prompt muons, an estimate of the average branching ratio can be made:

$$\left(\frac{1\mu}{2\mu}\right)_{\text{obs}} = \frac{1}{\varepsilon \cdot B} \cdot \left(\frac{\text{prompt weak } 2\mu}{\text{all } 2\mu}\right)_{\text{obs}}$$

$$B = \frac{(\text{prompt weak } 2\mu/\text{all } 2\mu)_{\text{obs}}}{(1\mu/2\mu) \cdot \varepsilon}$$

$$= \frac{.03 - .06}{.642}$$

$$\therefore B = (6 - 10)\%,\ \text{varying the model-dependent acceptance for weak } 2\mu\text{'s.}$$

This calculation may not work as an estimate of the charm branching ratio to muons, because it assumes that the average branching ratio for double prompt muonic decay is the square of the average branching ratio, which is true if the production ratios given above are correct. However, it does exclude non-charmed hyperons with large cross sections and small muonic branching ratios as the sole source of the signal.

7.9 Conclusions

Prompt single muon production has been observed in the kinematic regions $p_\mu > 20$ GeV/c, $p_{t\mu} < 1$ GeV/c and $p_{t\mu} > 0.5$ GeV/c, 10 GeV/c $< p_\mu <$ 60 GeV/c. The assumption that weak decays of charmed particles were the source of the muons is found to be compatible with the data. Other possible sources were measured or calculated to be much smaller than the observed rates.

The rate of single muon production was converted to a total charm cross section within the framework of two simple models for charm production - uncorrelated D production and correlated $D\overline{D}$ production. The kinematic distributions of the data were used to constrain the parameters of the models:

$$\begin{array}{cl} 1 < \alpha < 3 & \text{single D model} \\ \text{insensitive to } \beta & \end{array}$$

$$\begin{array}{cl} \alpha > 0.4 & \\ 2.5 < \beta < 5.0 & \text{continuum D model} \\ \gamma > 0.5\sqrt{s} & \end{array}$$

The range of cross sections obtained for the acceptable parameters was 10-60 μb/nucleon for the p_t data and 20-90 μb/nucleon for the high p data, assuming linear A dependence and an average muonic branching ratio of 8%.

The relative rates of prompt $1\mu^+$ and prompt $1\mu^-$ production were investigated using the high p data. The total rates were equal to within one standard deviation. An asymmetry was observed in the p_μ distribution with the μ^+ distribution favoring a steeper x_F dependence, but the statistical level of this difference was 1.5 standard deviations, and both the μ^+ and μ^- distributions could be fit for $\beta = 3$-4 in the continuum model.

The diffractive model for Λ_c-D production could not totally explain these data, but a substantial amount of diffractive production could be allowed by the data. A most conservative limit of $\sigma < 55$ μb was set for diffractive production at ISR energies, assuming linear A dependence (the limit increases by a factor of 3 if $A^{.67}$ dependence is assumed).

APPENDIX

NONLINEAR EFFECTS IN THE DENSITY EXTRAPOLATION

The density extrapolation technique is based on the following formula for the decay rate of a particle of interaction length λ_i and decay length $\lambda_d = \gamma c\tau$, in a material of density ρ:

$$R = \sigma \cdot B \cdot \frac{\lambda_i}{\lambda_d} \cdot \frac{1}{\rho} \cdot \frac{1}{1 + \frac{\lambda_i}{\lambda_d} \cdot \frac{1}{\rho}}$$

where σ is the production cross section and B the branching ratio into muons. The rate is exactly linear in $1/\rho$ in the limit $(\lambda_i/\lambda_d) \to 0$. The values of (λ_i/λ_d) for π's, K's, Λ's, and Σ's are listed in Table A-1 for typical values of γ. Clearly, the nonlinear effects in the π and K rates are very small. The hyperon rates have nonlinearities of several per cent, but the combination of small σ, small B, and small mean E_μ meant that the trigger rate from hyperons was negligible in this experiment.

The formula above applies to a material of uniform density, but the apparatus used in this experiment was a set of steel plates followed by air gaps of varying length. Small nonlinearities would be expected from the nonuniformity.

The Monte Carlo for π and K production included the effects of nonuniform density and $(\lambda_i/\lambda_d) \neq 0$, and also used the proper energy distribution for π's and K's, the proper π/K ratio, and the proper exponential distribution in interaction point. The Monte Carlo gave a value for the nonlinearity between compacted and expanded density, excluding trigger acceptance, of $(8.0 \pm 8.3) \cdot 10^{-3}$, implying a change of less than 2% in the prompt signal.

Table A-1: λ_i/λ_d values

Particle	E	γ	λ_d	λ_i/λ_d
π	15 GeV	107.4	$8.4 \cdot 10^4$	$2.5 \cdot 10^{-4}$
K	15 GeV	30.4	$1.1 \cdot 10^4$	$2.2 \cdot 10^{-3}$
Λ^o	75 GeV	67.3	$5.3 \cdot 10^2$	$4.7 \cdot 10^{-2}$
Σ^+	75 GeV	63.1	$1.5 \cdot 10^2$	$1.7 \cdot 10^{-2}$
Σ^-	75 GeV	62.7	$2.8 \cdot 10^2$	$9.0 \cdot 10^{-2}$

REFERENCES

1. S. D. Drell and T. M. Yan, Phys. Rev. Lett. 25, 316 (1970).
2. J. J. Aubert et al., Phys. Rev. Lett. 33, 1404 (1974).
3. W. R. Innes et al., Phys. Rev. Lett. 39, 1240 (1977).
4. M. J. Shochet, Proc. of Summer Institute on Particle Physics, SLAC-204, p. 321 (1977).
5. K. J. Anderson et al., Phys. Rev. Lett. 43, 1219 (1979).
6. H. D. Politzer, Phys. Reports 14, 129 (1974).
7. J. Ellis, M. K. Gailliard, and D. V. Nanopoulos, Nucl. Phys. B100, 313 (1975).
8. J. Ellis and M. Einhorn, Phys. Rev. D12, 2007 (1975); A. Donnachie and P. V. Landshoff, Nucl. Phys. B112, 233 (1976); L. M. Jones and H. W. Wyld, Phys. Rev. D17, 1782 (1978); J. Babcock, D. Sivers, and S. Wolfram, Phys. Rev. D19, 234 (1979).
9. S. L. Glashow, J. Iliopoulos, and L. Maiani, Phys. Rev. D2, 1285 (1970).
10. J. E. Augustin et al., Phys. Rev. Lett. 33, 1406 (1974); G. Goldhaber et al., Phys. Rev. Lett. 37, 255 (1976); I. Peruzzi et al., Phys. Rev. Lett. 37, 569 (1976).
11. J. Lach and S. Pruss, Fermilab Memo TM-285 (1971).
12. F. J. Sciulli, Photon-Collecting Hadron Calorimeters, in Proc. of the Calorimeter Workshop, Fermilab, ed. by M. Atac (May 1975), and references therein.
13. R. Coombes et al., Nucl. Instr. and Meth. 98, 317 (1972).
14. F. Merritt, Ph.D. Thesis, California Institute of Technology (1977).

15. The Multi program is now supported by the Fermilab Computer Department.

16. J. P. Dishaw, Ph.D. thesis, SLAC Report 216 (1979).

17. M. Bourquin and J. M. Gailliard, PL 59B, 191 (1975).

18. J. P. Dishaw et al., Phys. Lett. 85B, 142 (1979).

19. Kichimi et al., Phys. Lett. 72B, 411 (1978).

20. F. E. Taylor et al., Phys. Rev. D14, 1217 (1976).

21. K. J. Anderson et al., Phys. Rev. Lett. 36, 237 (1976); K. J. Anderson et al., Phys. Rev. Lett. 37, 799 (1976).

22. Y.-S. Tsai, Rev. Mod. Phys. 46, 815 (1974); erratum Rev. Mod. Phys. 49 (1977).

23. M. J. Lauterbach et al., Phys. Rev. Lett. 37, 1437 (1976).

24. J. G. Branson et al., Phys. Rev. Lett. 38, 457 (1977).

25. J. Rosner, Proc. of the Cosmic Ray and Particle Physics Conference, Newark, Delaware, ed. by T. K. Gaisser, p. 297 (1978).

26. J. Kirkby, Proc. of the Lepton-Photon Symposium, Fermilab, ed. by T. B. W. Kirk and H. D. I. Abarbanel, p. 107 (1979).

27. J. D. Prentice, ibid., p. 563.

28. B. Guberina et al., Phys. Lett. 89B, 111 (1979).

29. A. S. Carroll et al., Phys. Lett. 80B, 319 (1979).

30. W. R. Innes, Proceedings of Summer Institute on Particle Physics, Stanford, California, SLAC-204, p. 425 (1977).

31. A. Diamant-Berger et al., Phys. Rev. Lett. 43, 1774 (1979).

32. D. Drijard et al., Phys. Lett. 81B, 248 (1979).

33. D. Spelbring et al., Phys. Rev. Lett. 40, 605 (1978).

34. W. R. Ditzler et al., Phys. Lett. 71B, 451 (1977).

35. K. L. Giboni et al., Phys. Lett. 85B, 437 (1979).

36. W. Lockman et al., Phys. Lett. 85B, 443 (1979).

37. D. Drijard et al., Phys. Lett. 85B, 443 (1979).

38. H. Fuchi et al., Phys. Lett. 85B, 135 (1979).

39. G. Coremans-Bertrand et al., Phys. Lett. 65B, 480 (1976).

40. W. Bozzoli et al., Lett. Nuovo Cimento 19, 32 (1977).

41. D. Reeder, Proc. of Lepton-Photon Symposium, Fermilab, ed. by T. B. W. Kirk and H. D. I. Abarbanel, p. 553 (1979).

42. R. Barloutaud et al., Rutherford preprint RL 80/003, submitted to Nucl. Phys. B (1980).

43. Chilingarov et al., Phys. Lett. 83B, 136 (1979).

44. Baum et al., Phys. Lett. 77B, 337 (1978).

45. D. J. Crennell, C. M. Fisher, and R. L. Sekulin, Phys. Lett. 78B, 71 (1978).

46. P. Alibran et al., Phys. Lett. 74B, 134 (1978).

47. P. C. Bosetti et al., Phys. Lett. 74B, 143 (1978)

48. T. Hansl et al., Phys. Lett. 74B, 139 (1978).

49. H. Wachsmuth, Proc. of the Lepton-Photon Symposium, Fermilab, ed. by T. B. W. Kirk and H. D. I. Abarbanel, p. 541 (1979).

50. J. G. Körner and G. Kramer, Zeitschrift für Physik C, Particles and Fields 2, 117 (1979).

51. A. Kernan, Proc. of the Lepton-Photon Symposium, Fermilab, ed. by T. B. W. Kirk and H. D. I. Abarbanel, p. 535 (1979).

52. C. E. Carlson and R. Suaya, Phys. Lett. 81B, 329 (1979).

53. B. L. Combridge, Nucl. Phys. B151, 429 (1979).

54. A. Bodek, University of Rochester preprint, UR-730 (1979).

55. The calculation used a fit to $\frac{d^2\sigma}{dmdy}$ from D. Kaplan et al., Fermilab Pub-77/107 (1977).

56. F. Halzen, Proc. of the Cosmic Ray and Particle Physics Conference, Newark, Delaware, ed. by T. K. Gaisser, p. 261 (1978).

57. A. Diamant-Berger et al., Phys. Rev. Lett. 44, 507 (1980).

58. CERN Courier, Vol. 20, No. 4 (June, 1980) p. 159.